FLUIDELASTIC INSTABILITY OF HEAT EXCHANGER TUBE ARRAYS

by

METIN YETISIR, B.Sc., M.Eng.

A Thesis

Submitted to the School of Graduate Studies

in Partial Fulfillment of the Requirements

for the Degree

Doctor of Philosophy

McMaster University

FLUIDELASTIC INSTABILITY IN HEAT EXCHANGERS

DOCTOR OF PHILOSOPHY (1991) | McMASTER UNIVERSITY

(Mechanical Engineering) | Hamilton, Ontario

TITLE : Theoretical Model Development For Fluidelastic Instability of Heat Exchanger Tube Arrays

AUTHOR : METIN YETISIR,
B.Sc. (Middle East Technical University, Ankara)
M.Eng.(McMaster University, Hamilton)

SUPERVISOR : Dr. D.S. Weaver

NUMBER OF PAGES : xiii, 173

ABSTRACT

A study is carried out to investigate the cross-flow induced instabilities in heat exchanger tube arrays. For this purpose, the shortcomings of the Lever and Weaver unsteady theoretical model for a single flexible tube are dealt with and the modified model is extended to a multiple flexible tube analysis. Among the significant modifications is the introduction of a decay function to take into account the decay of the perturbations. This model predicts both static and dynamic instabilities in the transverse and longitudinal directions. It was found that a single flexible tube become tends towards divergence at high values of the mass-damping ratio. This phenomenon is associated with smaller vibration frequencies than the natural frequency of the heat exchanger tube and approaches zero (divergence) at very high mass-damping ratios. The single flexible tube model is extended to a multiple flexible tube model to investigate the effect of the motion of neighboring tubes. It was found that this effect is very important at high values of the mass-damping ratio where the instability is dominated by stiffness terms. The decay function is investigated experimentally. Velocity fluctuations are measured up to 4 tube rows upstream the vibrating tube. The experimentally determined decay function is used to predict the critical velocities for the dynamic instability. Equations of the theoretical model are solved numerically and the agreement between the experimental data and the theoretical predictions is reasonable for all array configurations.

Dedicated to my wife, Liz

ACKNOWLEDGEMENTS

The author would like to express his sincere gratitude to Dr. D.S. Weaver. His competent assistance was invaluable during the course of this study.

The author is also grateful to Dr. M. A. Dokainish for the use of his computer facilities. Thanks are also due to Dr. Kemal Berkkan, Mr. Bruce Tole, Mr. Mark Werner and Mr. Roy Underhill for the nice working atmosphere.

The financial support provided by the Natural Sciences and Engineering Research Council is also acknowledged.

TABLE OF CONTENTS

LIST OF FIGURES

LIST OF TABLES

NOMENCLATURE

A_o	Minimum gap area
$A(s,t)$	Streamtube area
$a(s,t)$	Streamtube area fluctuation
$C_{(\ldots)}$	Fluid force coefficients
c	Damping
d	Tube diameter
F	Force
{F}	Fluid force array
f(s)	Decay function
f_c	Contact force
f_n	Tube natural frequency [Hz]
$H_{a-h}(f)$	Transfer function
h	Pressure loss coefficient
i	$\sqrt{-1}$
k	Stiffness
K_u	U_f/U_r, A geometry dependent constant
l_o	Total streamtube length
m	Mass of the tube per unit length
n(s)	Unit normal vector at position s
P	Array Pitch
P_r	P/d, Pitch Ratio
P(s,t)	Pressure
p_h	Pressure loss
Re	Reynolds number
ROW	# of tube rows
U(s,t)	Flow velocity
U_p	Pitch velocity
U_r	$U_o/(l_o \omega_n)$, Reduced velocity
U_f	$U_p/(f_n d)$, Dimensionless velocity
U_u	Upstream velocity
s	Curvilinear Coordinate

s_a	Attachment point
s_m	Position of the minimum gap
s_s	Separation point
s_i	Position of the streamtube inlet
t	Time
α	Pitch angle
β	Angular coordinate
β_1	Attachment angle
β_2	Separation angle
δ	Logarithmic decrement of damping
$\phi(s)$	Phase function
ψ_i	Phase angle if i'th tube
λ	Total fluid force coefficient
ρ	Density of the surrounding fluid
ω	Vibration Frequency [rad]
ω_n	Natural Frequency [rad]
$(\ )_e$	Exit
$(\ )_i$	Inlet
$(\ )_x$	X-component
$(\ )_y$	Y-component
$(\ )_L$	Longitudinal component
$(\ )_T$	Transverse component
$(\ )_R$	Real component of a complex number
$(\ )_I$	Imaginary component of a complex number
$(\ )_0$	Mean value
$\{\ \}^e$	Elemental array
$\{\ \}^g$	Global array
$[\ ]^g$	Global matrix
$(\ )^*$	Dimensionless variables

CHAPTER 1
INTRODUCTION

Cross-flow induced vibrations have been a major concern in shell and tube type heat exchangers, such as steam generators, coolers and condensers. In shell and tube type heat exchangers, one fluid flows inside the tubes while another fluid is forced through the shell and over the outside of the tubes. The trend in modern heat exchanger design is to increase flow rates and to use a larger number of smaller diameter tubes with minimum structural constraints for higher efficiency. This approach increases the heat transfer rate while decreasing the pressure drop. These requirements increase the likelihood of problems due to flow induced vibrations.

In heat exchangers, flow types can be broadly classified as (i) cross-flow, (ii) internal axial flow, (iii) external axial flow or (iv) annular or leakage flow. Among these flow types, cross-flow has been found to be most likely to produce exessive vibrations. It is now widely accepted [1,2] that vortex shedding, turbulent buffeting, acoustic resonance and fluidelastic instability are the main mechanisms causing cross-flow induced vibrations in heat exchangers. Vortex shedding and turbulent buffeting result in small amplitude vibrations which in turn might lead to unpredictable long term fretting failures at the supports. On the other hand, fluidelastic instability causes large amplitude vibrations that might result in heat exchanger failures shortly after they are put into operation. Due to it's destructive nature fluidelastic instability has been a subject of a substantial research effort in the last two decades.

Fluidelastic instability in heat exchangers arises due to the interaction of the vibrating heat exchanger tubes and the flow field around them. The term "fluidelastic" refers to the mutual interaction of the fluid forces and the elastic structural forces. At and above a critical flow velocity, a feedback mechanism develops between the vibrating tubes and the surrounding fluid such that energy from the fluid is fed to the tubes continuously. As a result, the amplitude of vibration grows exponentially to unacceptable levels. Once this happens, tube-to-tube clashing may occur. Failure follows in a very short time if the operation is not halted. Such failures in nuclear steam generators may result in the leakage of primary side fluids into the secondary side fluids. If a leakage is detected, because of the potential danger of radioactive contamination and loss of primary side coolant, nuclear power plant has to be shut down. The cost of repairs and loss of power production may exceed one quarter of a million dollars per day. Therefore an understanding of the fluidelastic mechanism and the prediction of the fluidelastic instability is necessary.

Although there is a substantial amount of experimental data available to avoid fluidelastic instability, scatter in the data is significant. This results in overconservative designs of heat exchangers at the expense of heat exchanger efficiency and higher capital cost. Because of the complexity of the phenomenon, the underlying mechanisms of the fluidelastic instability in heat exchangers are not fully understood. A satisfactory theoretical solution has not yet been obtained. This is because of the difficulty in modelling the flow field. If the fluid forces acting on the vibrating tubes are determined, the fluidelastic instability threshold can be predicted. A proper analytical solution of the flow field would require the solution of 3-D Navier-Stokes equations. Moving boundaries because of the vibrating tube, the unsteady nature of the flow field and turbulence would impose difficulties in obtaining a theoretical solution. No one has succeeded in obtaining an analytical expression for the flow field in a tube bank. A numerical solution in the practical operating velocities cannot be obtained with the existing solution techniques and computer power. In order to obtain the fluid forces acting on a vibrating tube, some researchers [3-17] simply measured them, and some [18-22] have attempted to determine them from potential flow solutions without success. On the other hand, Lever and Weaver [23-25] simplified the flow field based on experimental observations and then determined the fluid forces for the simplified model. They modelled the unsteady fluid forces acting on a single flexible tube and predicted the critical velocity at which the fluidelastic instability starts. Although they reported good agreement between their theory and experiments, there are some shortcomings. S.S. Chen [8], in his generalized theory of fluidelastic instability in tube arrays, discusses these shortcomings.

Among all the theoretical models, potential flow theories

[18-22] are not fully capable of modelling the observed behaviour of the tube arrays. Unsteady semi-empirical theories [6-8, 14-16] measure all the unsteady force coefficients, and therefore should, and do, predict the instability threshold quite well. Since the measurement of a large number of force coefficients is necessary for each array geometry, such models are not practical design tools. Price & Païdoussis' quasi-steady [9-13] approach requires far fewer experimental measurements, but their prediction of the fluidelastic instability threshold is not as good. Lever & Weaver's [23-25] simplified unsteady model requires no new experimental measurements and shows reasonable agreement with experiments for certain array configurations. Thus, Lever & Weaver's theory for the prediction of the fluidelastic instability seems to be a suitable candidate for improvement.

1.1 STATEMENT OF THE PROBLEM

Although Lever & Weaver's model shows good agreement with the experimental data for some array configurations, the results are not satisfactory for others. There are other problems as well. Theoretically, a dynamic model must produce static instability when the time dependent terms are set to zero. Lever & Weaver's model does not predict the static instability from the dynamic model. Also, they predicted multiple instability regions that are not observed in the experiments. These shortcomings were pointed out by Chen [8], and are discussed in detail in Chapter 2.

The purpose of this work is to develop a theoretical model to investigate the fluidelastic instability in heat exchangers. In order to do this, this work deals with the shortcomings of Lever and Weaver's model. By improving and extending Lever and Weaver's theory it is hoped to obtain (a) better understanding of the fluidelastic phenomenon and (b) a more reliable theoretical model applicable to all the tube arrays and which requires a minimum of experimental measurements.

1.2 OUTLINE OF THE THESIS

A literature survey is given in the second chapter. Previous experimental studies are summarized. The historical development of the theoretical studies and the state of knowledge in fluidelastic behavior of heat exchanger tubes is presented.

In chapter three, the theoretical model for a single flexible tube is presented. Modifications done on the basic model of Lever and Weaver are discussed. Among these modifications, introduction of the decay function and the relaxing of the frequency ratio are fundamentally important. The effects of these modifications and the numerical solution are discussed.

The theory for the extension of the single flexible tube model to a multiple flexible tube model is given in chapter 4. In this chapter, determination of the least stable mode of vibration and the resultant stability curves are also presented.

In chapter 5, the experimental study conducted to gain some understanding of the decay and phase characteristics of the velocity perturbations is presented. The design of the test rig and the instrumentation is explained and experimental findings are presented.

The developed model is applied to different array geometries in chapter 6. The results are compared with the experimental data collected from the literature. A subsequent discussion of the results is given.

The conclusions of the present study are presented in chapter 7.

CHAPTER 2

LITERATURE SURVEY

Since the fluidelastic instability mechanism in heat exchangers was recognised by Roberts [26] and widely accepted after Connors [3], a large body of experimental data has been published [30-48]. Roberts [26], studying a row of circular cylinders, observed the switching of jets passing through the gaps between the cylinders. He concluded that it is the jet-switch mechanism that feeds energy to the flexible cylinders continuously and eventually causes dynamic instability. Connors measured the static force coefficients for a row of cylinders and developed a model to predict the fluidelastic instability. Connors' theoretical model [3] yields a simple equation widely known as Connors' Equation. This equation is in the form :

$$\frac{U}{f_n d} = K\cdot\left(\frac{m\delta}{\rho d^2}\right)^{1/2} \tag{2.1}$$

where U is the characteristic flow velocity
f_n is the tube natural frequency
d is the tube diameter
δ is the logarithmic decrement of damping
m is the mass of the tube per unit length
ρ is the density of the surrounding fluid

Here, $U/f_n d$ is called the critical dimensionless velocity and $m\delta/\rho d^2$ is called the mass-damping parameter. Connors reported that the value of K is 9.9 for a single row of tubes. However, later experimental studies [30-38] showed that this constant is array dependent. Many researchers tried to find the value of the constant K in Connors' equation for various array configurations and pitch ratios.. They [30-32] generated tables of K values for design purposes. Hartlen's study [30] also showed that the exponent in Connors' Equation might be different than 0.5. Other experimental works [31, 33, 37, 38] supported this finding. Weaver and Grover [37] showed that grouping the damping, δ, and the mass ratio, $m/\rho d^2$, into mass-damping parameter, $m\delta/\rho d^2$, may not be correct. The effects of damping, δ [37], mass-ratio, $m/\rho d^2$ [38], tube mass, m [40], fluid density, ρ [35], induced upstream turbulence [45], approach flow direction [41] and partial admission [46, 47] on fluidelastic instability have also been investigated. Chen's theoretical studies [6-7] showed that Connors' equation is valid at high values of the mass-damping parameter. However, in general, there is not a simple relationship between the mass-damping parameter, $m\delta/\rho d^2$, and the critical dimensionless velocity, $U/f_n d$. In their review papers, Chen [27], and Weaver et.al.[1], give stability boundaries based on experimental data for various array geometries. Figure 2.1 shows Weaver and Fitzpatrick's [1] definitions of the stability boundaries with experimental data from the literature.

Traditionally, researchers publish their fluidelastic instability data by reporting the mass-damping parameter and the dimensionless velocity. Yet, even after two decades, there is still confusion about which parameters should be used to determine

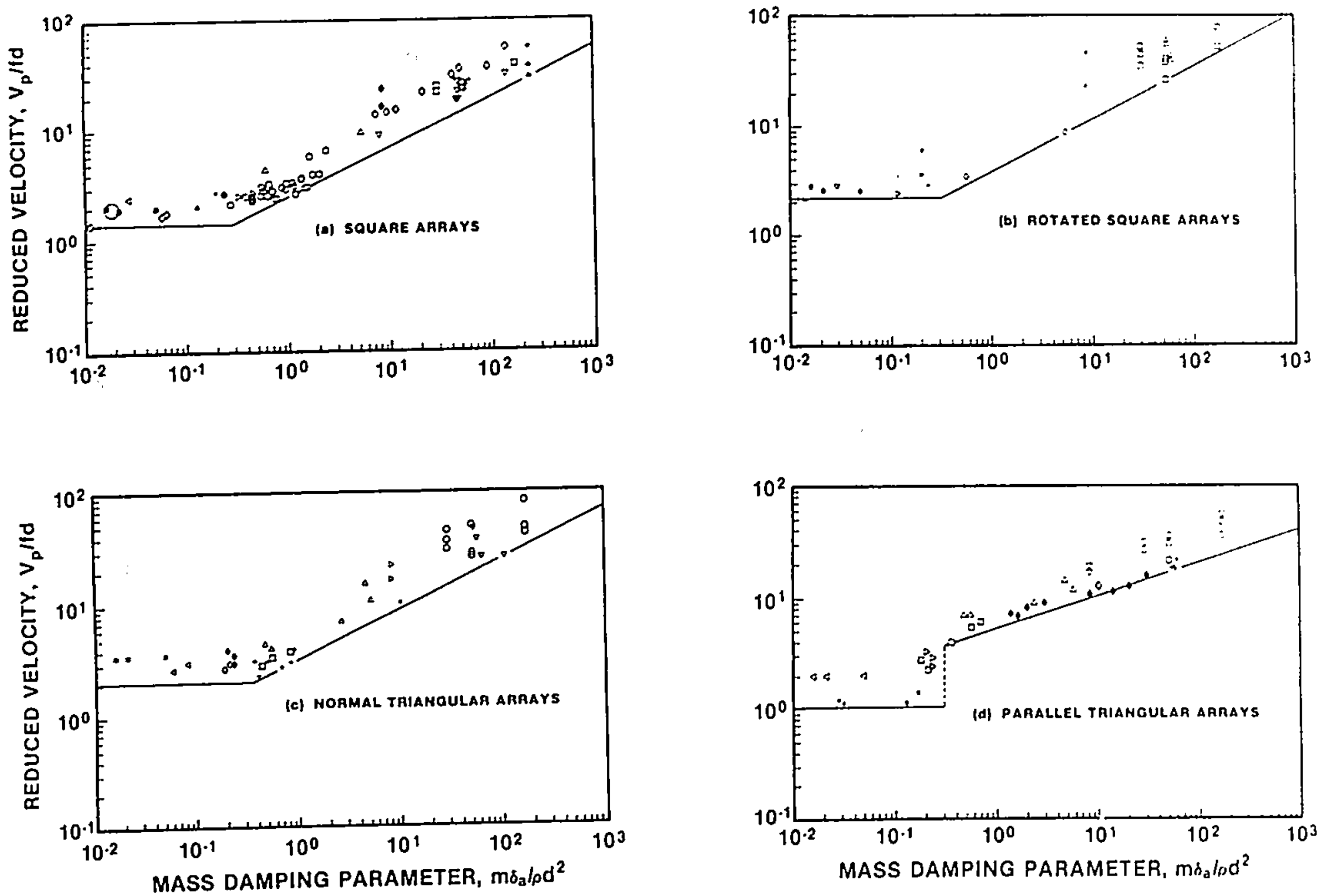

Figure 2.1 Dynamic Instability Thresholds for Various Arrays as Defined by Weaver and Fitzpatrick [1]

the dimensionless velocity, $U_p/f_n d$, and the mass-damping parameter, $m\delta/\rho d^2$. For example, for the tube natural frequency and damping, f_n and δ, some researchers use in-vacuo values, some use quiescent fluid values, and some others use observed values at the stability threshold. The critical pitch flow velocity, U_p, may not be easily determined and different implementation techniques for the same experimental data might yield significantly different values. Chen [28] in his recent review, addresses these problems. Partially as a result of the use of inconsistent parameters and implementation techniques, the experimental data obtained is rather scattered.

On the other hand, attempts have been made to determine the fluidelastic instability theoretically [3-29]. While thesetheories helped the understanding of how fluidelastic instability occurs in heat exchanger arrays, they cannot be used as design tools for the time being. Due to the complexity of the flow field and it's interaction with the tubes, the physics of the phenomenon is not known completely, and this makes the phenomenon difficult to model. Although the structural motion can be modelled successfully, determination of the fluid forces acting on the structure is extremely difficult. These forces can be determined by using (1) experimental techniques [6-17], (2) potential flow theory [18-22], (3) a simplified flow field [23-25]. Experimental studies which measure all the fluid force coefficients [6-8, 14-16] are successful in predicting the fluidelastic instability. However, tedious measurements must be taken for every array geometry under investigation and over a wide range of flow velocities. Thus such techniques are not practical design tools. Models that require fewer measured fluid force coefficients [9-13] do not generally give such good agreement with experiments. Based on physical arguments, Lever and Weaver [23-25] simplified the flow field and obtained an analytical expression with some simplifying assumptions. This simple model produced results with limited success. Models based on the potential flow theory [18-22] are shown not to be suitable in analysing tube array behavior [21].

Early theoretical models employed the quasi-static assumption [3, 26]. These quasi-static theories assume that the forces acting on the heat exchanger tube are a function of tube displacement only. Using experimentally determined force coefficients and an assumed mode shape, they obtained good agreement between experiments and the theoretical prediction at high values of the mass-damping parameter. Connors [3], measured the steady-state force coefficients by positioning the tubes according to a predetermined mode shape. Assuming that the dynamic forces acting on a moving tube can be approximated by the measured static forces, he predicted the critical flow velocity for fluidelastic instability (see Equation 2.1). Blevins' approach is basically an extension of Connors' model. He [4] investigated the vibrations of a row of tubes and by assuming the mode of vibration he determined the critical velocity as a function of displacement dependent force coefficients and damping. Blevins later extended his model [5] to an array of tubes by using the same quasi-static approach.

On the other hand, if the effect of the tube velocity in addition to the tube displacement is taken into account, the fluid forces acting on a vibrating tube can be characterized more realistically. Such models are called quasi-steady models. Price and Païdoussis' theory [9-13], for example, is a quasi-steady theory, since the velocity dependent components of the fluid force are found by using a flow retardation term. They determined the displacement dependent fluid force coefficients experimentally. Then, arguing that there will be a time lag between the fluid force acting on the tube and the tube displacement, they determined the velocity dependent component of the fluid force.

Unsteady theories [6-8, 14-16, 23-25] involve the fluid forces as a function of displacement, velocity and acceleration. Among these theories, Chen's [6-8] and Tanaka et al's [14-16] theories require the experimentally determined fluid force coefficients whereas Lever and Weaver's [23-25] theory doesn't require such experimental measurements. Tanaka and Takahara [14-16] measured the unsteady fluid forces acting on heat exchanger tubes and, assuming linear behavior, superimposed the effect of individual tubes on every tube in the array to obtain the fluidelastic threshold for the fully flexible array. Although they obtained excellent agreement with the experiments, this theory is not a practical design tool, since the force coefficients have to be measured for every different array geometry. Chen, in his generalized theory of fluidelastic instability [6, 8], gave the complete formulation of the phenomenon. However, he also heavily depended on the experimental force coefficients. Although Chen's theory needs the array geometry dependent fluid force coefficients, as in Tanaka and Takahara's theory, it shed light on the mechanisms of fluidelastic instability. The so called stiffness-controlled and damping controlled fluidelastic instabilities are first reported by Chen [6, 7]. Lever and Weaver's theory [23-25], on the other hand, doesn't require such experimental measurements. In a simplified model, starting from first principles, they determined the fluid forces acting on a single flexible tube in an array of rigid tubes. They argued that the stability threshold for the single flexible tube is approximately the same as the fully flexible tube array. They reported good agreement between the theoretical prediction and the experiments for in-line square and parallel triangular arrays, but the agreement was not as good for rotated square and normal triangular arrays.

2.1 STATE OF KNOWLEDGE

While there are number of areas for improvement, theoretical studies explaining fluidelastic instability have increased significantly in the last decade. Now, it is recognised that fluidelastic instability is dominated by velocity dependent fluid forces at low values of the mass-damping parameter. This is called damping controlled fluidelastic instability because instability occurs when the damping of a tube becomes negative. At high values of the mass-damping parameter, displacement dependent fluid forces are dominant. Instability in this range is called stiffness controlled fluidelastic instability.

Quasi-static theories [3, 26] can only predict the stiffness controlled fluidelastic instability, since only the displacement dependent force coefficients are implemented. Similarly, pure potential theories [18-22] can only predict the stiffness controlled instabilities since the perturbations are instantly propagated in potential flow and there is no phase lag between the tube motion and the forces acting on that tube. Therefore, the resultant forces are only displacement dependent. In such theoretical models, the assumed phase relationship between the tubes (mode shape) is the essential requirement for fluidelastic instability.

The main requirement for the modeling of the damping controlled fluidelastic instability is the phase difference between the tube motion and the fluid force acting on it. This is accomplished through a phase function in Lever and Weaver's theory [23-25] and through a flow retardation parameter in Price and Païdoussis' [9-13] theories. Both of these theories predicted multiple unstable regions. Tanaka et al. [14-16] measured the above mentioned phase difference and based their analysis on these values. Chen [6-8] has the same phase lag built in his model through the use of velocity and inertial force coefficients in addition to the displacement force coefficients. Chen [27] reported that a single flexible tube is sufficient to model the damping-controlled fluidelastic instability. He also reported that for stiffness controlled instability, at least two tubes are necessary. In their recent review, Païdoussis and Price [29] conclude that the minimum number of degrees of freedom must be two to model the stiffness controlled mechanism properly. Unlike Chen's finding, they report that a single flexible tube, if modelled in two orthogonal directions (2 degrees of freedom), is sufficient to predict the stiffness-controlled instability. Here, it is important to note that both of these papers reach their conclusions by ignoring the velocity and inertia dependent terms and considering only the displacement dependent terms of the fluid force.

Lever and Weaver's theory [23-25] with it's simple form, showed good agreement with experiments for parallel triangular and in-line square arrays. However, the agreement wasn't as good for normal triangular and rotated square arrays. On the other hand, their theory produced some unexpected results that need to be explained. The problems associated with the Lever and Weaver theory are the following;

(1) Static instability couldn't be obtained from the dynamic model. In a proper theoretical model, when the time dependent terms are equated to zero, the dynamic model should produce the static instability solution. This wasn't the case in Lever and Weaver's model.

(2) A large number of instability regions are predicted by Lever and Weaver at low values of the mass damping parameter. Not more than two instability regions were reported experimentally (see Anjelic [48])

(3) At high values of the mass-damping parameter, the slope of the stability curve is predicted to be unity. This means that the dimensionless velocity, $U_p/f_n d$, is directly proportional to

the mass-damping parameter, $m\delta/\rho d^2$. These results contradict experimental results and other theoretical estimates where the square root of the mass-damping parameter is proportional to the dimensionless velocity.

(4) A single flexible tube surrounded by rigid tubes is assumed to represent the fully flexible array. Some experimental studies [44, 49] with single flexible tubes show that this assumption is not correct for all of the array geometries.

It was the purpose of the present work to develop an improved theoretical model using Lever and Weaver's theory as a basis. To begin with, the above mentioned deficiencies of the Lever and Weaver single flexible tube model was overcome. Then, this model was extended to a multiple flexible tube model to include the effect of the neighboring tube motion.

CHAPTER 3

SINGLE FLEXIBLE TUBE MODEL

In this chapter, Lever and Weaver's model [23-25] is summarized and the natural evolution of the present study from Lever and Weaver's theory is presented. Lever and Weaver modelled a single flexible tube surrounded by rigid tubes. They simplified the flow field and determined the unsteady forces acting on the flexible tube. The effects of varying the array configuration is taken into account so that the theory applies to every array geometry. The shortcomings of Lever and Weaver's theory are discussed in Section 2.2. By introducing a series of modifications to their basic model these shortcomings are dealt with in this study. Among these modifications, the introduction of the decay function and relaxing the frequency ratio in the eigenvalue analysis are fundamentally important. In addition, the numerical solution technique is discussed and the results are presented.

3.1 THEORETICAL MODEL DEVELOPMENT

The basic model used is that of a single flexible tube in an array of rigid tubes. This is the same concept as that developed by Lever and Weaver [23-25] based on some experimental observations, so only the details relevant to the present modifications and consistent with a coherent model development will be repeated here. The theory is general for an array which is symmetric about a streamwise axis through the center of the flexible tube.

Four standard types of array configuration are generally used in existing heat exchangers. These are shown in figure 3.1. From the flow visualization studies of Abd-Rabbo & Weaver [42-43], and Scott [44], flow around the tube is idealized for various array configurations as shown in figure 3.2. These four configurations can be classified in two groups ; (1) in-line square, parallel triangular arrays and rotated square arrays with $P_r < 1.71$: the streamtubes on each side of the heat exchanger tube are separated, and (2) rotated square arrays with $P_r > 1.71$ and rotated triangular arrays : streamtubes on each side of the flexible tube overlap in upstream and downstream of regions of the tube. These differences only affect the selection of the model parameters as will be discussed in the following sections. The basic model concept is the same for all the array configurations. Therefore, for the sake of simplicity, the system parameters will be developed for the parallel triangular array in the following sections and the list of parameters for all the configurations will be given in Chapter 6.

3.1.1 Basic Model Concept

The flow around the tube in a parallel triangular array is characterized by the moving fluid along the streamtubes, as shown in figure 3.3, and represented by the curvilinear coordinate, s. From the flow visualization studies of Weaver et al. [42-44], it is reasonable to assume that the mean area of a streamtube is

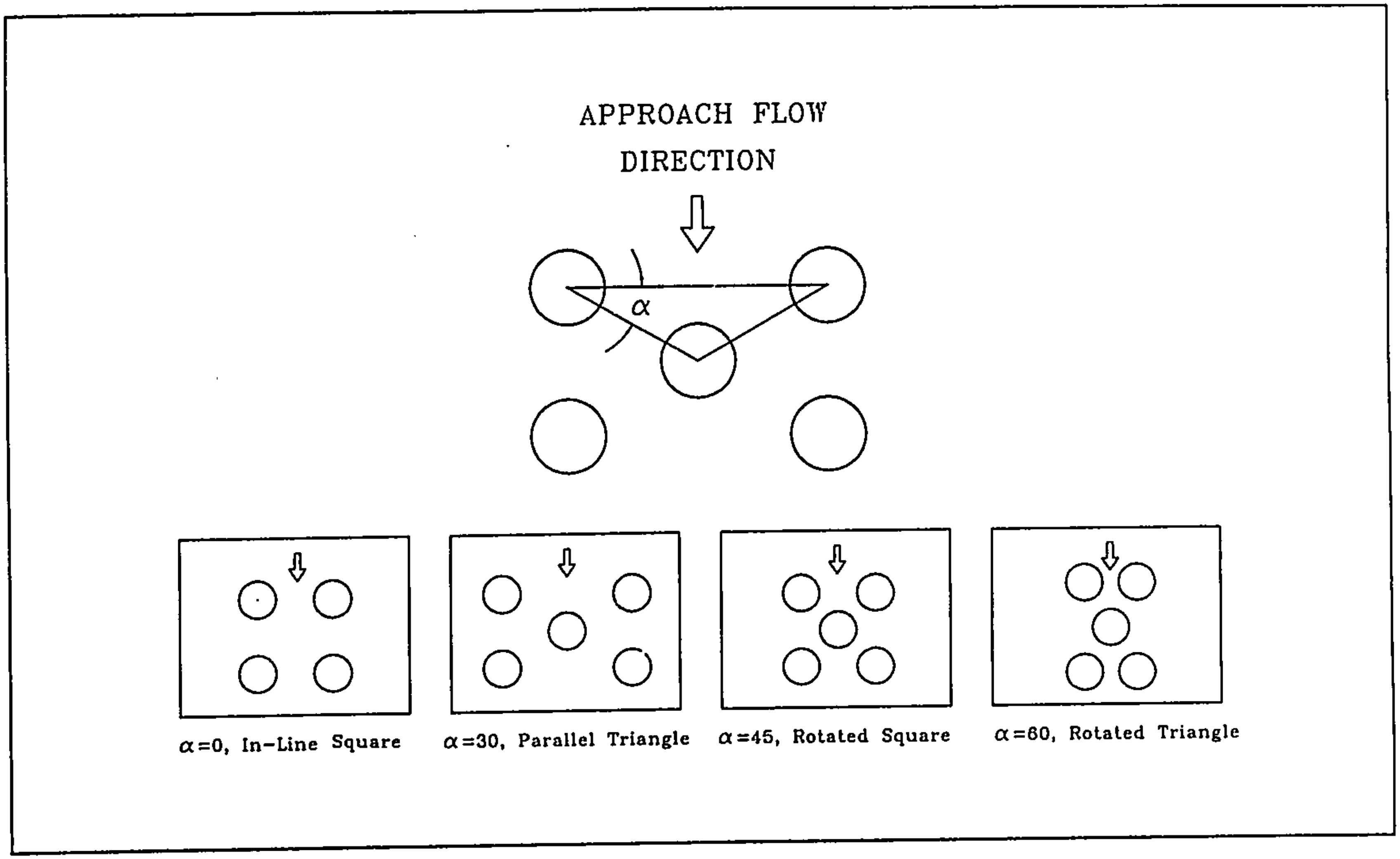

Figure 3.1 Standard Array Configurations

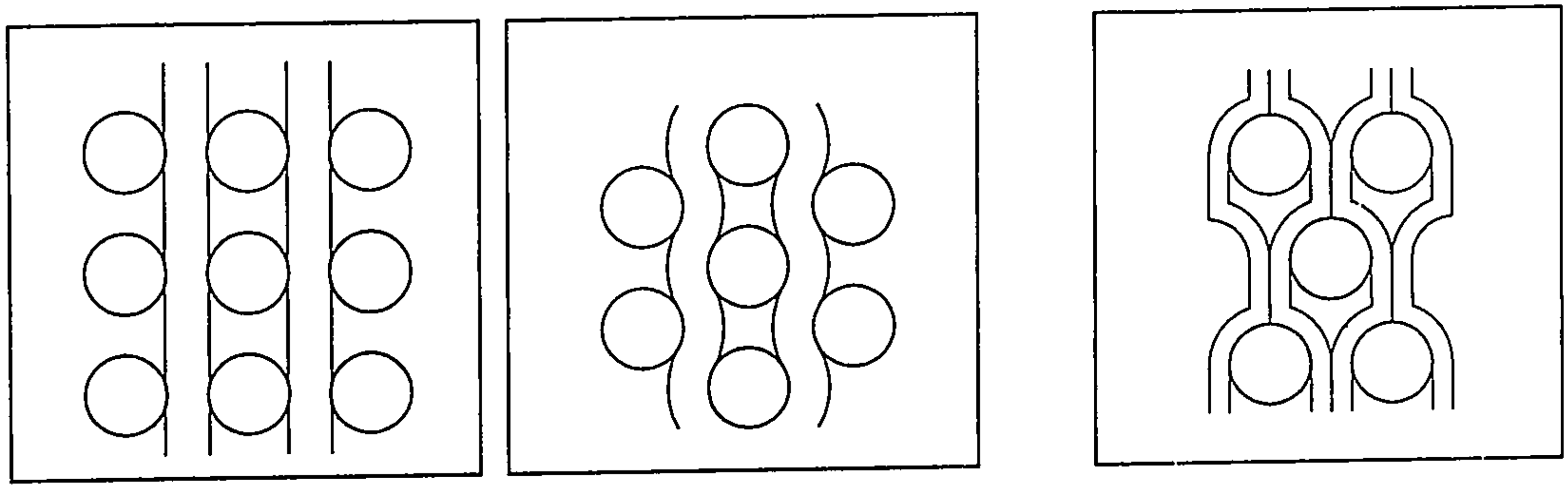

(a) GROUP 1 : In-Line Square, Parallel Triangle and Rotated Square with $P_r \leqslant 1.7$

$$A_o^* = P_r - 1$$

(b) GROUP 2 : Rotated Triangle & Rotated Square with $P_r > 1.7$

$$A_o^* = P_r \cos(\alpha) - 1/2$$

Figure 3.2 Streamtube Geometry for Various tube Arrays

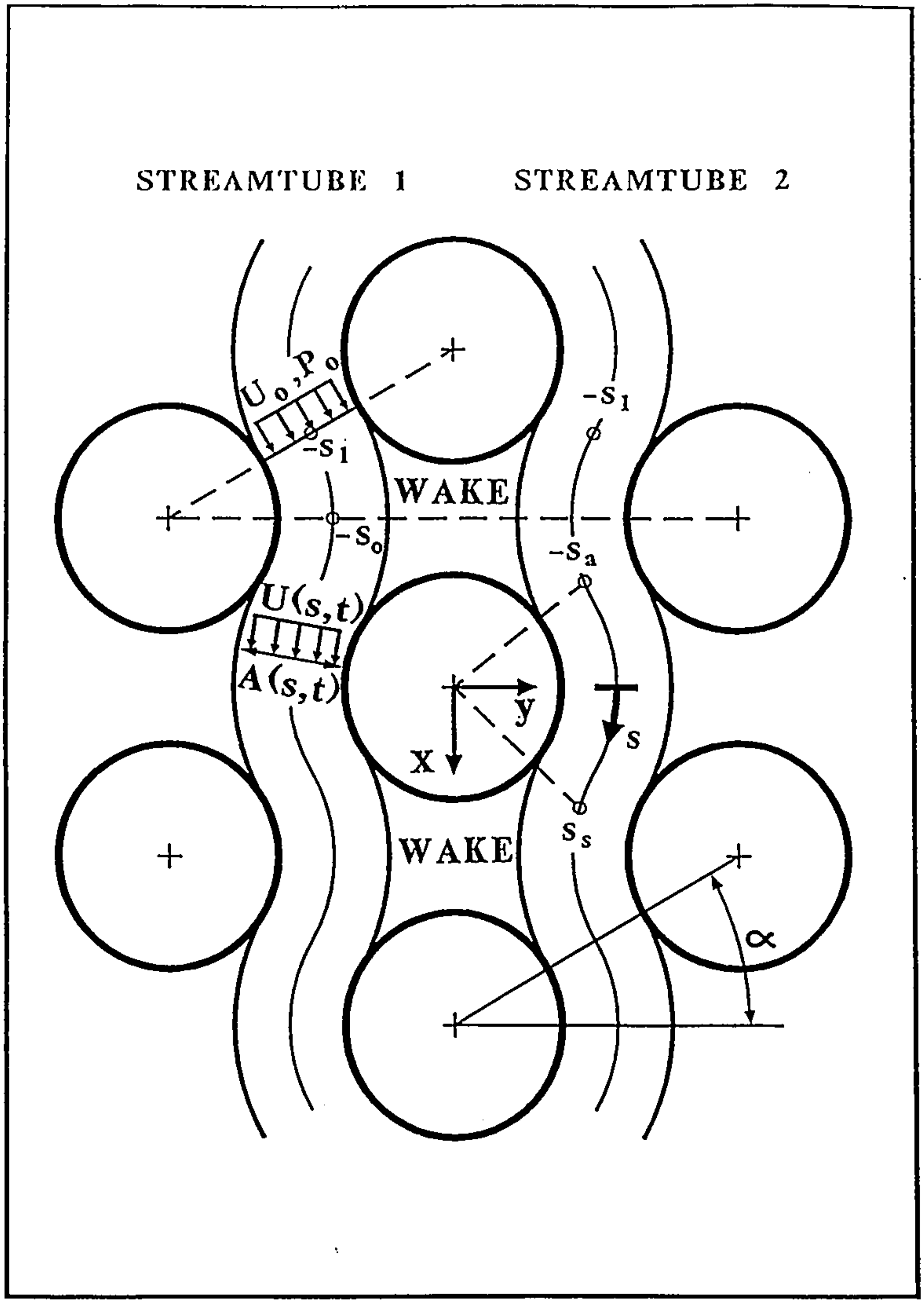

Figure 3.3 Idealized Model for Parallel Triangular Arrays

constant over the streamtube length and is determined by the minimum gap area, A_0, which depends on the tube pitch, P, tube diameter, d, and array geometry angle, α.

$$A_0 = \min(P\cos\alpha - \frac{d}{2}\ ,\ P - d) \tag{3.1}$$

Due to the vibration of the tube, the streamtube area will change along the streamtube with respect to time. Therefore, the streamtube area function can be expressed in terms of the mean component, A_0, and the fluctuating component, a(s,t).

$$A(s,t) = A_0 + a(s,t) \tag{3.2}$$

As a result of the area perturbation, the velocity and pressure along the streamtube will have fluctuating components as well. At some point upstream, the velocity and pressure will be undisturbed and are represented by the initial constant values U_0 and P_0, respectively.

In the curvilinear coordinate system, the location of the minimum gap is at $s = \mp s_m$. As can be seen in figure 3.3, the streamtube attaches to the tube at $s = -s_a$ and separates at $s = s_s$. In the upstream region ($s < -s_a$), there is a point at which the area, velocity, and pressure perturbations reduce to negligible levels. This point is designated $s = -s_1$.

The fluctuation in streamtube area due to the tube motion, will be felt later due to the finite fluid inertia. This time lag is formulated with the use of the phase function, $\phi(s)$.

The area perturbation created by the vibrating tube must diminish at large distances ($s < -s_1$) from the tube. Therefore an area decaying function, $f(s)$, is introduced to account for the decay of the area perturbation. This function will also produce decays of velocity and pressure perturbations. The decay function must satisfy $\lim_{s \to -\infty} f(s) = 0$ (no perturbances at large distances from the vibrating tube). Therefore, the unit area perturbation function for a streamtube in the upstream region is written as:

$$a_u(s) = f(s)e^{i\phi(s)} \quad . \tag{3.3}$$

Note that $a_u(s)$ is defined as the upstream area perturbation for a unit displacement at the minimum gap. Therefore the upstream area perturbation function, $a(s,t)$, for the streamtube can be obtained by multiplying $a_u(s)$ by the total perturbation at the minimum gap, $a(-s_m,t)$. i.e.,

$$a(s,t) = a(-s_m,t)f(s)e^{i\phi(s)} \quad . \tag{3.4}$$

In the attached flow region ($-s_a \le s \le s_s$), the phase lag is zero (i.e. $\phi(s) = 0$) and the decay is assumed to be negligible ($f(s)=1$).

These idealized streamtubes are analyzed using one dimensional unsteady fluid mechanics theory in curvilinear coordinates. Thus, for a given tube disturbance, the fluid pressure on the tube can be determined and the stability of the tube analyzed.

3.1.2. Continuity Equation

For the control volume, C.V., shown in figure 3.4, the continuity equation for an incompressible fluid can be written as,

$$\frac{\partial}{\partial t}\,[A(s,t)] + \frac{\partial}{\partial s}\,[A(s,t)\mathbf{U}(s,t)\cdot\mathbf{n}(s)] = 0 \tag{3.5}$$

where, $\mathbf{U}(s,t)$ is the velocity vector, and $\mathbf{n}(s)$ is the unit vector normal to the surface of the Control Volume. In equation 3.5, the first term corresponds to the accumulating mass in the control volume and the second term gives the amount of fluid crossing the control volume surface.

Let $P_0(s)$ and $U_0(s)$ be the mean components and $p(s,t)$ and $u(s,t)$ be the fluctuating components of the pressure and velocity respectively. i.e.,

$$\left.\begin{aligned} P(s,t) &= P_0(s) + p(s,t) \\ \mathbf{U}(s,t) &= \mathbf{U}_0(s) + \mathbf{u}(s,t) \end{aligned}\right\} \tag{3.6}$$

It is assumed that $P_0(s)$ and $U_0(s)$ do not vary significantly along s, i.e., $P_0(s) = P_0$ and $U_0(s) = U_0$. Substituting equations (3.6) into the continuity equation (3.5) and integrating along the control volume coordinate, s, from inlet $s = s_i$ to exit $s = s_e$, yields, after eliminating steady-state and higher order terms and nondimensionalizing :

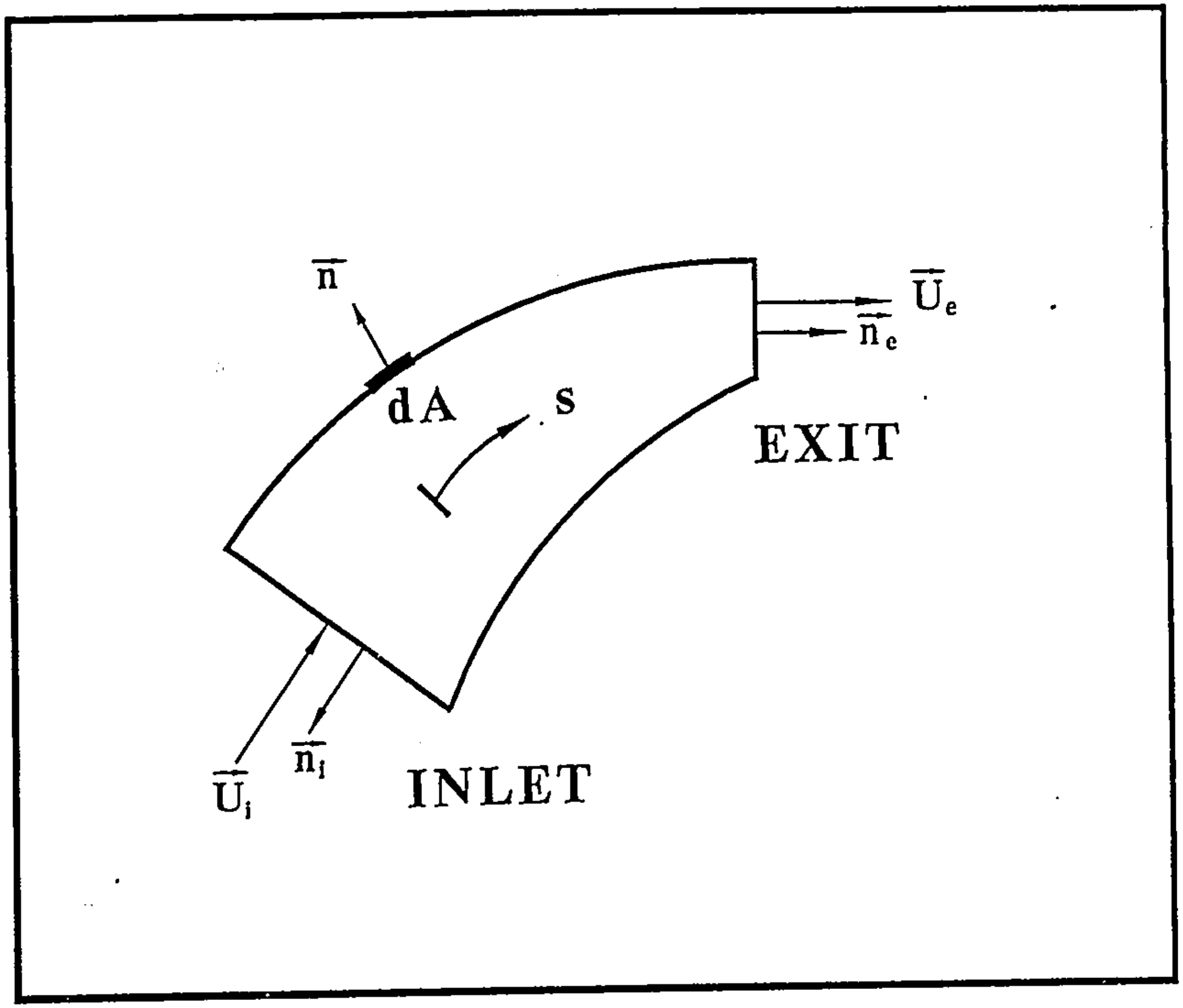

Figure 3.4 The Control Volume

$$\boxed{\frac{1}{U_r}\frac{\omega}{\omega_n}\int_{s_1}^{s_e}\frac{\partial a^{*}(s^{*},t^{*})}{\partial t^{*}}\,ds^{*}+l_0^{*}A_0^{*}[u^{*}(s_e^{*},t^{*})-u^{*}(s_1^{*},t^{*})]+l_0^{*}[a^{*}(s_e^{*},t^{*})-a^{*}(s_1^{*},t^{*})]=0} \tag{3.7}$$

where, $U_r = \dfrac{U_0}{\omega_n l_0}$

ω_n : natural frequency of the tube in still fluid

ω : complex frequency of vibration

$l_0^{*} = l_0/d$, l_0 : dimensionless streamtube length

$t^{*} = \omega t$

$a^{*}(s,t) = a(s,t)/d$

$A_0^{*} = A_0/d$

$u^{*}(s,t) = u(s,t)/U_0$

$s^{*} = s/d$

Note that, $U(s,t)=|U(s,t)|$ and $u(s,t)=|u(s,t)|$

3.1.3 Momentum Equation

The linear momentum equation for the control volume may be written as :

$$\frac{\partial}{\partial t}\int_{V} U(s,t)dV + \oint \rho U(s,t)[U(s,t).n(s)]dA = \frac{1}{\rho}\sum F \tag{3.8}$$

where V : Volume of the control volume and $dV = A\,ds$

In equation 3.8, the first and the second terms correspond to the momentum accumulation and the momentum flux for the fixed control volume, respectively. The R.H.S. of equation (3.8) gives the sum of the external forces acting on the control volume. Shear and gravity forces are assumed to be negligible. Since the pressure is uniform at any cross section, the forces on the sides of the control volume parallel to the streamtube are self-equilibrating. Therefore, the sum of the external forces term reduces to :

$$\begin{aligned}\sum F &= -\oint P(s,t).n(s)dA \\ &= -A(s_1,t)P(s_1,t)n(s_1) - A(s_e,t)P(s_e,t)n(s_e) \qquad (3.9)\end{aligned}$$

The momentum equation may be written in terms of perturbation parameters by substituting equations (3.2) and (3.6) into equation (3.8). After eliminating the steady state and higher order terms and nondimensionalizing, this becomes:

$$\boxed{\begin{aligned}&\frac{\omega}{\omega_n}\int\frac{\partial u^*(s^*,t^*)}{\partial t^*}\,n(s^*)ds^* + \frac{\omega}{\omega_n}\frac{1}{A_0^*}\int\frac{\partial a^*(s^*,t^*)}{\partial t^*}\,n(s^*)ds^* + \\ &[\ 2l_0^*u^*(s_1^*,t^*) + \frac{l_0^*}{A_0^*}\,a^*(s_1^*,t^*)\ ]U_r n(s_1) + \\ &[\ 2l_0^*u^*(s_e^*,t^*) + \frac{l_0^*}{A_0^*}\,a^*(s_e^*,t^*)\ ]U_r n(s_e) + p_h \\ &\qquad\qquad = -p^*(s_1^*,t^*)n(s_1^*) - p^*(s_e^*,t^*)n(s_e^*)\end{aligned}} \qquad (3.10)$$

where $p^* = \dfrac{p_{11}}{\rho d\omega_n U_0} = \dfrac{p}{\rho d l_0 \omega_n^2 U_r}$ and $p_h = h\,\dfrac{l_0^*}{s_o^*}\,U_r\int u^*(s^*,t^*)ds^*$

The pressure drop can be accounted for in equation (3.10) as done by Lever and Weaver [24] by adding p_h on the L.H.S. of Equation (3.10). Here h is the pressure loss coefficient and s_0^* is the inlet location of Lever and Weaver's model.

3.1.4 Pressure Forces Acting on the Vibrating Tube

The pressure forces acting on the vibrating tube can be found by integrating the pressure over the area of flow attachment, $-s_a < s < s_s$. Inspection of the continuity and momentum equations shows that the pressure at any point, and hence the pressure force, is directly proportional to the magnitude of the area perturbation at the minimum gap. For computational convenience, the dimensionless pressure forces, F_L^* and F_T^*, are obtained for a unit perturbation at the minimum gap. Here, subscripts L and T denotes longitudinal and transverse, respectively. These forces are given by,

$$\begin{aligned} F_y^*(t^*) &= F_T^*(t^*) = \int_{-s_a^*}^{s_s^*} p^*(s^*,t^*)\cos\beta(s^*)ds^* \\ F_x^*(t^*) &= F_L^*(t^*) = \int_{-s_a^*}^{s_s^*} p^*(s^*,t^*)\sin\beta(s^*)ds^* \end{aligned} \tag{3.11}$$

where $F^* = \dfrac{F}{\rho d^2 l_0 \omega_n^2 U_r}$

In order to find the total forces acting in the transverse and longitudinal directions, F_L^* and F_T^* must be multiplied by the dimensionless magnitude of the area perturbation at the minimum gap, $a^*(-s_m^*,t^*)$.

3.1.5 Equations of Motion of Tube

The flexible tube is assumed to behave as a two degree of freedom simple harmonic oscillator with the same natural frequency in orthogonal directions. Its equations of motion can be written in the x and y directions as :

$$\left.\begin{aligned} m\ddot{x} + c\dot{x} + kx &= F_x a_1(-s_m,t) + F_x a_2(-s_m,t) \\ m\ddot{y} + c\dot{y} + ky &= F_y a_1(-s_m,t) - F_y a_2(-s_m,t) \end{aligned}\right\} \qquad (3.12)$$

where λ is the tube length, m is the tube mass per unit length including added mass, c is the damping coefficient, k is the stiffness, F_x and F_y are the unit fluid forces acting on the tube in the x and y directions, respectively, and $a_1(-s_m,t)$ and $a_2(-s_m,t)$ are the area perturbations of streamtubes 1 and 2 at the minimum gap, respectively. By definition of the x and y coordinate axes, $F_x = F_L$ and $F_y = F_T$.

3.2 SOLUTION TECHNIQUE

The algorithm used for the numerical solution is given in Appendix A. The reduced velocity, $U_r = U_o/\omega l_o$, is calculated for a given dimensionless velocity , $U_f = U_p/f_n d$, by using the following relationship :

$$U_r = U_f/K_u = \frac{U_p}{f_n d}\left[\frac{1}{1_o^* A_o^*}\right]\frac{\cos\alpha}{2\pi}(P_r - 1) \qquad (3.13)$$

where, U_p is the pitch velocity, and K_u is the proportionality constant that depends on the array geometry. This equation follows from continuity and the resultant geometric relationship between the minimum gap velocity, U_o, and the pitch velocity, U_p. The remaining formulation and some details of the solution technique are given below.

3.2.1 Determination of System Parameters

In order to show the natural evolution of the present analysis from the Lever & Weaver theory, to start with, the same system parameters used by Lever and Weaver will be used. This way, the numerical solution can be tested and the effects of new additions to the theory can be determined. Table 3.1 shows the system parameters used by Lever and Weaver for various array geometries. These parameters together with the phase and decay functions, will be used to determine the area fluctuation along the streamtube.

3.2.2 Phase and Decay Functions

Lever and Weaver [24] assumed that the phase lag, $\phi(s)$, based on a hydraulic transient analogy, could be expressed as :

Configuration	α	A_o^*	s_1^*	β_1	β_2
In-Line Square	0°	$P_r - 1$	$P_r * ROW$	11.5°	11.5°
Parallel Triangle	30°		$P_r \alpha * ROW$	α/P_r	α/P_r
Rotated Square ($P_r \le 1.7$)	45°			α/P_r	α/P_r
Rotated Square ($P_r > 1.7$)	45°	$P_r \cos(\alpha) - 0.5$	$\frac{1}{\pi}\int_0^\pi [(1+(\frac{\pi}{4l})^2 \sin^2\epsilon]^{\frac{1}{2}} d\epsilon$	α/P_r	α/P_r
Rotated Triangle	60°			α/P_r	α/P_r

$l_o^* = 8/3s_1^*$, $s_a^* = -\sin(\beta_1)/2$, $s_s^* = \sin(\beta_2)/2$

$ROW = 1.5$
$\omega/\omega_n = 1.0$

Table 3.1 Lever and Weaver's [25] Model Parameters for Various Arrays

$$\phi(s) = \frac{\omega_n l_0}{U_0} \frac{s+s_a}{s_1-s_a} = \frac{1}{U_r} \frac{s+s_a}{s_1-s_a} \quad , \qquad s < -s_a$$

$$= 0 \qquad\qquad , \qquad -s_a \le s \le s_s \tag{3.14}$$

Note that they set the phase lag to zero in the attached flow region. Physically, this means that the area perturbations in this region are created instantaneously with tube displacement. The form of this phase function is very important and should be studied experimentally. As no guidance is available from experiments, the function proposed by Lever and Weaver will be adopted here for the time being.

A basic inconsistency in the Lever and Weaver model is that the effect of a disturbance is assumed to be limited to 1.5 tube rows upstream and downstream of the flexible tube, yet the magnitude of the area perturbation is assumed constant over this range. Additionally, the velocity and pressure fluctuations at the streamtube inlet (initial conditions) are assumed to be zero. This is also inconsistent with the assumption of constant area perturbation along the streamtube. These inconsistencies can be overcome by introducing an area decay function, f(s), as given in equation (3.4). A form for this function which satisfies the requirement of constant area perturbation over the flow attachment range, $-s_a < s < s_s$, and becomes asymptotic to zero for large $|s|$ is :

$$f(s) = \frac{1}{1 + B(-s_a - s)^A}, \qquad s < -s_a$$

$$= 1 \qquad\qquad -s_a \leq s \leq s_s \tag{3.15}$$

where B and A are constants to be chosen to suit the boundary conditions. It is to be noted that this is a mathematical artifice introduced to overcome inconsistencies discussed above. The concept can be justified qualitatively on physical grounds as disturbances must vanish at some distance from the source. However, there is no experimental evidence on which a better approximation can be based.

This area decay function is plotted in figure 3.5 for A = 10 and values of B which give the decay of 99%, that is $f(-s_1^*) = 0.01$, and no decay (Lever & Weaver's model), $f(-s_1^*)=1.0$, at the streamtube inlet, $-s_1^*$. The latter represents the distance upstream and downstream within which a significant disturbance occurs and is assumed to be 1.5 tube rows in figure 3.5. This value is somewhat arbitrary and was used so that a direct comparison with the previous results of Lever and Weaver could be made.

Given the phase (3.14) and decay functions (3.15) and the total area fluctuation at the minimum gap, upstream fluctuations can be determined by using equation (3.4).

3.2.3 Area Perturbation in the Attached Flow Region :

Up to this point in the development, the model is applicable to any array geometry. However, as discussed in

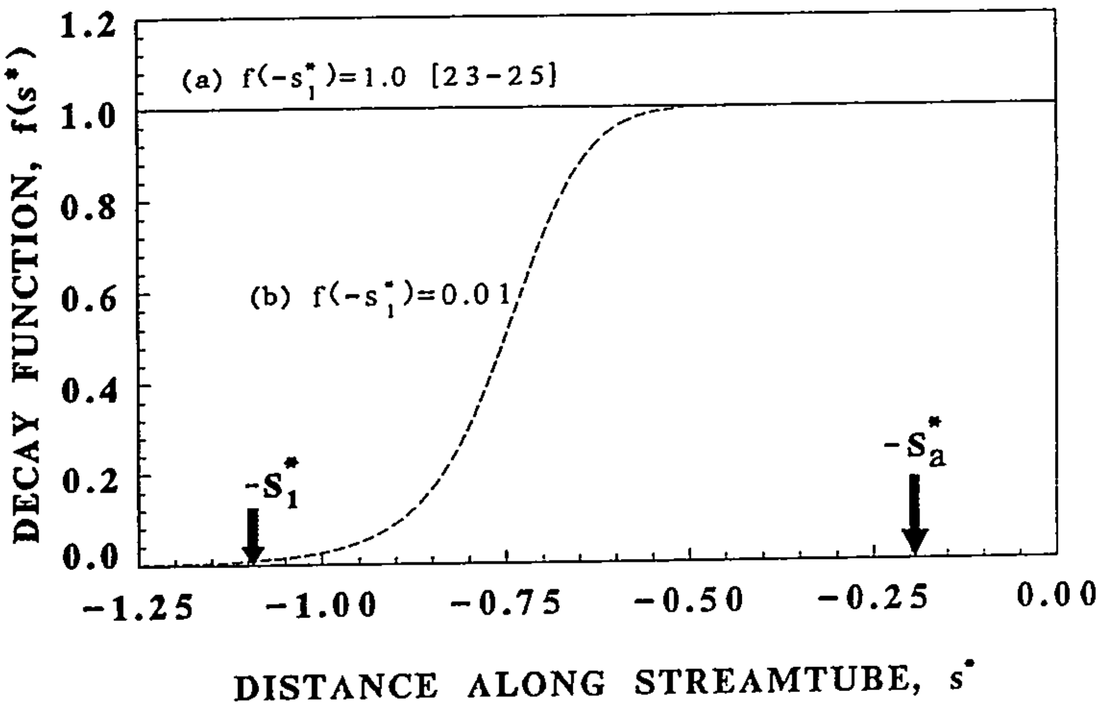

Figure 3.5 Area Decay Function (a) Lever & Weaver (b) Present Study

section 3.1, the streamtube area is determined by the minimum flow area through the array and this is array geometry dependent. As a result, the area perturbation in the attached flow region is array dependent as well. This area perturbation in the attached flow region can be determined from the idealized streamtube geometries. It is assumed that the streamtubes in the upstream area cannot differentiate between the fluctuations created by the streamwise and transverse directions. Hence, given the fluctuation at the minimum gap, upstream fluctuations can be determined as explained in section 3.2.2.

Transverse Vibration : If a flexible tube moves only in the transverse direction, the streamtube area perturbation is approximately constant along the attached flow region and equal to the streamtube area perturbation at the minimum flow gap. This is a reasonable assumption and can be verified from the geometry of the idealized streamtubes. If the flexible tube moves in the transverse direction a distance $y(t)$, for the parallel triangular and the rotated square arrays with $P_r \leq 1.7$, the perturbation at the minimum gap can be approximated by $y(t)\cos(\alpha)$ as shown in figure 3.6(a). This approximation introduces negligible error for small amplitude tube vibrations. Typically, the vibration amplitude of the heat exchanger tube is less than 2% of the tube diameter at the onset of instability. Therefore, the assumption of small amplitude vibration is valid. In in-line square arrays, $\alpha = 0^{\circ}$ and the magnitude of the minimum gap perturbation would be $y(t)$. On the other hand, in normal triangular and rotated square arrays with $P_r > 1.7$, the perturbation of the minimum streamtube

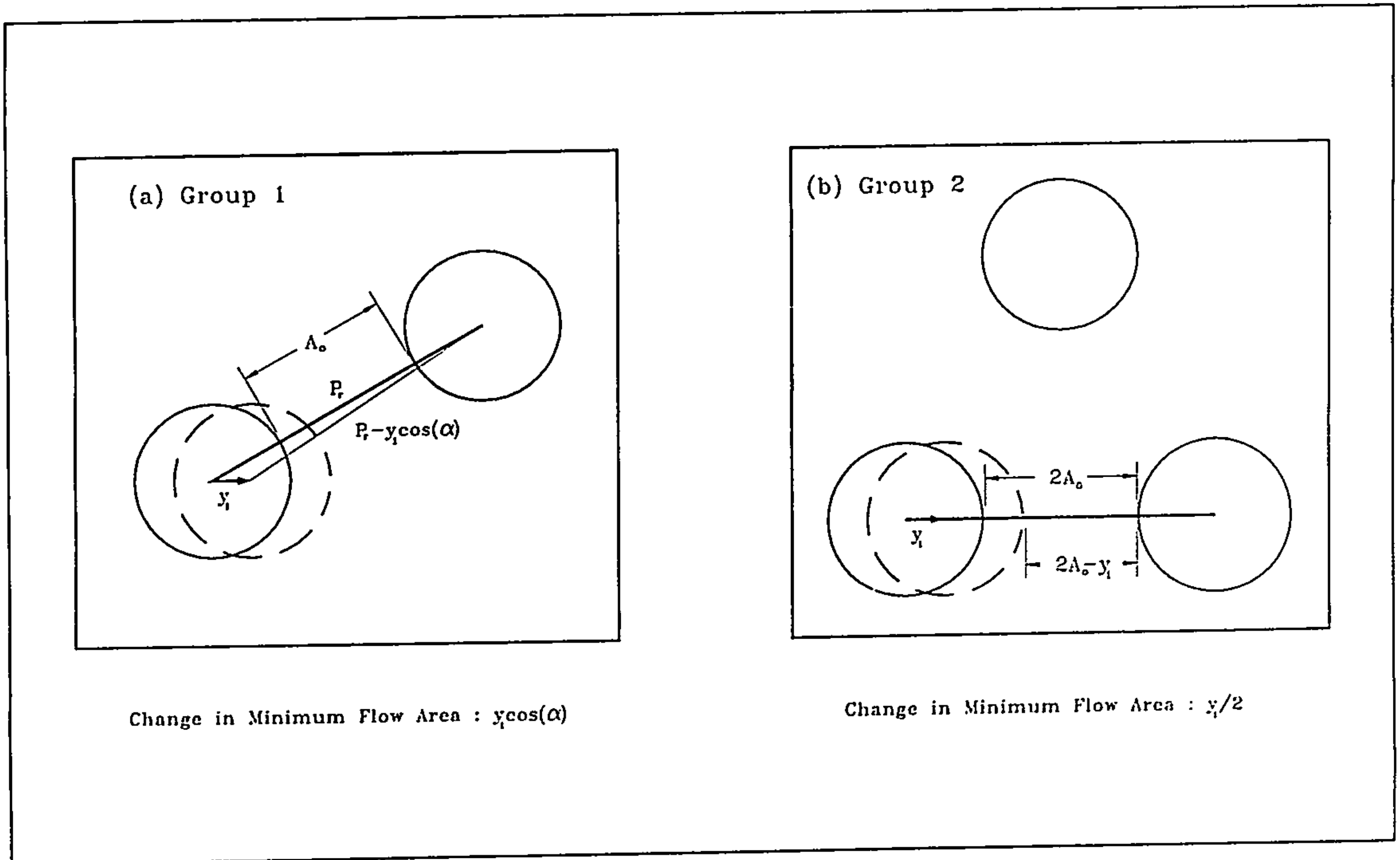

Figure 3.6 Area Perturbation at the Minimum Flow Area for (a) Group 1 arrays, (b) Group 2 arrays

area is $y(t)/2$ (see figure 3.6(b)) This is because of the overlapping of two streamtubes at $s = 0$. Thus, the mean flow area is actually two streamtubes wide and, to allow for the same theoretical definition of A_o, the perturbation is taken as half the value of the amplitude of the tube vibration. When the magnitude of these perturbations are examined carefully, a general formula for the area perturbation function in the attached flow region can be found for all the tube arrays as follows:

$$a_y(s,t) = y(t)\cos(\alpha) \;, \qquad -s_a < s < s_s \tag{3.16}$$

It must be noted that this formula introduces some error in rotated square arrays with $P_r > 1.7$, but it is believed that this error doesn't affect the overall results significantly. This expression is different than Lever and Weaver's model by a factor of $\cos(\alpha)$. In that model it was assumed that the area fluctuation in the attached flow region is constant and equal to $y(t)$ regardless of the pitch angle, α.

<u>Streamwise Vibration :</u> If the tube moves only in the streamwise direction $x(t)$ amount, the area perturbation at $\beta = \alpha$ would be $x(t)\sin(\alpha)$. In this case, constant area perturbation in the attached flow region is not valid, since the perturbation changes from $x(t)\sin(\alpha)$ at $s = -s_m$ to $-x(t)\sin(\alpha)$ at $s = s_m$. This can be concluded directly from the geometry of the idealized streamtubes. Again, using the streamtube geometry, the area perturbation in the attached flow region can be obtained as:

$$a_x(s,t) = x(t)\sin(2s/P_r) \tag{3.17}$$

This formula is valid for all the tube arrays except the in-line square arrays where $a_x(s,t) = 0$. Physically, this means that in an in-line square array, there is no static and dynamic instability expected for a single flexible tube allowed to move only in the streamwise direction.

Transverse and Streamwise Vibrations : If the tube is moving both in transverse and streamwise directions, the total area perturbation of the streamtube 1, in the attached flow region, would be the superposition of equations (3.16) and (3.17). That is :

$$a_1(-s,t) = x(t)\sin(2s/P_r)\delta(\alpha) - y(t)\mathrm{Cos}(\alpha) \qquad (3.18)(a)$$

Similiarly, for the streamtube 2;

$$a_2(-s,t) = x(t)\sin(2s/P_r)\delta(\alpha) + y(t)\mathrm{Cos}(\alpha) \qquad (3.18)(b)$$

where, $\delta(\alpha) = 1$, if $\alpha \neq 0$
$= 0$, if $\alpha = 0$ (in-line square arrays)

At $s = -s_m$, equations 3.18 reduces to :

$$a_1(-s_m,t) = x(t)\sin(\alpha)\delta(\alpha) - y(t)\mathrm{Cos}(\alpha) \qquad (3.19)(a)$$

$$a_2(-s_m,t) = x(t)\sin(\alpha)\delta(\alpha) + y(t)\mathrm{Cos}(\alpha) \qquad (3.19)(b)$$

3.2.4 Uncoupling of Transverse and Streamwise Motions

Substituting the area perturbations at the minimum gap, $s = -s_m$ in equation (3.19), into the equations of motion, equations (3.12), yields :

$$\left.\begin{aligned} &\text{(a)} \quad m\ddot{x}(t) + c\dot{x}(t) + kx(t) = 2x(t)F_x \sin(\alpha)\delta(\alpha) \\ &\text{(b)} \quad m\ddot{y}(t) + c\dot{y}(t) + ky(t) = 2y(t)F_y \cos(\alpha) \end{aligned}\right\} \quad (3.20)$$

Note that the equations of motion are uncoupled. This means that the stability of the tube in the streamwise and longitudinal directions may be analyzed separately.

3.2.5 Determination of Velocity and Pressure Fluctuations

As mentioned earlier, the fluid in the upstream region cannot differentiate between the fluctuations created by streamwise and transverse motions. Therefore, in order to avoid repeating the same calculation twice, one for the streamwise motion and the other for the transverse motion, the area perturbation is set to unity at the minimum gap. The desired values of the fluctuating fluid forces acting on the vibrating tube is then found by multiplying the fluid force (determined by setting the area perturbation to unity) by the minimum gap area perturbation.

Once the area perturbations in the upstream and the attached flow region are determined, velocity fluctuations can be found from the continuity equation (3.7). At this point in the analysis, the frequency ratio, ω/ω_n, is not known yet. Hence, the velocity fluctuation is found as :

$$u^{\bullet}(s) = u_o^{\bullet}(s) + \left(\frac{\omega}{\omega_n}\right)u_1^{\bullet}(s)/U_r \quad (3.21)$$

By substituting the velocity fluctuation (3.21) in the momentum equation (3.10), pressure fluctuations can be obtained as given below:

$$p^*(s) = p_o^*(s)/U_r + (\frac{\omega}{\omega_n})p_1^*(s) + (\frac{\omega}{\omega_n})^2 p_2^*(s)\cdot U_r \qquad (3.21)$$

The unsteady fluid force acting on the vibrating tube is then found by integrating the pressure along the attached flow region (equation 3.12). This force will be in the form :

$$F^*(s) = F_o^*(s)/U_r + (\frac{\omega}{\omega_n})F_1^*(s) + (\frac{\omega}{\omega_n})^2 F_2^*(s)\cdot U_r \qquad (3.23)$$

3.2.6 Nondimensionalized Equations of Motion

Assuming that the tube oscillates at the same frequency in the x and y directions with a phase difference, φ, the motion can generally be described by :

$$\left.\begin{aligned} y(t) &= Ye^{i\omega t} \\ x(t) &= Xe^{(i\omega t+\varphi)} \end{aligned}\right\} \qquad (3.24)$$

where, ω is the complex frequency of oscillation. Of course, since the equations of motion are uncoupled, the phase relationship, φ, is of no consequence in the present analysis. Substituting solutions (3.24) into the equations of motion (3.20), introducing the variables $c = m\delta\omega_n/\pi$, $k = \lambda m\omega_n^2$, and nondimensionalizing, yields :

$$\left.\begin{array}{ll}\text{(a)} & -\dfrac{m}{\rho d^2}\left(\dfrac{\omega}{\omega_n}\right)^2+\dfrac{i}{\pi}\dfrac{m\delta}{\rho d^2}\left(\dfrac{\omega}{\omega_n}\right)+\dfrac{m}{\rho d^2}=2F_x^* l_0^* U_r(\sin\alpha) \\ & \text{and,} \\ \text{(b)} & -\dfrac{m}{\rho d^2}\left(\dfrac{\omega}{\omega_n}\right)^2+\dfrac{i}{\pi}\dfrac{m\delta}{\rho d^2}\left(\dfrac{\omega}{\omega_n}\right)+\dfrac{m}{\rho d^2}=2F_y^* l_0^* U_r(\cos\alpha)\end{array}\right\}\quad(3.25)$$

Both the theoretical results of this model (see section 3.3.5) and experiments show that transverse vibrations are potentially more dangerous than streamwise vibrations. Hence, only the motion in transverse direction will be considered below.

3.2.7 Characteristic Equation

Introducing the following transformation (3.26)

$$\overline{F}=2l_o^* U_r \cos(\alpha)\ F^*(s)=\overline{F}_o U_r^2+\left(\frac{\omega}{\omega_n}\right)\overline{F}_1 U_r+\left(\frac{\omega}{\omega_n}\right)^2\overline{F}_2 \qquad (3.26)$$

equation (3.25) can be rearranged to obtain :

$$\frac{m}{\rho d^2}=\frac{\overline{F}_o U_r^2+\left(\frac{\omega}{\omega_n}\right)\overline{F}_1 U_r+\left(\frac{\omega}{\omega_n}\right)^2\overline{F}_2}{-\left(\frac{\omega}{\omega_n}\right)^2+1+i\,\frac{\delta}{\pi}\left(\frac{\omega}{\omega_n}\right)} \qquad (3.27)$$

This is the characteristic equation of the theoretical model. Given the reduced velocity, U_r, and the geometric parameters of the array, F_o, F_1 and F_2 can be determined as mentioned earlier. The solution of the characteristic equation (3.27) gives the frequency ratio, ω/ω_n and the mass ratio, $m/\rho d^2$, from which the mass-damping parameter is obtained.

The flexible tube is assumed to be moving sinusoidally as given by equation (3.24). In general, ω is a complex number, so that $\omega = \omega_R + i\omega_I$. Here, ω_I represents the exponential decay or growth of the amplitude of motion in time, whereas ω_R represents the oscillatory frequency. Table 3.2 summarizes the behavior of the vibratory motion of a heat exchanger tube depending on the complex frequency. When ω_R is non-zero and ω_I changes sign from positive to negative, dynamic instability starts. At the dynamic instability threshold, $\omega_R \neq 0$ and $\omega_I = 0$. When ω_R is zero, there is no oscillatory motion. In this case, static instability occurs if ω_I is positive. At the static instability threshold, $\omega_R = \omega_I = 0$. Note that the imaginary part of the complex frequency is zero at both the static and dynamic instability thresholds.

At the stability thresholds of both the static and dynamic instabilities, ω_I is zero. Therefore, $\omega = \omega_R$ and ω/ω_n is a real number. As a result, the solution of equation (3.27) can be obtained by forcing the mass-damping parameter , $m\delta/\rho d^2$ and the frequency ratio, ω/ω_n to be real numbers. For this purpose, an iterative type of solution procedure is adopted to solve equation (3.27). As an initial assumption $\omega/\omega_n=1$ is assumed. Then equation (3.26) is evaluated and the resultant force coefficient is used in equation (3.27) to determine the actual ω/ω_n and $m/\rho d^2$. If ω/ω_n varied from its initial assumed value, equation (3.26) is evaluated again with the updated value and iterations are performed until the difference between the initial and final values of ω/ω_n is within 0.01%. It was found that the convergence is very fast.

$$y = y_0 e^{i\omega t} \quad , \quad \omega = \omega_R + i\omega_I$$

ω_R	ω_I	Behaviour	Implication
0	(+)	Exponential decay, no vibrations	Stable
$\neq 0$	(+)	Exponential decay, sinusoidal vibr.	Stable
0	(-)	Exponential growth, no vibration	Statically Unstable
$\neq 0$	(-)	Exponential growth, sinusoidal vibr.	Dynamically Unstable
0	0	No motion	Stat. Inst. Threshold
$\neq 0$	0	Constant amplitude sinusoidal vibr.	Dyn. Ints. Threshold

Table 3.2 The behavior of a structure as a function of it's complex frequency.

3.3 RESULTS AND DISCUSSION

As mentioned in the previous chapters, the analytical expressions (equations 3.7, 3.10, 3.11 and 3.26) were solved numerically. Although, it is possible to obtain the solution analytically, the resultant equations would be cumbersome, making basic changes to the model relatively difficult. To verify the computer code, Lever and Weaver's model was simulated for the parallel triangular array with a pitch ratio, P_r, of 1.375. This array was selected, because the analytical solution was reported by Lever and Weaver [25]. Using the same system parameters as Lever and Weaver, the numerical solution for the transverse instability is obtained (see figure 3.7). These results are essentially same as the analytical solution. Numerical error due to the finite integration step is less than 0.5% for the whole range. Hence, numerical error is negligible and the numerical solution is satisfactory.

Lever and Weaver's prediction of the dynamic instability in parallel triangular arrays is in good agreement with the experiments as shown in figure 3.7. They also report good agreement for in-line square arrays [25]. However, their prediction is not as good for the rotated triangular and rotated square arrays. In addition to this, qualitatively, there are inconsistencies between Lever and Weaver's theory and the experiments. These inconsistencies can be summarized as follows.

(1) In Lever and Weaver's model, static instability cannot be obtained from the dynamic instability solution. Theoretically, when the time dependent terms are eliminated from the

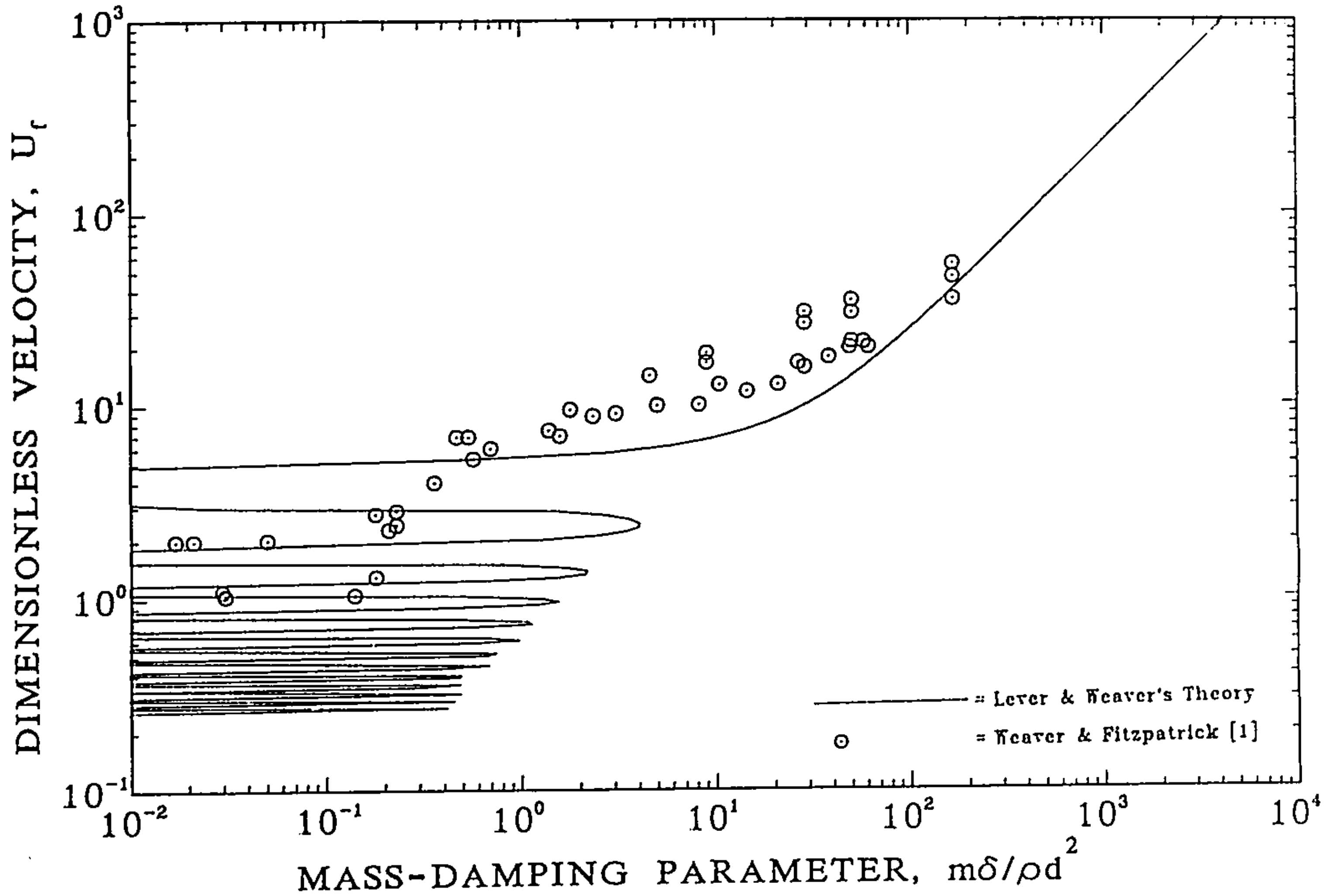

Figure 3.7 Lever & Weaver's Prediction of Dynamic Instability for Parallel Triangular Arrays with P -1.375 (Obtained Numerically)

governing equations , static instability is obtained. This is not the case in Lever and Weaver's theory where they used a different model to predict the static instability.

(2) Other theoretical studies based on the experimental data report that the slope of the dynamic instability curve approaches 1/2 at high dimensionless velocities. This means that :

$$U_p/f_n d = K\ (m\delta/\rho d^2)^{1/2} \tag{3.28}$$

Lever and Weaver's model predicts a slope of 1 from the dynamic instability curve in figure 3.7. That is:

$$U_p/f_n d = K\ (m\delta/\rho d^2)\ . \tag{3.29}$$

This discrepancy has to be explained.

(3) At low values of dimensionless velocities, typically $U_p/f_n d < 5$, a large number of unstable regions are predicted. Experiments [48] show that there is, in fact, a second instability region in this area, but there is no evidence that the number of unstable regions is greater than two. It should be noted that the same multiple instability regions are obtained by Price & Paidoussis' [10-13]. This phenomena will be explained in section 6.2.

3.3.1 Effect of Area Decay Function

It is found that the reason Lever and Weaver's theory is incapable of predicting static instability from the dynamic model is the inconsistent boundary conditions at the inlet of the streamtube. They assumed that the effect of a disturbance is limited to 2 tube rows upstream and downstream of the flexible tube, and the magnitude of the area perturbation was assumed constant over this range. Additionally, the velocity and pressure fluctuations at the streamtube inlet, $s = -s_1$ were assumed to be zero. This is not consistent with the assumption of constant area perturbation along the stream tube. As a result, in an attempt to determine the static instability from the dynamic model, when the frequency ω was set to zero, there was a uniform area perturbation along the streamtube while the velocity and pressure perturbations were uniform (i.e., area, velocity and pressure perturbations do not vary along streamtubes). The values of these uniform velocity and pressure were set by the inlet values at the streamtube inlet and were equal to zero. It follows that the static force acting on the flexible tube is zero, and hence no static instability could be predicted.

Theoretically, if velocity and pressure fluctuations are zero, there should be no area perturbation. Since, velocity and pressure fluctuations are assumed negligible and set to zero at the streamtube inlet, the magnitude of the area perturbation must be set to a negligible value. The area decay function determines the magnitude of the area perturbation as a function of the position along a streamtube. A proper selection of this function ensures that the magnitude of the area perturbation is negligible (1% of the perturbation at the minimum gap) at the streamtube inlet. With the introduction of the decay function, f(s), the boundary conditions at the streamtube inlet becomes consistent and static instability can be obtained from the dynamic model by setting the frequency ratio, ω/ω_n=0. Results for the parallel triangular array with P_r=1.375 are shown in figure 3.8. Except for the introduction of the decay function, the same system parameters that Lever & Weaver used are used for comparison purposes. When obtaining the dynamic instability the frequency ratio, ω/ω_n, is forced to take the value of 1 as Lever & Weaver did.

The decay function, while satisfying the inlet boundary conditions, also reduces the fluid inertia that plays an important role in dynamic instability. Hence, the present solution for the dynamic instability is affected significantly with the introduction of the decay function. However, the solution for the static instability is very close to Lever and Weaver's static instability solution. This is because of the fact that the static instability is dominated by the area change in the attached flow region and the decay in this region is negligible.

Unfortunately, with the introduction of the decay function, quantitative agreement between the theory and the experiments is not good when the Lever and Weaver parameter values are used. The following sections will outline the further development of this theoreticel model.

3.3.2 The Effect of Relaxing the Frequency Ratio, ω/ω_n

As mentioned above, at the stability threshold, the frequency of vibration, ω, and hence the frequency ratio, ω/ω_n, has to be a real number. Similarly, for a realistic solution, the

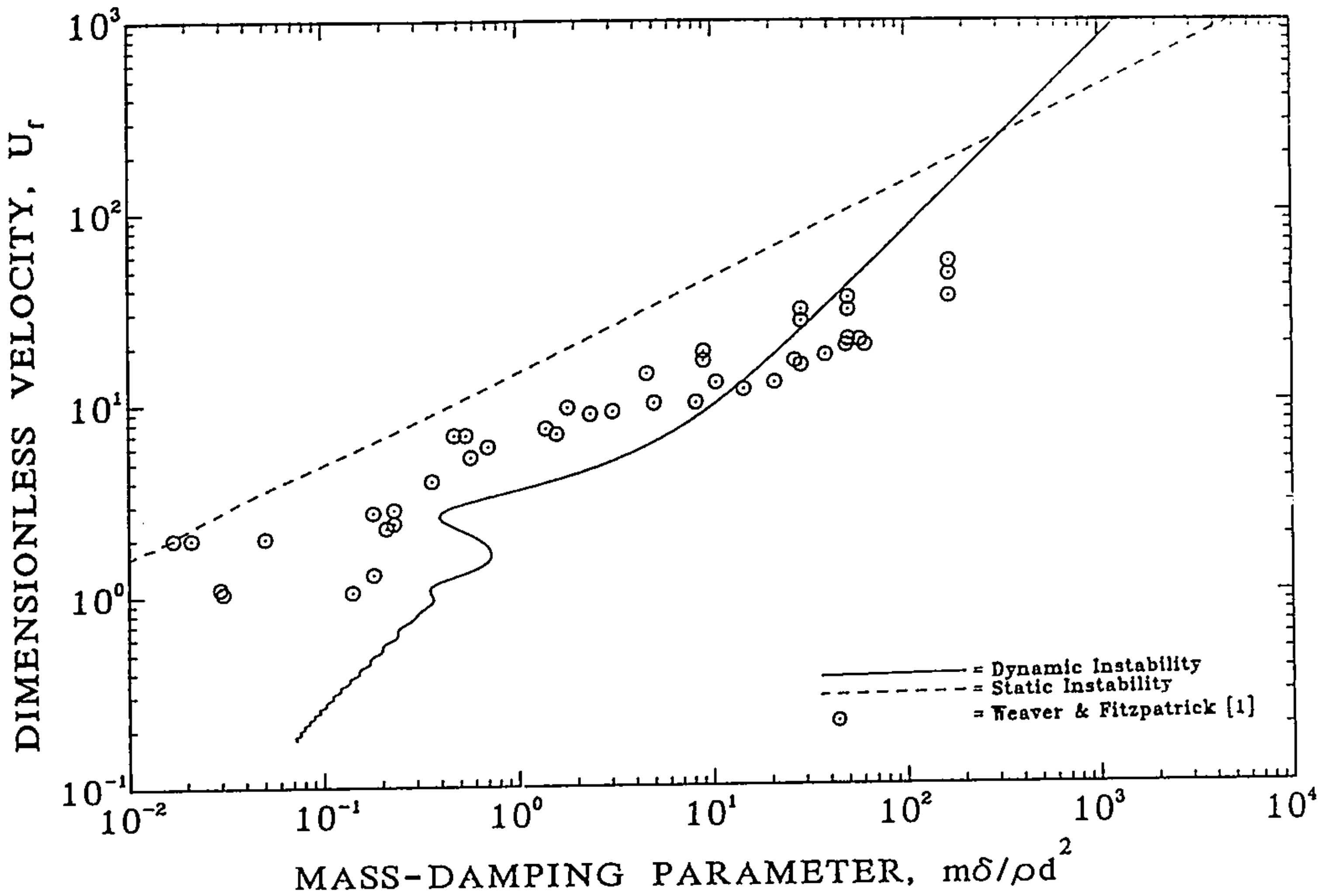

Figure 3.8 Effect of Area Decay Function on Transverse Dynamic Instability

mass ratio has to be real as well. On the other hand, the right hand side of equation (3.25) is a complex expression that accommodates the phase difference between the tube motion and the fluid force acting on the tube. Therefore,

$$\frac{m}{\rho d^2} = \frac{F_R + iF_I}{1-(\frac{\omega}{\omega_n})^2 + i\frac{\delta}{\pi}(\frac{\omega}{\omega_n})} \tag{3.30}$$

where, $F_R = 2l_0^{*}U_r(\mathrm{Sin}\alpha)\mathrm{Real}(F_x^{*})$,

$F_I = 2l_0^{*}U_r(\mathrm{Sin}\alpha)\mathrm{Imaginary}(F_x^{*})$.

Traditionally, the theoretical models in the literature assume that the frequency of oscillation at the onset of instability is equal to the natural frequency of the heat exchanger tube (either in vacuum [6-13] or in still fluid [23-25]). That is $\omega/\omega_n = 1$. This is a reasonable assumption supported by experimental observations. However, when $\omega/\omega_n = 1$ is substituted into equation (3.30), this assumption introduces an error in determining the dynamic instability threshold. Equation (3.30) reduces to the following equation when $\omega/\omega_n = 1$:

$$\frac{m}{\rho d^2} = \frac{F_R + iF_I}{i\frac{\delta}{\pi}} \tag{3.31}$$

Since the denominator on the right hand side is an imaginary number, in order to obtain a real valued mass ratio, $m/\rho d^2$, the numerator of the right hand side has to be an imaginary number as well. Previous researchers [3-29] neglected the real component of the numerator, F_R to obtain the solution:

$$\frac{m\delta}{\rho d^2} = \pi \cdot F_I \tag{3.32}$$

However, at large values of the mass-damping ratio, $m\delta/\rho d^2$, F_R is larger than F_I and neglecting F_R introduces an error. This error can be avoided if the frequency ratio, ω/ω_n is relaxed and obtained by solving (3.30). Figure 3.9 shows the effect of relaxing the frequency ratio. The dynamic stability solution departs from that obtained with $\omega/\omega_n = 1$ at a value of $m\delta/\rho d^2$ of about 200 and approaches the static stability solution at very high mass-damping ratios, implying that the fluid stiffness force, F_R, is much larger than the fluid damping force, F_I. In this range, the frequency ratio approaches zero (see figure 3.9). In the limiting case when the fluid damping force is equal to zero, the frequency ratio would be zero and the structure would go statically unstable. It is noteworthy that over a large range of the mass-damping parameter, the frequency ratio is very nearly equal to unity and hence very little error was introduced by assuming $\omega/\omega_n \cong 1.0$. Another important effect is that the slope of the stability curve now approaches 0.5 as predicted by other theories. In all calculations in the following sections, the frequency ratio is relaxed and obtained as outlined above.

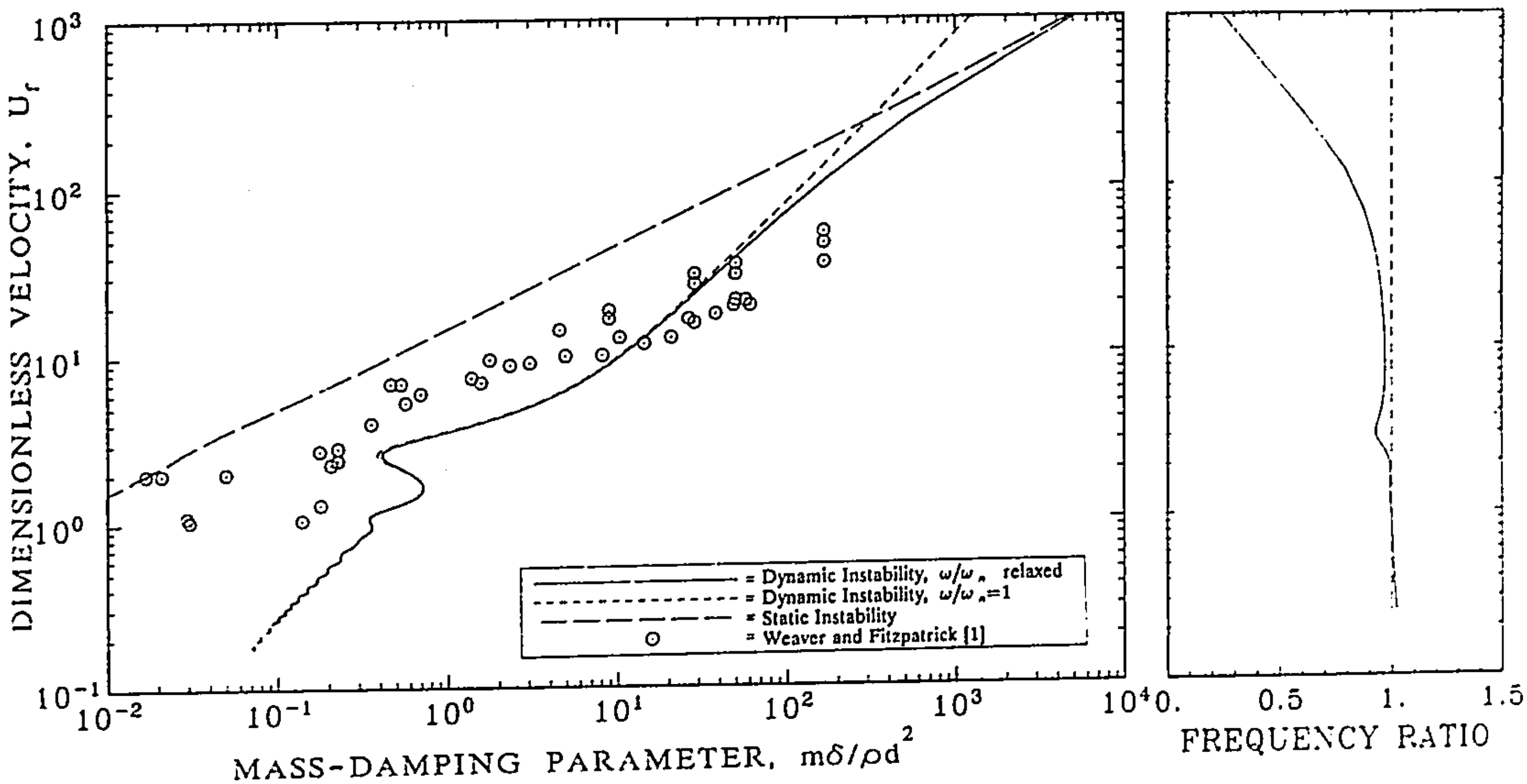

Figure 3.9 Effect of Relaxing the Frequency Ratio, ω/ω_n.
(a) $\omega/\omega_n=1$, (b) ω/ω_n relaxed.

3.3.3 Effect of Curvilinear Coordinates

Lever & Weaver's model showed good agreement with the experiments for the parallel triangular and the in-line square arrays. However, agreement wasn't as good for the rotated square and rotated triangular arrays. It was thought that the reason for this might be the torturous flow path that cannot be modelled properly with linear one-dimensional flow equations. Curvilinear coordinates are used in the present analysis in the hope that the flow field can be modelled more realistically. It was found that it is the pressure gradient across a streamtube that makes the streamtube bend around a tube. This pressure gradient means that two-dimensional effects are important in areas where the flow field changes direction sharply. However, without introducing additional assumptions, these two-dimensional effects cannot be modelled properly. Such assumptions can not be justified at this stage of the present study. The formulation of the flow field is left as it is for the curvilinear coordinates in the hope that the above mentioned two-dimensional effects can be included in the future when a better understanding of two-dimensionality is gained.

The results with curvilinear coordinates are shown in figure 3.10 and are, as expected, essentially identical to the results shown in figure 3.9 where one-dimensional linear formulation is used.

3.3.4 2-D Results

As mentioned earlier, from the present analysis the

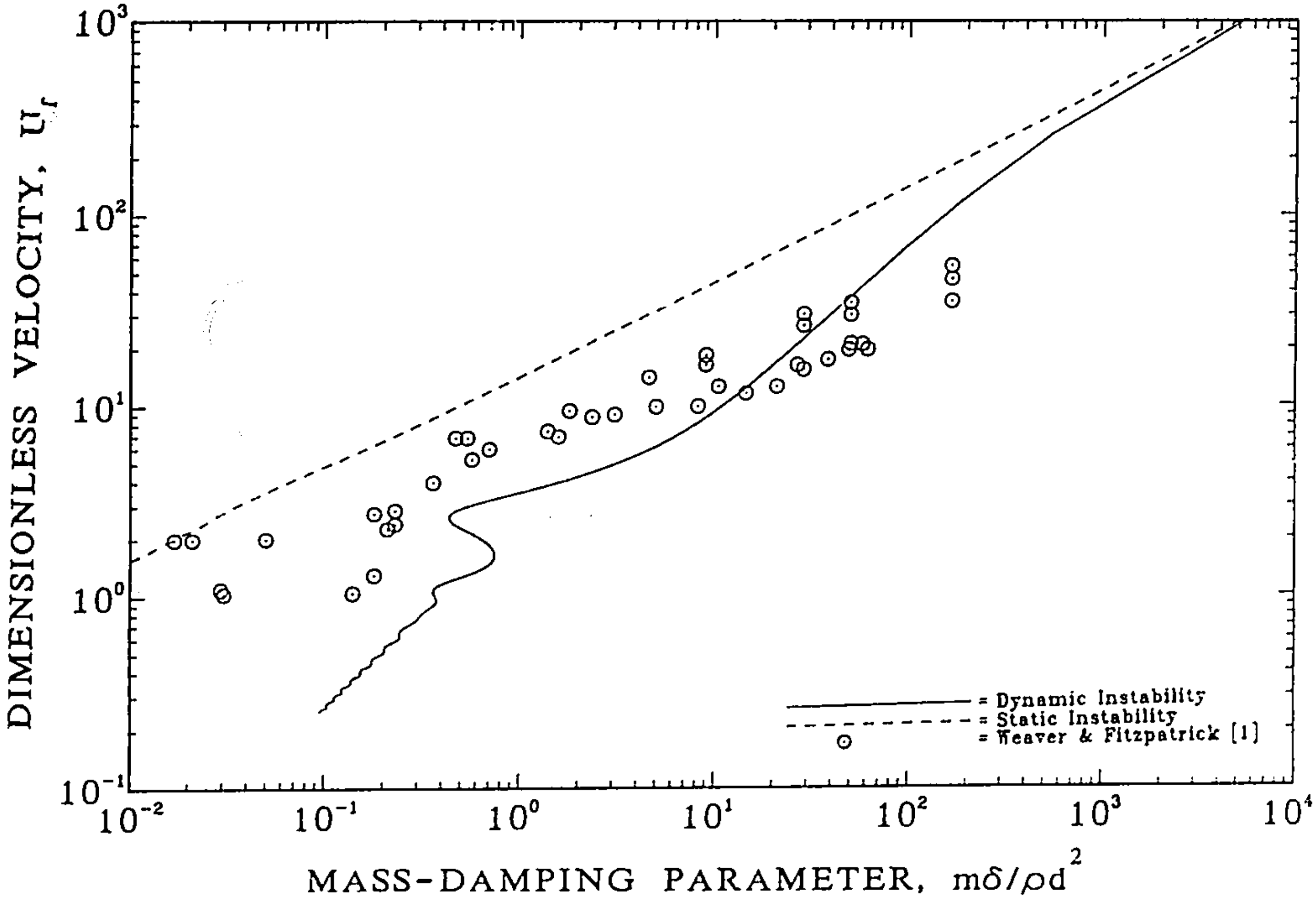

Figure 3.10 Effect of Curvilinear Coordinate System

streamwise and transverse vibrations are uncoupled. This is the result of not modelling the relative flow velocity with respect to the vibrating tube which would couple these vibration modes. At very low flow velocities, the relative flow velocity might be large enough to affect the overall results. However, it was felt that for the practical operating range of heat exchangers, this relative flow velocity effect may not be important. For example, the vector diagram for the $U_p/f_n d = 1$ is shown in figure 3.11. The relative flow velocity is only 1.6% higher than the absolute flow velocity and the angle θ is 7°. At higher dimensionless velocities, the effect of the relative flow velocity is even less important. At dimensionless velocities less than about 1, no instabilities have been observed for any tube array.

It is of course possible, that the streamwise motion of a tube is coupled with the transverse motion of the neighboring tubes as in the case of Connors' and Blevins' assumed mode shape [4,5]. This aspect can be explored in the multi-flexible tube analysis, since such an analysis would require the modeling of the effect of relative tube motion.

The results using curvilinear coordinates, the decay function and Lever & Weaver's parameters for the parallel triangular array with P_r= 1.375 are shown in figure 3.12. The vibration of the tube in the transverse and the streamwise directions are uncoupled as mentioned above. The results obtained are similar to Lever & Weaver's model. Streamwise dynamic instability is predicted neither by the present analysis nor by Lever & Weaver.

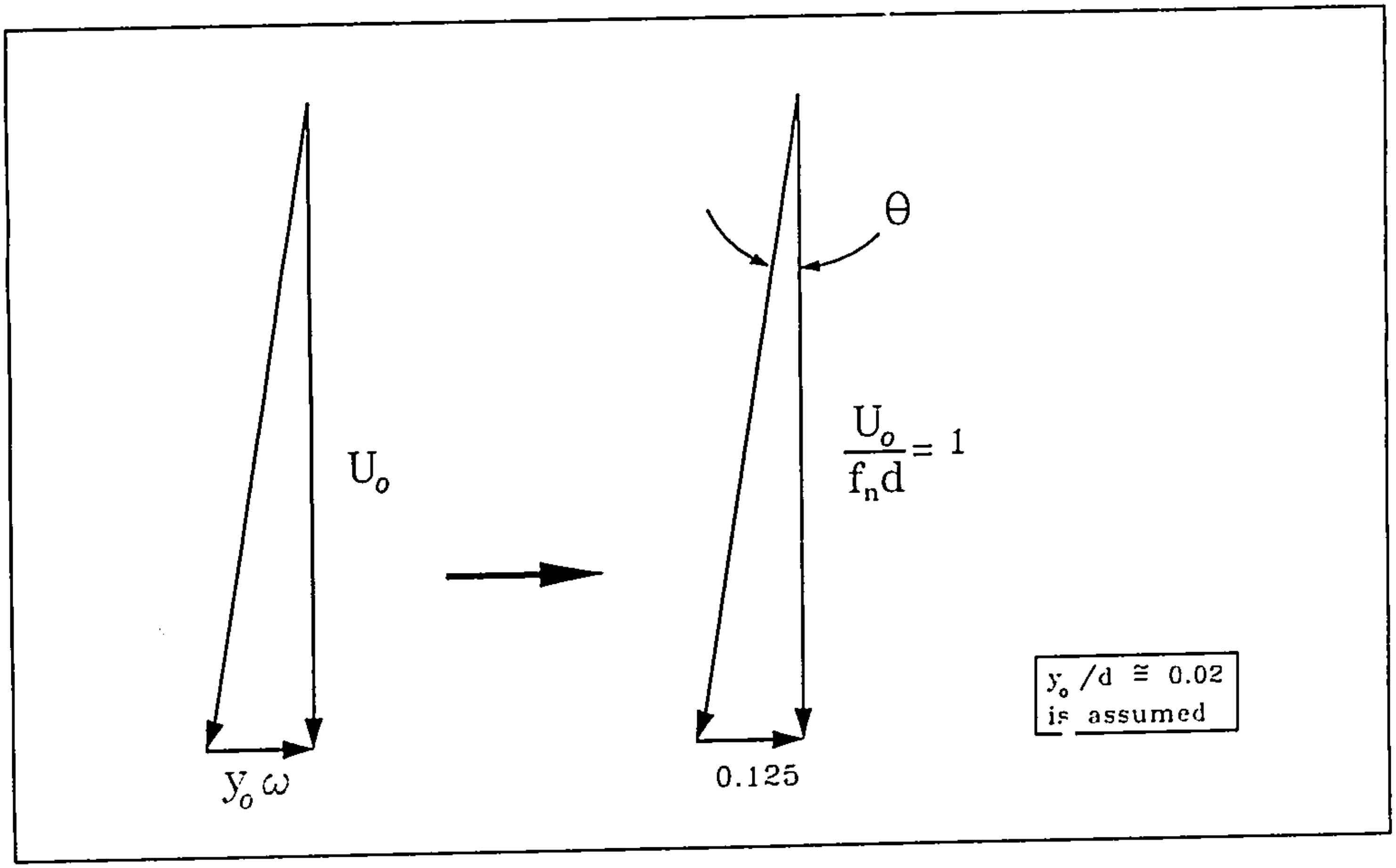

Figure 3.11 Relative Flow Velocity at $U_o/f_n d = 1$

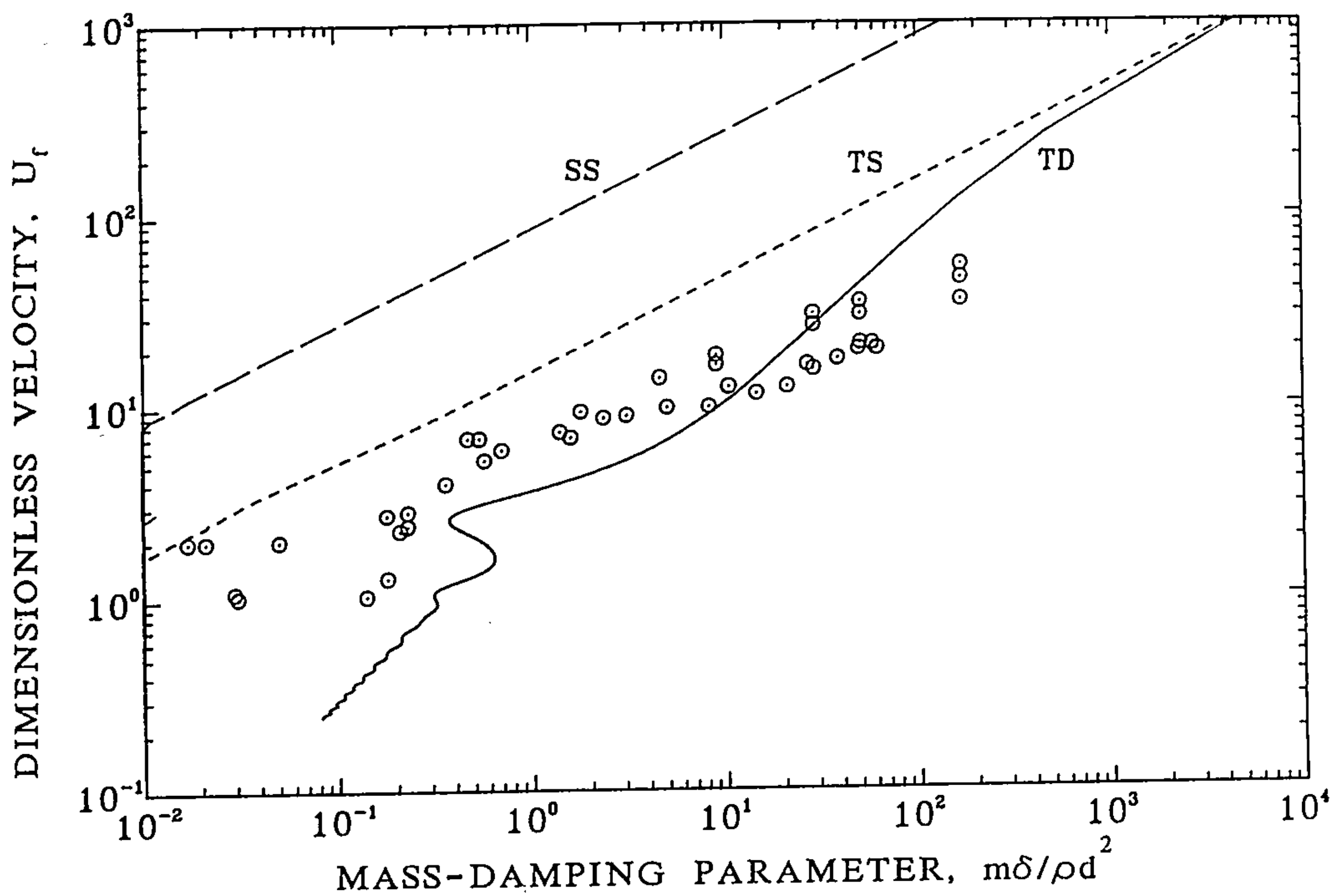

Figure 3.12 2-D Analysis : Predicted Stability Thresholds in Transverse and Streamwise Directions.
(TD - Transverse Dynamic; TS - Transverse Static)
(SD - Streamwise Dynamic; SS - Streamwise Static)

3.3.5 Effect of Attachment and Separation Points

Lever & Weaver assumed that the attachment and separation points are symmetric about s = 0, and the corresponding attachment and separation angles can be found by : $\beta_1 = \beta_2 = \omega/P_r$. Weaver & Abd-Rabbo's [42,43] and Scott's [44] flow visualization pictures show that these angles might be quite different than the proposed ones. They also observed little variation in attachment and separation angles when the pitch ratio was varied. Table 3.3 gives the observed values for various array geometries.

The results in figure 3.13 are obtained by using the attachment and separation angles listed in table 3.3 for the parallel triangular arrays. The rest of the parameters and the solution technique are the same as those used in figure 3.12. Note that the present analysis predicts dynamic instability in the streamwise direction when the experimental attachment and separation angles are used. This is because of the change in the net projected area of the tube surface subjected to fluid force. In the attached flow region, pressure fluctuations don't change significantly. Therefore, if $\beta_1 = \beta_2$, the projected area, and hence the fluctuating force component in the streamwise direction is zero. If $\beta_1 > \beta_2$, then there is a net fluctuating force component in the streamwise direction. Therefore, streamwise dynamic instability is possible. It is also found that transverse instabilities are almost always more critical than the streamwise instabilities. This conclusion is found to be correct for other array configurations as well.

The other important observation is that the choice of the

Configuration	α	β_1	β_2
In-Line Square	0°	20°	20°
Parallel Triangle	30°	40°	10°
Rotated Square ($P_r \leq 1.7$)	45°	75°	15°
Rotated Square† ($P_r > 1.7$)	45°	85°	15°
Rotated Triangle	60°	85°	15°

† Attachment and Separation angles for this array is assumed to be the same as Rotated Triangular arrays.

Table 3.3 Attachment and Separation Angles for Various Arrays (from [44])

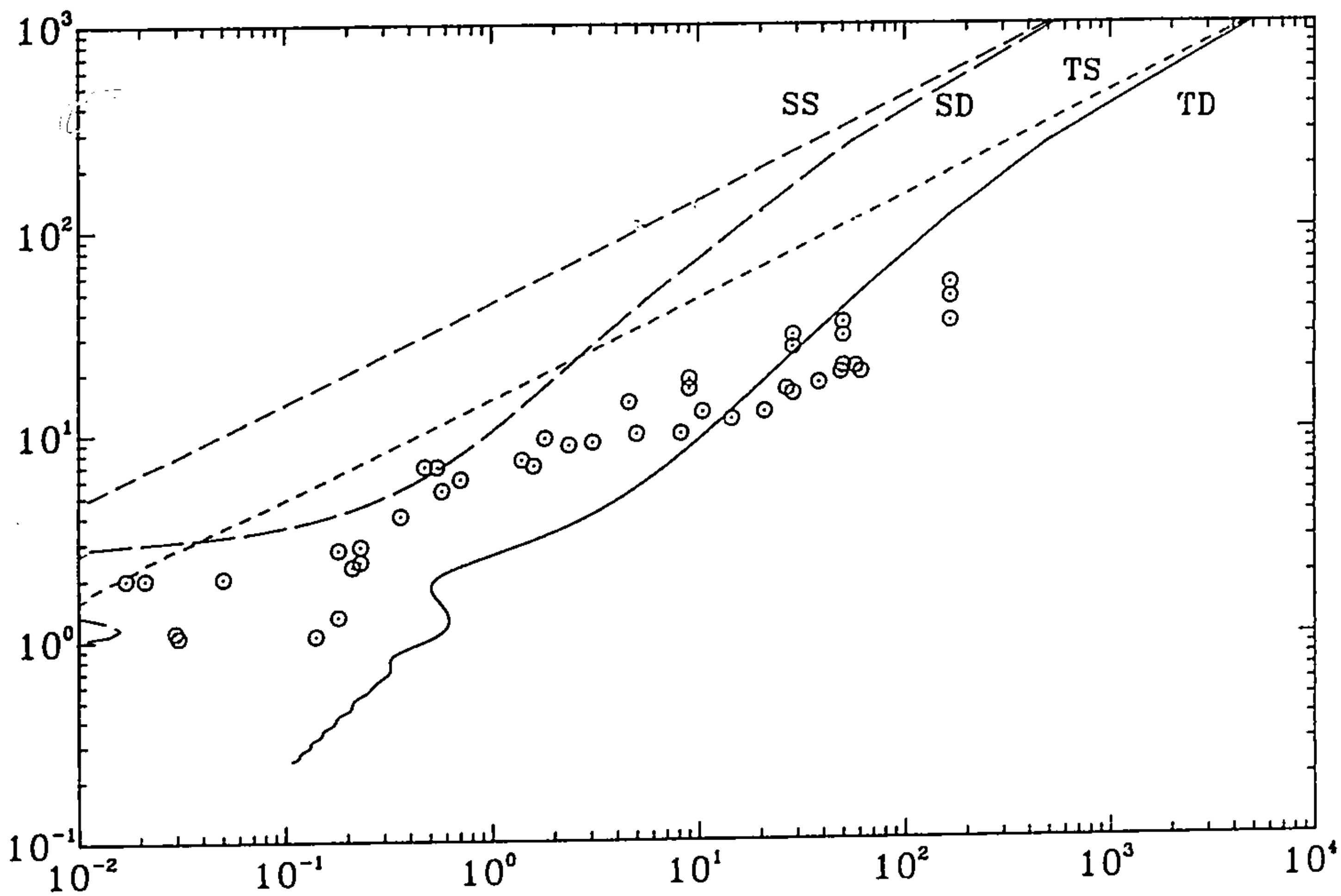

Figure 3.13 Effect of Attachment and Separation Points

attachment and separation angles doesn't effect the stability thresholds in the transverse direction significantly. Therefore, even if the reported values in Table 3.3 are in some error, the effect of this error on the overall result is not significant.

3.3.6 Phase Function

The phase function proposed by Lever and Weaver's later papers [24, 25] attains zero value in the attached flow region. Physically, this means that the area perturbation at the attached flow region due to the vibrating tube is created instantly, hence the fluid in attached flow region doesn't oppose the motion of the tube. This is a good approximation for the high mass-damping parameter range where the fluid inertia is very low and the fluid responds to the vibrating tube almost instantly. However, this assumption may not be valid at low mass-damping ratios where the fluid inertia is much larger. In addition, dynamic instabilities in this range are associated with low dimensionless velocities which means that the velocity of the vibrating tube with respect to the mean flow velocity, and hence the opposing fluid forces are larger. In short, due to large fluid inertia and low dimensionless velocities, it is expected that the fluid in the attached flow region contributes to the opposing forces in addition to the fluid in the upstream region. In order to model this, the phase function could be assumed to be non-zero in the attached flow region as well as upstream and downstream regions. For this purpose, the phase function proposed by Lever & Weaver [24-25] is modified so that that spatial variation of the phase function along a streamtube starts at s = 0. Hence, the phase function becomes :

$$\phi(s) = \frac{1}{U_r} \frac{s}{s_1} \tag{3.33}$$

Note that this is the same function proposed by Lever and Weaver in their early paper [23]. At high values of the dimensionless velocity, the phase function, $\phi(s)$, approaches zero, thus giving approximately zero values in the attached flow region. Therefore, the predictions at high values of the mass-damping parameter will not be affected significantly by using the phase function given by equation (3.33) instead of the one given by equation (3.14). The results for the parallel triangular arrays with the new phase function are presented in figure 3.14. All of the terms except the phase function are the same as the ones used to obtain figure 3.13. The results improved considerably at low values of the mass-damping parameter.

It should be noted here that the perturbation decay function is also modified to be consistent with the phase function so that the spatial decay starts at s = 0. This modification, however, does not affect the results significantly, since the decay function has a very flat profile in the attached flow region. The final form of the perturbation decay function, then, is as follows.

$$f(s) = \frac{1}{1 + B \cdot s^A} \tag{3.34}$$

where, A = 10 and $f(-s_1) = 0.01$.

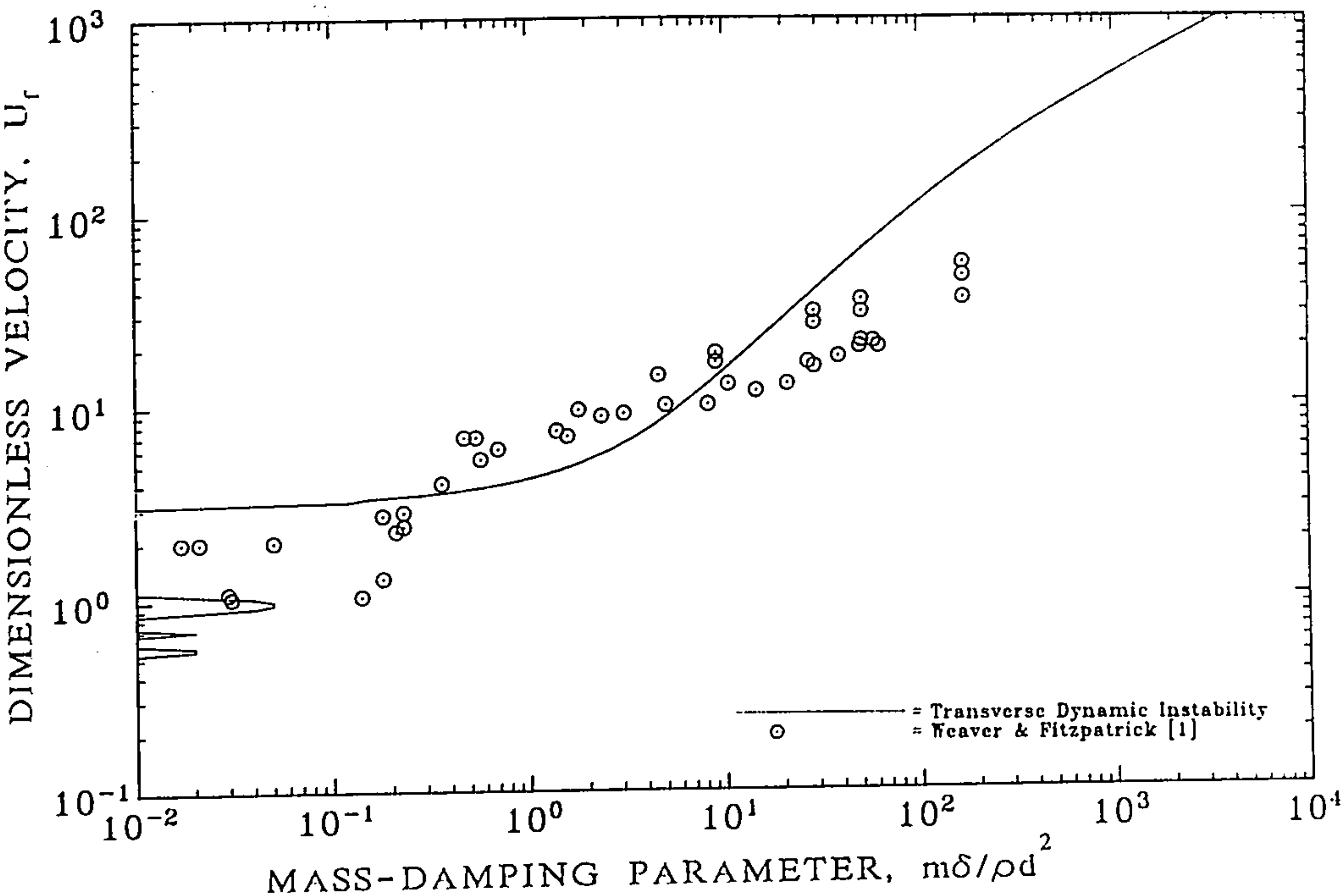

Figure 3.14 Effect of the Phase Function

CHAPTER 4

MULTIPLE TUBE VIBRATION ANALYSIS

The effect of neighboring tubes on the fluidelastic instability threshold has been a subject of controversy. Lever & Weaver's experiments [23] showed that the fully flexible tube array goes unstable at essentially the same velocity as a single flexible tube surrounded by rigid tubes. On the other hand, the semi-empirical theories of S.S.Chen [8] and of Price and Païdoussis [12, 13], show that at high values of the mass-damping parameter, multiple flexible tube vibration behavior is quite different from that of a single flexible tube in a rigid array. They report that the dominant fluid force is proportional to the relative displacement of neighboring tubes. This component plays an important role at high dimensionless velocities (high mass-damping parameter values), and is called a fluid-stiffness force. As a result of the neighboring tubes' motion, fluidelastic instability occurs at lower velocities in multiple flexible tube arrays than in the array with only a single flexible tube. It should be noted that these results are not necessarily in contradiction with Lever and Weaver's experimental results where measurements were taken at $m\delta/\rho d^2$=1.8. At this mass-damping value, the stiffness component of the fluid force is expected to have a small effect.

In order to determine the effect of the motion of neighboring tubes, the single flexible tube analysis is extended to a multi-flexible tube analysis in this chapter.

4.1 UNSTEADY FLUID FORCE COEFFICIENTS

It is assumed that only the immediate neighboring tubes have a direct effect on a tube. The same assumption is used by Tanaka & Takahara [14-16] and excellent agreement is found between their semi-empirical theory and the experiments. In the case of parallel triangular arrays, the center tube and four neighboring tubes are assumed sufficient to determine the forces acting on the tube at the center (see figure 4.1). It is, of course, possible to include the indirect effect of other tubes through the immediate neighboring tubes. This is explained in detail as follows.

The arrangement of the four flexible neighboring tubes (tubes #2,3,4 and 5) and the flexible center tube (tube #1) will be called a "unit cell" for tube #1 from now on. It is assumed that only these five tubes in the unit cell are directly responsible for the forces acting on the center tube in the unit cell.

Tanaka and Takahara [14] mechanically shook the center tube and measured the fluid forces acting on the stationary surrounding tubes by using strain gages attached to them. The phase difference between the fluid force acting on the center tube and the fluid force acting on one of the surrounding tubes is found by comparing the signals obtained from the respective tubes.

In the present analysis, the fluid forces acting on the tubes in the unit cell are obtained theoretically with the

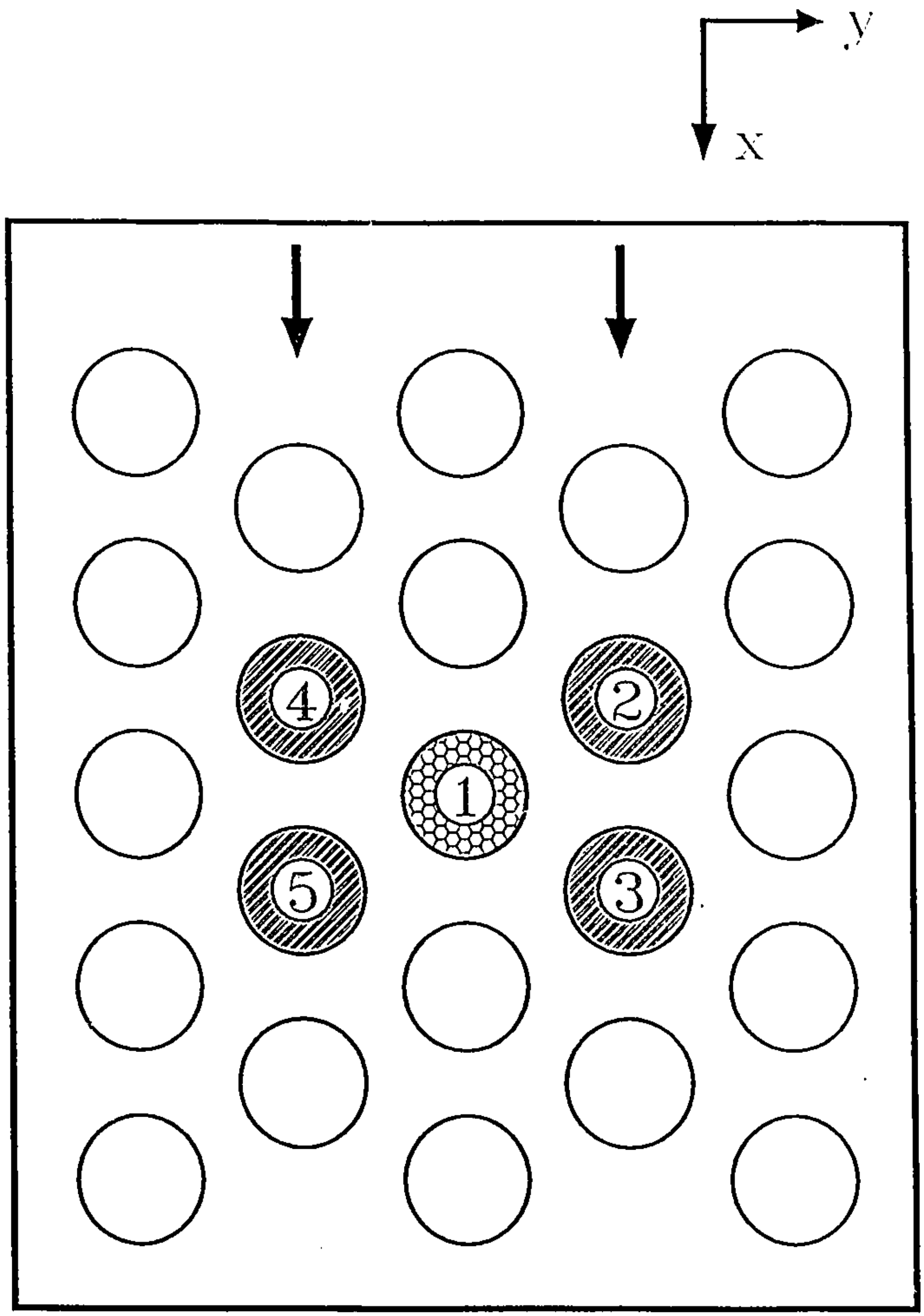

Figure 4.1 Parallel Triangular Array. Five Tubes Numbered 1 to 5 Indicate the Unit Cell for Tube #1.

existing theoretical model. For this purpose, the single flexible tube solution is extended to determine the pressure fluctuation in the downstream region of the vibrating tube. Then the forces acting on the upstream, center, and downstream tubes are determined by integrating the pressure along the attachment regions of the respective tubes.

4.1.1 Fluid Forces Acting in the Unit Cell

Consider only the tubes #1,2,3,4 and 5. The total force acting on the center tube is assumed to be the superposition of the fluid forces due to the vibration of the individual tubes (either one of the tubes #1,2,3,4 or 5) when the rest of the tubes are stationary. This is the same assumption used and verified by Tanaka and Takahara in their semi-empirical study. Their results showed excellent agreement with the experiments for a wide range of the mass-damping parameter.

The dimensionless equations of motion for the five tubes can be written as (from equations (3.25) and (3.26));

$$\frac{m}{\rho d^2}\left[-\left(\frac{\omega}{\omega_n}\right)^2+\frac{\delta}{\pi}\left(\frac{\omega}{\omega_n}\right)i+1\right]x_i^* = \bar{F}_{x_i} \quad , \quad i=1,5$$

$$\frac{m}{\rho d^2}\left[-\left(\frac{\omega}{\omega_n}\right)^2+\frac{\delta}{\pi}\left(\frac{\omega}{\omega_n}\right)i+1\right]y_i^* = \bar{F}_{y_i} \quad , \quad i=1,5 \tag{4.1}$$

where, the fluid forces, $\bar{F}_{x_i}$, and $\bar{F}_{y_i}$, are functions of the displacements of the five tubes. Similar to Tanaka and Takahara's notation [12-14], the fluid-dynamic forces acting on tube# i can be written as;

$$\bar{F}_{x_i} = \sum_{j=1}^{5} (C_{xjx_i} \dot{x}_j + C_{xjy_i} \dot{y}_j) \quad , \quad i=1,5$$
$$\bar{F}_{y_i} = \sum_{j=1}^{5} (C_{yjx_i} \dot{x}_j + C_{yjy_i} \dot{y}_j) \quad , \quad i=1,5 \qquad (4.2)$$

where i, j=1,2,...,5 denote the five tubes. C_{yjx_i}, etc. are fluid dynamic force coefficients. The first, second and third suffixes refer to direction of the force on cylinder i, the position of the vibrating cylinder generating the force (cylinder j), and the direction of motion of cylinder i being considered respectively. For example, C_{x3y_1} refers to the X-direction force on tube #1 caused by tube #3 vibrating in the Y-direction. In this case the upstream tube (tube #3) is the only tube that vibrates, the rest are stationary.

Some experimental studies [37, 38] show that the unstable mode of vibration is usually the mode where all the tubes move in the transverse direction. Tanaka & Takahara's [12] and Price & Païdoussis' [12] semi-empirical theories also yielded the least stable mode shapes with all the tubes moving in the transverse direction. Chen's semi-empirical [7] theory showed that streamwise motion might be observed at high values of the mass-damping parameter, but restricting the motion in the streamwise direction produces the instability threshold very close to that corresponding to an unrestricted mode. Therefore, for the sake of simplicity, the rest of the analysis will be carried by considering only the transverse vibrations. However, it should be kept in mind that the methodology is general, hence it is straightforward to include the streamwise vibrations.

In the case of no streamwise vibrations, the displacements of the fl... ..ole tubes in the unit cell are given as;

$$\left.\begin{aligned} x_i^* &= 0 \\ y_i^* &= Y_i^* e^{i\psi_i t} \end{aligned}\right\} \quad i=1,5 \tag{4.3}$$

Therefore, the force equations given in equation (4.2) reduce to;

$$\overline{F}_{y_i} = \sum_{j=1}^{5} (C_{yjy_i} y_j^*) \tag{4.4}$$

Inspecting equations (3.25(b)), (3.26) and (4.1), it can be seen that the force coefficients, C_{yjy} are the same as $\overline{F}$ given by (3.26). For example, if tube #1 vibrates in the transverse direction (y direction), the resultant transverse force, $\overline{F}$, acting on tube #2 becomes equal to C_{y1y_2}.

The force coefficient, C_{yjy}, is determined as a function of the array geometry, reduced velocity, and frequency ratio as mentioned in Chapter 3. The form of the unsteady fluid force is obtained in equation (3.26). From this equation the force coefficients can be written as :

$$C_{yjy} = C0_{yjy} U_r^2 + C1_{yjy} U_r \left(\frac{\omega}{\omega_n}\right) + C2_{yjy} \left(\frac{\omega}{\omega_n}\right)^2 \tag{4.5}$$

where, C0, C1 and C2 correspond to $\overline{F}_o$, $\overline{F}_1$ and $\overline{F}_2$ in equation (3.26), respectively.

4.1.2 Fluid Forces Due to the Center Tube

In the unit cell of figure 4.1, if tubes #2 to #5 are rigid and tube #1 is displaced y_1^*, the forces acting on the tubes are determined from the single flexible tube analysis as presented in chapter 3. Figure 4.2(a) shows these forces which are;

$$\begin{aligned}
\bar{F}_{y_1} &= y_1^* C_{ycy_1} \\
\bar{F}_{y_2} &= -y_1^* C_{yuy_2} \\
\bar{F}_{y_3} &= -y_1^* C_{ydy_3} \\
\bar{F}_{y_4} &= -y_1^* C_{yuy_4} \\
\bar{F}_{y_5} &= -y_1^* C_{ydy_5}
\end{aligned} \tag{4.6}$$

Note that the middle subscripts, c, u and d refer to Center, Upstream and Downstream, respectively. For computational purposes, equation (4.6) is written in compact form in equation (4.7). Thus, the force array for the unit cell, when only the center tube (tube #1) is vibrating, is obtained as follows;

$$\left\{ \begin{array}{c} \bar{F}_{y_1} \\ \bar{F}_{y_2} \\ \bar{F}_{y_3} \\ \bar{F}_{y_4} \\ \bar{F}_{y_5} \end{array} \right\} = \left\{ \begin{array}{c} C_{ycy} \\ -C_{yuy} \\ -C_{ydy} \\ -C_{yuy} \\ -C_{ydy} \end{array} \right\} y_1^* \tag{4.7}$$

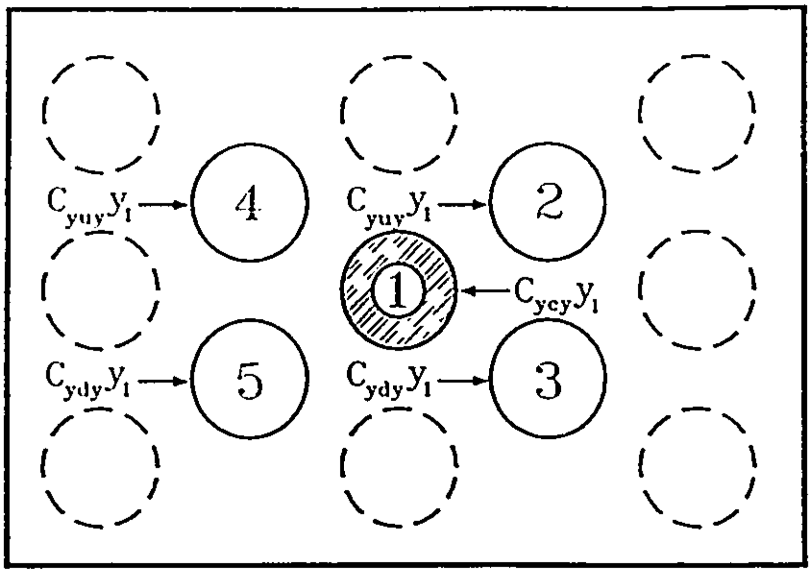

(a) Fluid Forces due to Tube #1

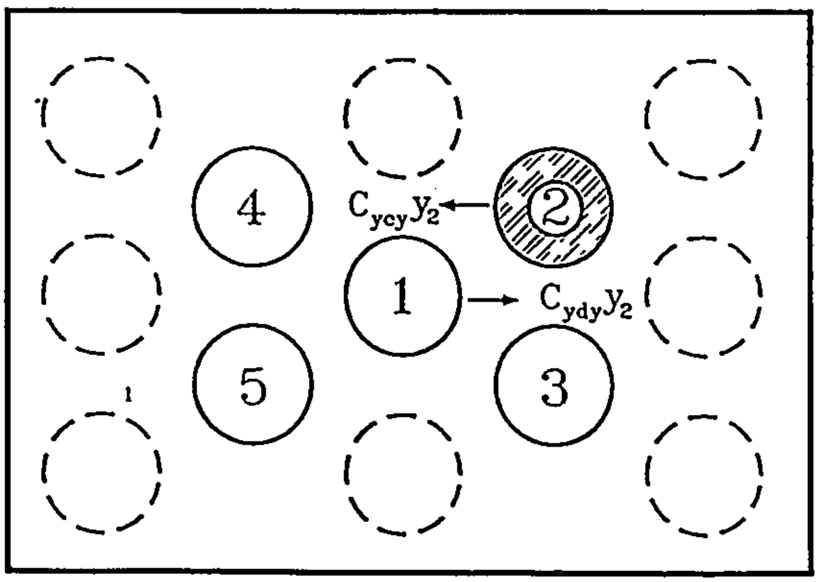

(b) Fluid Forces due to Tube #2

Figure 4.2 Forces Acting on the Surrounding Tubes due to the Vibration of (a) Tube #1, and (b) Tube #2 (solid lined circles show the flexible tubes) or,

$$\{F\}_1^c = \{C\}_1^c \; y_1^*$$ (4.8)

Here, $\{F\}_1^c$ and $\{C\}^c$ will be called the elemental force array, and the force coefficient array, respectively. The superscript c stands for "cell" to indicate that an array or a matrix is obtained for the unit cell. The subscript 1 indicates that the center tube in the unit cell is tube #1. The reason for writing the equations in this form is for computational purposes only. As can be seen in the following sections, it is easier to analyze a large number of vibrating tubes in this fashion. It should be noted that if any of the tubes in the unit cell are rigid, $\{C\}^c$ has to be modified accordingly. For example, if tube #2 and tube #4 are rigid, then the 2nd and 4th terms in $\{C\}^c$ must be set to zero.

4.1.3 Fluid Forces Due to all the Tubes in a Unit Cell

The principal of superposition is assumed to apply in multiple tube vibrations. If only the center tube (tube #1) is vibrating, the forces acting on the tubes in the unit cell are shown in figure 4.2(a). Similarly, if only an upstream tube (tube #2) is vibrating, the forces acting on the immediate neighboring tubes in the same unit cell are shown in figure 4.2(b). Forces due to the vibrations of other tubes in the unit cell can be obtained in the same way and are superimposed to determine the total forces acting on all the tubes in the unit cell. As a result, the forces acting on the tubes can be written as;

$$\bar{F}_{y_1} = (C_{ycy}\, y_1^* - C_{yuy}\, y_2^* - C_{ydy}\, y_3^* - C_{yuy}\, y_4^* - C_{ydy}\, y_5^*)$$

$$\bar{F}_{y_2} = (C_{ycy}\, y_2^* - C_{yuy}\, y_1^*)$$

$$\bar{F}_{y_3} = (C_{ycy}\, y_3^* - C_{ydy}\, y_1^*) \tag{4.9}$$

$$\bar{F}_{y_4} = (C_{ycy}\, y_4^* - C_{yuy}\, y_1^*)$$

$$\bar{F}_{y_5} = (C_{ycy}\, y_5^* - C_{ydy}\, y_1^*)$$

Written in matrix form, the force array for the unit cell can be obtained as follows;

$$\begin{Bmatrix} \bar{F}_{y_1} \\ \bar{F}_{y_2} \\ \bar{F}_{y_3} \\ \bar{F}_{y_4} \\ \bar{F}_{y_5} \end{Bmatrix} = \begin{bmatrix} C_{ycy} & -C_{ydy} & -C_{yuy} & -C_{ydy} & -C_{yuy} \\ -C_{yuy} & C_{ycy} & 0 & 0 & 0 \\ -C_{ydy} & 0 & C_{ycy} & 0 & 0 \\ -C_{yuy} & 0 & 0 & C_{ycy} & 0 \\ -C_{ydy} & 0 & 0 & 0 & C_{ycy} \end{bmatrix} * \begin{Bmatrix} y_1^* \\ y_2^* \\ y_3^* \\ y_4^* \\ y_5^* \end{Bmatrix} \tag{4.10}$$

or, $\{F\} = [C]\ \{y\}$ (4.11)

It must be kept in mind that the terms of the C-matrix, [C], are a function of the frequency ratio, ω/ω_n , and the reduced velocity, U_r, as shown in equation (4.5). Hence, the force coefficient matrix can be obtained as;

$$[C] = [C0]U_r^2 + [C1](\frac{\omega}{\omega_n})U_r + [C2](\frac{\omega}{\omega_n})^2 \tag{4.12}$$

For simplicity, only [C] will be used in the formulation for the rest of the analysis.

4.1.4 Solution for the Fully Flexible Array

Consider the fully flexible array with n tubes (see figure 4.3). Note that only 25 tubes are numbered in the figure, but it is possible to include as many flexible tubes in the analysis as desired. The displacements of the tubes are given as;

$$y_i^* = Y_i^* e^{i\psi_i t} \qquad i = 1,n \tag{4.13}$$

The elemental force equations can be written from equation (4.8). The unit cells for tube #9, and #13 are shown in figure 4.3. The forces acting on the tubes in the unit cells for tube #9 and tube #13 are given below:

$$\begin{aligned} \{F\}_9^c &= \{C\}_9^c\, y_9^* \\ \{F\}_{13}^c &= \{C\}_{13}^c\, y_{13}^* \end{aligned} \tag{4.14}$$

Note that in the equations given above, the elementary force coefficient array, $\{C\}^c$, does not change. It is given by equation (4.7). On the other hand, the force array is unit cell dependent. For example, $\{F\}_9^c = \{F_{x_9}, F_{x_7}, F_{x_{12}}, F_{x_6}, F_{x_{11}}\}$. The sequence of numbering must be the same as for the unit cell shown in figure 4.1. That is, the center tube (tube #9) is the first one, the upstream right tube (tube #7) is the second one, the

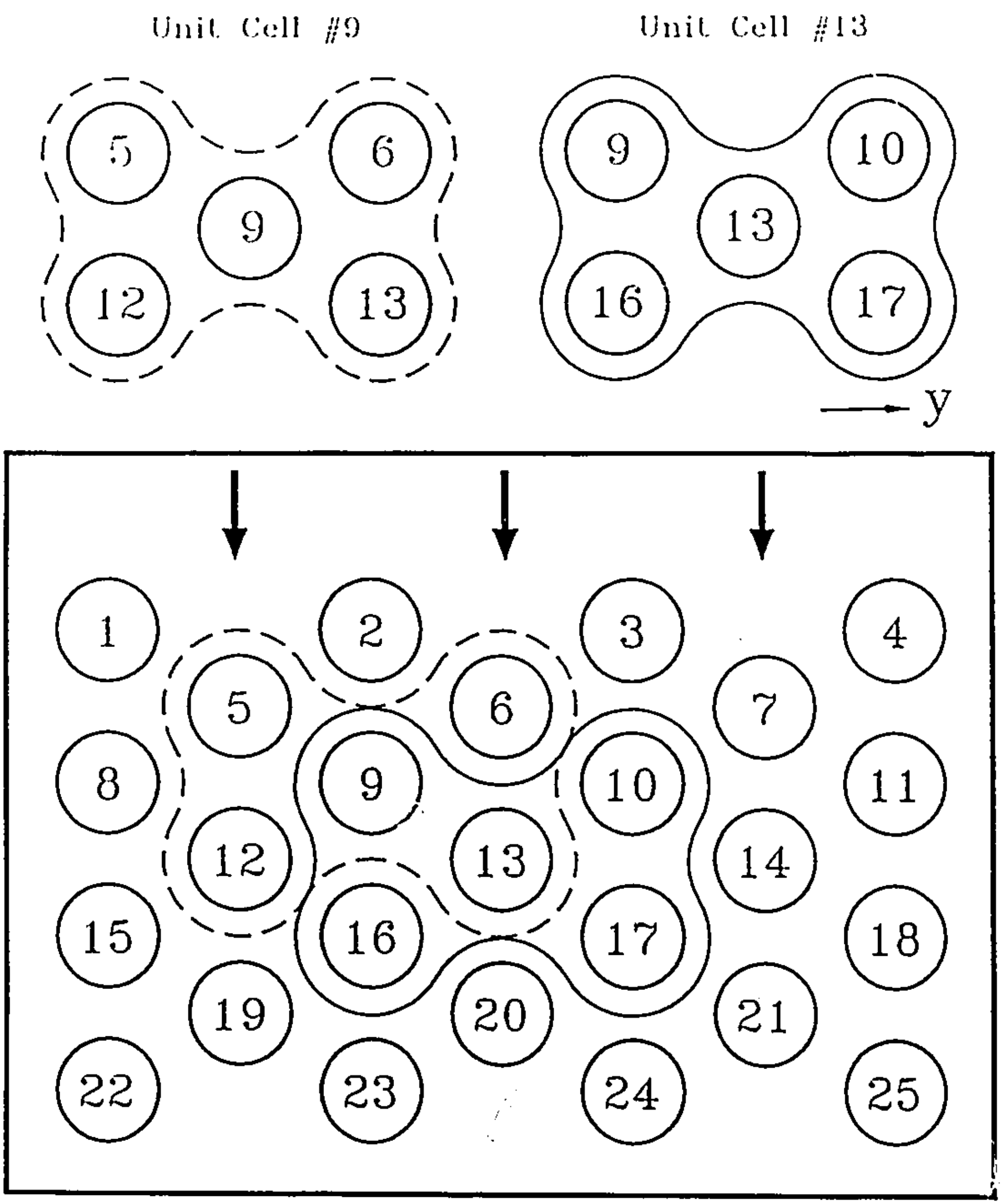

Figure 4.3 Fully Flexible Parallel Triangular Array

downstream right tube (tube #12) is the third one, the upstream left tube (tube #6) is the forth one and the downstream left tube (tube #11) is the fifth one.

For a fully flexible array with n tubes, the elemental matrix equations are written for each tube and these equations are assembled in a single global matrix form as in Finite Element Analysis. The resultant equations of fluid force will be in the form :

$$\{F\}^g = [C]^g\{y\}^g \qquad (4.15)$$

where,

$$[C]^g = \left[\{C\}_1^g, \{C\}_2^g, \;\ldots\;, \{C\}_n^g \right]$$

$$\{F\}^g = \{\overline{F}_{y_1}, \overline{F}_{y_2}, \;\ldots\;, \overline{F}_{y_n}\}$$

$$\{y\}^g = \{y_1^*, y_2^*, \;\ldots\;, y_n^*\}$$

Here, $[C]^g$ and $\{y\}^g$ refer to the global force coefficient matrix and global displacement vector, respectively. Note that due to the phase difference between the force coefficients and the tube motion, the C-matrix, $[C]^g$, is composed of complex numbers. Care must be taken when assembling the global C-matrix. The global force coefficient arrays, $\{C\}_i^g$, are easily determined from the elemental force coefficient arrays, $\{C\}_i^e$, by sorting the non-zero terms, so that they correspond to the same tube displacements in the global matrix equation as they do in the elemental matrix equation. The following examples will show how to assemble the global C-matrix, $[C]^g$, from the elemental force coefficient arrays and how to treat the special boundary flexible tubes that are adjacent to rigid tubes.

4.2. FLUID FORCE COEFFICIENT MATRIX FOR 13-FLEXIBLE TUBE AND 5-FLEXIBLE TUBE MODELS

In this section, the general approach for an n cylinder array developed in the previous section is applied to 13 flexible tube and 5 flexible tube arrays. The 13 flexible tube analysis will illustrate how to assemble the global C-matrix, $[C]^g$, from the elementary C-arrays, $[C]^c$. It will then be shown that this 13 tube model can be reduced to the 5 flexible tube model developed in section 4.1.3. Figure 4.4 shows the array under investigation. The elemental force arrays for 13 flexible tubes can be written as;

$$\{F\}_i^c = \{C\}_i^c \, y_i \qquad , \qquad i=1,13 \tag{4.16}$$

The unit cells #4, 5, 7, 9 and 10 include flexible tubes only. All of these unit cells have the elemental force coefficient array, $\{C\}^c$, in the same form as equation (4.6). For example,

$$\{F\}_4^c = \{C\}_4^c \, y_4^*$$

or,

$$\begin{Bmatrix} \bar{F}_{y_4} \\ \bar{F}_{y_7} \\ \bar{F}_{y_2} \\ \bar{F}_{y_1} \\ \bar{F}_{y_6} \end{Bmatrix} = \begin{Bmatrix} C_{ycy} \\ -C_{yuy} \\ -C_{ydy} \\ -C_{yuy} \\ -C_{ydy} \end{Bmatrix} y_4^* \tag{4.17}$$

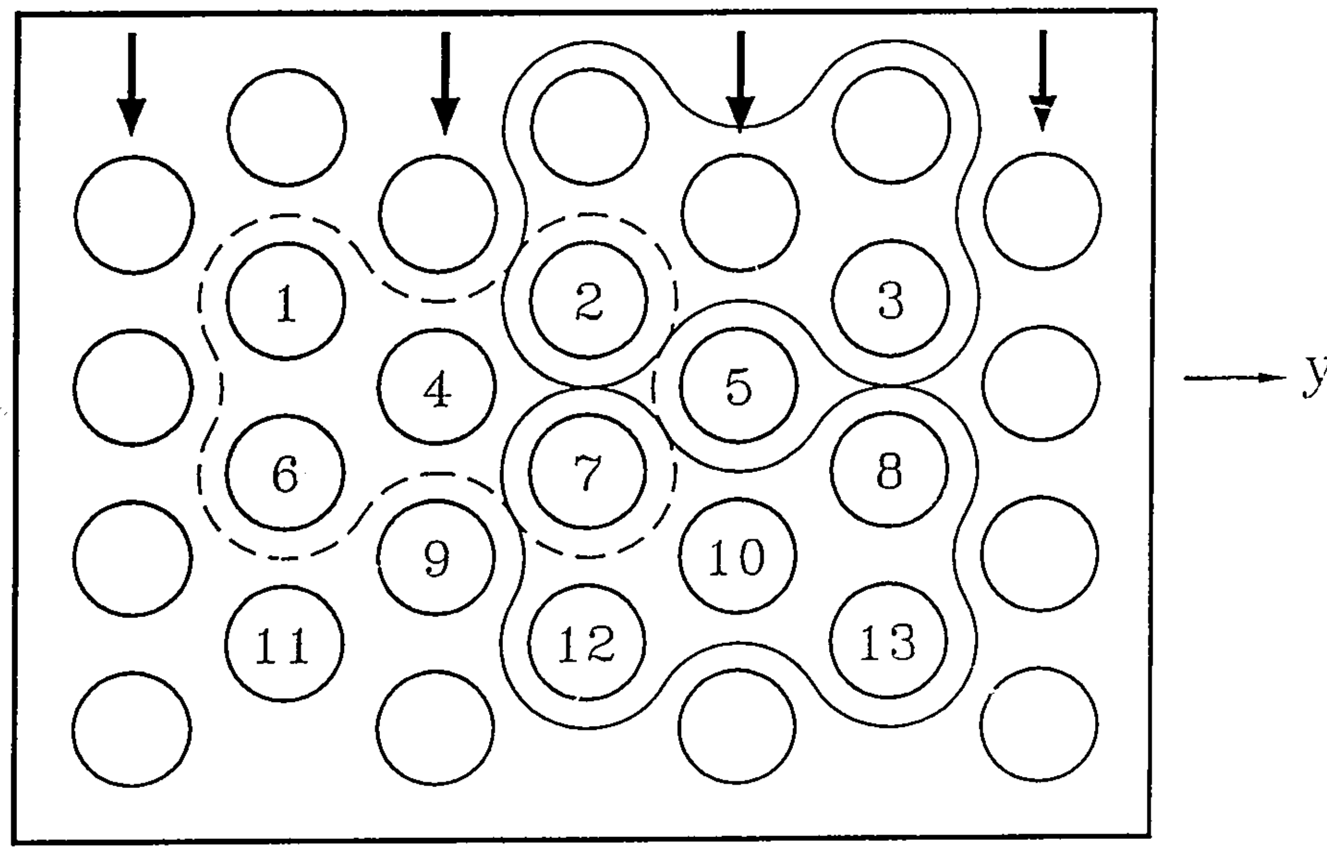

Figure 4.4 Parallel Triangular Array with 13 Flexible Tubes

Any other unit cell has at least one rigid tube. These are the boundary unit cells. Because of the rigid tubes existing in these boundary cells, $\{C\}^c$ has to be modified for these cells. For example; unit cell #3 has the two upstream tubes and the right downstream tube rigid (they correspond to the 2nd, 3rd and 4th terms in the elemental arrays), hence, the 2nd, 3rd and 4th terms in $\{C\}_3^c$ must be set to zero, i.e

$$\{F\}_3^c = \begin{Bmatrix} \bar{F}_{y_3} \\ 0 \\ 0 \\ 0 \\ \bar{F}_{y_1} \end{Bmatrix} = \begin{Bmatrix} C_{ycy} \\ 0 \\ 0 \\ 0 \\ -C_{ydy} \end{Bmatrix} y_3^* \tag{4.18}$$

Similarly, cell # 12 has two rigid downstream tubes. Therefore,

$$\{F\}_{12}^c = \begin{Bmatrix} \bar{F}_{y_{12}} \\ \bar{F}_{y_{10}} \\ 0 \\ \bar{F}_{y_9} \\ 0 \end{Bmatrix} = \begin{Bmatrix} C_{ycy} \\ -C_{yuy} \\ 0 \\ -C_{yuy} \\ 0 \end{Bmatrix} y_{12}^* \tag{4.19}$$

Then all these equations are written in the form;

$$\{F\}^s = [C]^s\{y\}^s \tag{4.20}$$

Since the global force vector, $\{F\}^s$, is in the form;

$$\{F\}^s = \{ F_1, F_2, \dots , F_{13}\}^T \tag{4.21}$$

the global force coefficient arrays, $\{C\}^{g}$ should be determined accordingly. For example, for the unit cell #3, $\{C\}^{g}$ can written as;

$$\{C\}_3^{g} = \{\ 0,\ 0,\ C_{ycy},\ 0, -C_{ydy},\ 0,\ 0,\ 0,\ 0,\ 0,\ 0,\ 0,\ 0\}^T \qquad (4.22)$$

Then, the global equations will be in the form:

$$\begin{Bmatrix} \overline{F}_{y_1} \\ \overline{F}_{y_2} \\ \vdots \\ \overline{F}_{y_{13}} \end{Bmatrix} = [C]^{g} \begin{Bmatrix} y_1^* \\ y_2^* \\ \vdots \\ y_{13}^* \end{Bmatrix} \qquad (4.23)$$

where,

$$[C]^{g} = \left[\ \{C\}_1^{g}, \{C\}_2^{g},\ \ldots\ ,\ \{C\}_{13}^{g} \right]$$

For the array under investigation, $[C]^{g}$ is;

$$[C]^{s}=\begin{bmatrix}
C_{ycy} & 0 & 0 & -C_{yuy} & 0 & 0 & 0 & 0 & 0 & 0 & 0 & 0 & 0 \\
0 & C_{ycy} & 0 & -C_{yuy} & -C_{yuy} & 0 & 0 & 0 & 0 & 0 & 0 & 0 & 0 \\
0 & 0 & C_{ycy} & 0 & -C_{yuy} & 0 & 0 & 0 & 0 & 0 & 0 & 0 & 0 \\
-C_{ydy} & -C_{ydy} & 0 & C_{ycy} & 0 & -C_{yuy} & -C_{yuy} & 0 & 0 & 0 & 0 & 0 & 0 \\
0 & -C_{ydy} & -C_{ydy} & 0 & C_{ycy} & 0 & -C_{yuy} & -C_{yuy} & 0 & 0 & 0 & 0 & 0 \\
0 & 0 & 0 & -C_{ydy} & 0 & C_{ycy} & 0 & 0 & -C_{yuy} & 0 & 0 & 0 & 0 \\
0 & 0 & 0 & -C_{ydy} & -C_{ydy} & 0 & C_{ycy} & 0 & -C_{yuy} & -C_{yuy} & 0 & 0 & 0 \\
0 & 0 & 0 & 0 & -C_{ydy} & 0 & 0 & C_{ycy} & 0 & -C_{yuy} & 0 & 0 & 0 \\
0 & 0 & 0 & 0 & 0 & -C_{ydy} & -C_{ydy} & 0 & C_{ycy} & 0 & -C_{yuy} & -C_{yuy} & 0 \\
0 & 0 & 0 & 0 & 0 & 0 & -C_{ydy} & -C_{ydy} & 0 & C_{ycy} & 0 & -C_{yuy} & -C_{yuy} \\
0 & 0 & 0 & 0 & 0 & 0 & 0 & 0 & -C_{ydy} & 0 & C_{ycy} & 0 & 0 \\
0 & 0 & 0 & 0 & 0 & 0 & 0 & 0 & -C_{ydy} & -C_{ydy} & 0 & C_{ycy} & 0 \\
0 & 0 & 0 & 0 & 0 & 0 & 0 & 0 & 0 & -C_{ydy} & 0 & 0 & C_{ycy}
\end{bmatrix} \qquad 4.24$$

The solution for 10 flexible tubes can be deduced from the 13 flexible tubes by eliminating the 11th, 12th and 13th rows and columns. The remaining 10x10 matrix is the global force coefficient matrix for the 10 flexible tubes numbered from 1 to 10 in figure 4.4. Similarly, a five flexible tube solution can be obtained by considering a unit cell made up of flexible tubes only. For example, unit cell #4, that includes tubes #1, 2, 4, 6, and 7 can be considered for the five flexible tube solution. That is, any other row and column, other than the 1st, 2nd, 4th, 6th and 7th row and column is eliminated to obtain;

$$\begin{Bmatrix} \bar{F}_{y_1} \\ \bar{F}_{y_2} \\ \bar{F}_{y_4} \\ \bar{F}_{y_6} \\ \bar{F}_{y_7} \end{Bmatrix} = \begin{bmatrix} C_{ycy} & 0 & -C_{yuy} & 0 & 0 \\ 0 & C_{ycy} & -C_{yuy} & 0 & 0 \\ -C_{ydy} & -C_{ydy} & C_{ycy} & -C_{yuy} & -C_{yuy} \\ 0 & 0 & -C_{ydy} & C_{ycy} & 0 \\ 0 & 0 & -C_{ydy} & 0 & C_{ycy} \end{bmatrix} \begin{Bmatrix} y_1^* \\ y_2^* \\ y_4^* \\ y_6^* \\ y_7^* \end{Bmatrix} \qquad (4.25)$$

This solution appears to be different than the one obtained before (See section 4.1.3). This is because of the different sequence of numbering of the tubes. If the numbering follows the same sequence as the previous one (see figure 4.1), both solutions are the same. That is,

$$\begin{Bmatrix} \bar{F}_{y_4} \\ \bar{F}_{y_2} \\ \bar{F}_{y_7} \\ \bar{F}_{y_1} \\ \bar{F}_{y_6} \end{Bmatrix} = \begin{bmatrix} C_{ycy} & -C_{ydy} & -C_{yuy} & -C_{ydy} & -C_{yuy} \\ -C_{yuy} & C_{ycy} & 0 & 0 & 0 \\ -C_{ydy} & 0 & C_{ycy} & 0 & 0 \\ -C_{yuy} & 0 & 0 & C_{ycy} & 0 \\ -C_{ydy} & 0 & 0 & 0 & C_{ycy} \end{bmatrix} \begin{Bmatrix} y_4^* \\ y_2^* \\ y_7^* \\ y_1^* \\ y_6^* \end{Bmatrix} \qquad (4.26)$$

4.3 DETERMINATION OF THE VIBRATION MODE (5-TUBE MODEL)

So far, a general method is presented to determine the fluid force matrix for a given array geometry and the dimensionless velocity, U_f. What has not been taken into account is the vibration pattern. Price & Païdoussis investigated the effect of the modal vibration pattern on the stability threshold [12,13]. They assumed that, for any row, the motions of adjacent tubes are of equal magnitude and either in in-phase or out-of-phase. Similarly, they assumed that the motion of a tube and it's counterparts two rows upstream and downstream is either in-phase or out-of-phase. As a result of these assumptions, they showed that the solution for fully flexible tube arrays can be reduced to a two-cylinder kernel. Since the motion of the tubes are constrained according to the above mentioned vibration modes, this analysis is called the *Constrained Mode Analysis*. They tried 256 possible vibration modes and determined the least unstable modes for various arrays [12]. In parallel triangular arrays, one mode was found to be the least stable mode for the whole range. The same mode was also the least stable mode for the rotated square arrays with $m\delta/\rho d^2 > 25$. Price et. al.'s subsequent investigation [13] on the vibration pattern by varying the phase relationships of the neighboring tubes verified their previous findings.

In the present analysis, all possible modeshapes will not be searched as this was already done by Price et. al. Instead, a simplified approach, by using Price et. al.'s findings, will be adapted to determine a modeshape that would predict critical velocities close to the absolute minimum critical velocity. The approach used here is not as comprehensive as Price et. al.'s approach, but should yield acceptable results.

The 5-tube model (figure 4.1) for the parallel triangular arrays is simplified by using the following assumptions :

(1) The motion of the adjacent tubes in a row are equal in magnitude and are either in-phase or out-of-phase with each other. This is the same assumption used by Price et al. . If the tubes are out-of phase, the forces acting on the center tube (tube #1) due to the upstream tubes (tubes #2 and #4) would cancel each other. A similar result would be found if the downstream tubes are considered. Therefore, the center tube would be unaffected by the neighboring tube motion if the adjacent tubes in a row are out-of-phase. Since the effect of neighboring tube motion is desired for a successful modelling of the stiffness-controlled dynamic instability, adjacent tubes in a row should be in-phase with each other. This is, in fact, the case for the least unstable mode reported by Price & Païdoussis [12]. Therefore $y_2^{\bullet} = y_4^{\bullet}$, and $y_3^{\bullet} = y_5^{\bullet}$ and the force equations (4.12) for the unit cell given in figure 4.1 reduces to :

$$\begin{Bmatrix} \bar{F}_{y_1} \\ \bar{F}_{y_2} \\ \bar{F}_{y_3} \end{Bmatrix} = \begin{bmatrix} C_{ycy} & -2C_{ydy} & -2C_{yuy} \\ -C_{yuy} & C_{ycy} & 0 \\ -C_{ydy} & 0 & C_{ycy} \end{bmatrix} \bullet \begin{Bmatrix} y_1^{\bullet} \\ y_2^{\bullet} \\ y_3^{\bullet} \end{Bmatrix} \qquad (4.27)$$

(2) There is 180° phase difference between the tubes in a row and the tubes two rows upstream and downstream. This assumption ensures the repeatability of the vibration pattern in the streamwise direction. That is, the tubes in a row will vibrate the same way as the tubes 4 rows upstream and 4 rows downstream do. Price and Païdoussis [12] assumed that the above mentioned

phase can be either 0° or 180°. Their analysis showed that 180° is the one that gives lower critical velocity. Therefore, $\dot{y}_3 = -\dot{y}_2$ and equation (4.27) reduces to :

$$\begin{Bmatrix} \bar{F}_{y_1} \\ \bar{F}_{y_2} \end{Bmatrix} = \begin{bmatrix} C_{ycy} & -2(C_{ydy} - C_{yuy}) \\ C_{ydy} & C_{ycy} \end{bmatrix} \cdot \begin{Bmatrix} \dot{y}_1 \\ \dot{y}_2 \end{Bmatrix} \tag{4.28}$$

Assuming that $\dot{y}_2 = \dot{y}_1 \angle\, \psi_2$, the constrained equation of motion for the five flexible tube array reduces to a single equation (Here, $\angle\, \psi_2$, shows that y_2 is leading y_1 by ψ_2) :

$$\bar{F}_{y_1} = [C_{ycy} - 2(C_{ydy} - C_{yuy})\angle\, \psi_2]\; \dot{y}_1 \tag{4.29}$$

The value of ψ_2 is optimized to obtain the maximum imaginary part of equation (4.29). When substituted in equation (4.1), this optimization ensures the largest mass-damping parameter, $m\delta/\rho d^2$, for the given dimensionless velocity, U_r. Therefore, for a given mass-damping parameter, U_r is minimized, and the least unstable mode is found as, $y_2 = y_4 = y_1 \angle\, \psi_2$, $y_3 = y_5 = y_1 \angle\, 180^\circ - \psi_2$. As will be discussed in chapter 6, at high mass-damping parameters, the force coefficients, C_{ycy}, C_{yuy} and C_{ydy} are essentially real numbers with positive values and $C_{ydy} > C_{yuy}$ in general. Hence, equation 4.29 attains its maximum positive imaginary component at about $\psi_2 = -90^\circ$. As a result of this, the least stable mode becomes $\dot{y}_2 = \dot{y}_4 = \dot{y}_1 \angle -90^\circ$, $\dot{y}_3 = \dot{y}_5 = \dot{y}_1 \angle\, 90^\circ$. This modeshape is similar to Price and Païdoussis' least stable mode, where $y_2 = y_4 = y_1^* \angle\, 90^\circ$ $y_3 = y_5 = y_1^* \angle\, {-90}^\circ$.

4.3.1 In-Line Square Arrays

Although the modelling and determination of the unsteady forces acting on the tubes in in-line square arrays is the same as parallel triangular arrays (see figure 3.1(a)), the elemental force arrays are different. The reason for this is the difference in the relative positions of the neighboring tubes with respect to the streamtubes. Following the same procedure described in section 4.1.3, the global force coefficient array for the 5-flexible tube model in the in-line square arrays (figure 4.5) is found to be:

$$\begin{Bmatrix} \bar{F}_{y_1} \\ \bar{F}_{y_2} \\ \bar{F}_{y_3} \\ \bar{F}_{y_4} \\ \bar{F}_{y_5} \end{Bmatrix} = \begin{bmatrix} C_{ycy} & -C_{ycy}/2 & C_{yuy} & -C_{ycy}/2 & C_{ydy} \\ -C_{ycy}/2 & C_{ycy} & 0 & 0 & 0 \\ C_{ydy} & 0 & C_{ycy} & 0 & 0 \\ -C_{yuy}/2 & 0 & 0 & C_{ycy} & 0 \\ C_{yuy} & 0 & 0 & 0 & C_{ycy} \end{bmatrix} \begin{Bmatrix} y_1^* \\ y_2^* \\ y_3^* \\ y_4^* \\ y_5^* \end{Bmatrix} \quad (4.30)$$

The off-diagonal C_{ycy} terms are half that of the diagonal ones, because the tubes corresponding to these coefficients (tube #2 and tube #4) experience the pressure perturbations of one streamtube, whereas the center tube (tube #1) experiences the perturbations of two streamtubes. A similar approach presented in the previous section can be used to determine the least stable modeshape.

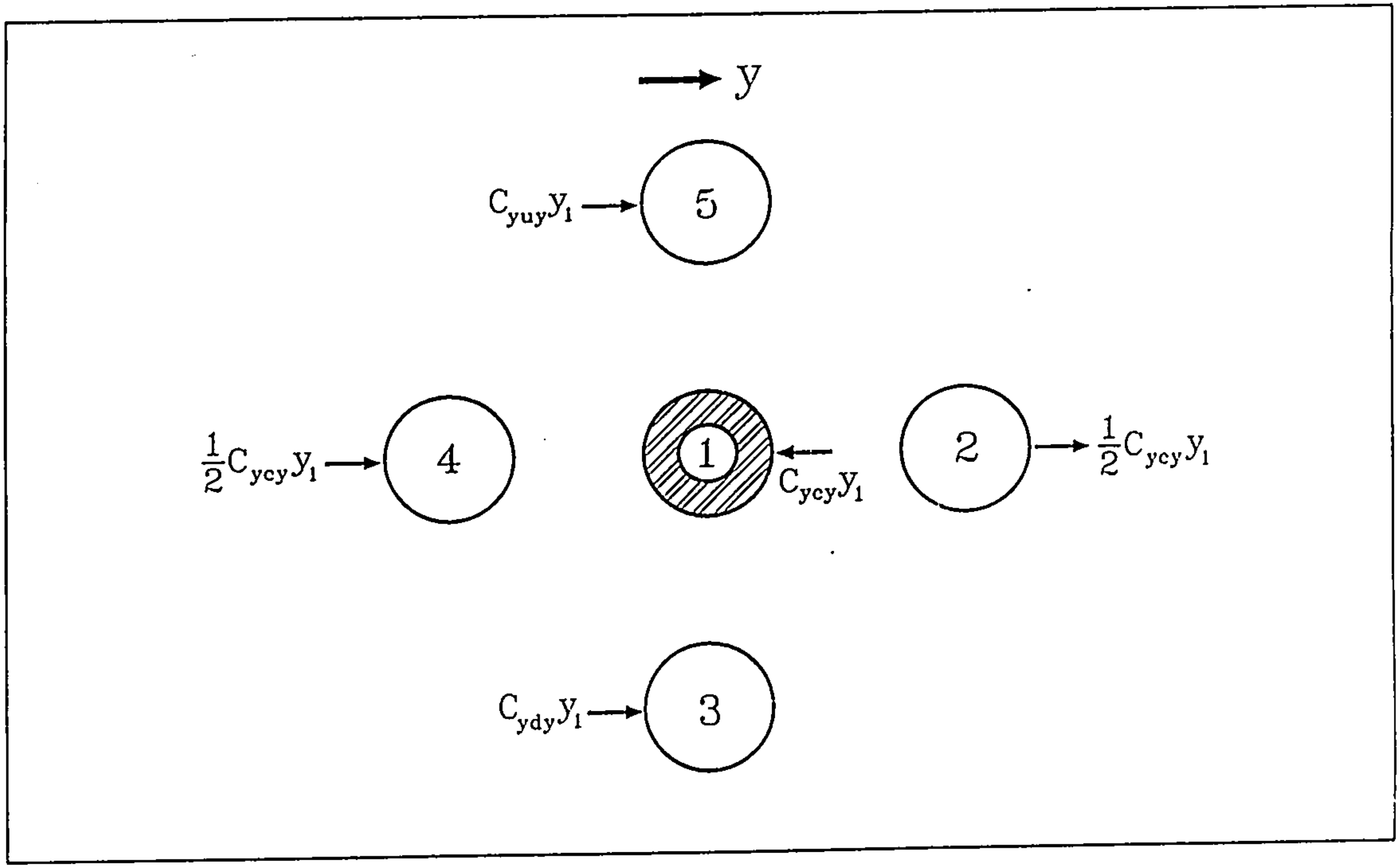

Figure 4.5 Unsteady Forces in a Unit cell in In-Line Arrays

Again, y_2^* cannot be out of phase with y_4^*, if it is desired to couple their motion with the center tube (tube #1). Hence it is assumed that they are in phase, i.e., $y_2^* = y_4^*$. Similar to the modeshape predicted in the previous section, if the downstream tube is out of phase with the upstream tube, $y_5^* = -y_3^*$. Then equation (4.30) reduces to :

$$\begin{Bmatrix} \bar{F}_{y_1} \\ \bar{F}_{y_2} \\ \bar{F}_{y_3} \end{Bmatrix} = \begin{bmatrix} C_{ycy} & -C_{ycy} & -(C_{yuy}-C_{ydy}) \\ -C_{ycy}/2 & C_{ycy} & 0 \\ -C_{ydy} & 0 & C_{ycy} \end{bmatrix} * \begin{Bmatrix} y_1^* \\ y_2^* \\ y_3^* \end{Bmatrix} \qquad (4.31)$$

For tube #1 be coupled with tube #2, they cannot be in phase. Hence, assuming out-of-phase motion, $y_2^* = -y_1^*$, equation (4.31) can be reduced to a two degree of freedom system as mentioned in the previous section. Again, by using the same argument for the determination of the maximum mass-damping parameter, the following characteristic equation corresponding to the modeshape $y_2^* = y_4^* = y_1^*$, $y_5^* = -y_3^* = -y_1^* \angle \psi_3$ is found as :

$$\bar{F}_{y_1} = [2C_{ycy} - (C_{ydy} - C_{yuy}) \angle \psi_3]\, y_1^* \qquad (4.32)$$

As described in the previous section, the value of ψ_3 is optimized and $\bar{F}_{y_1}$ is substituted into equation 4.1 to determine the critical mass-damping ratio, $m\delta/\rho d$, for a given dimensionless velocity, U_r.

4.4 RESULTS AND DISCUSSION

The single flexible tube model is extended to a multiple flexible tube model in order to investigate the effect of neighboring tube motion. The basic assumption in the extended model is that the total force acting on a tube is the superposition of the fluid forces due to the vibration of the individual tubes when the rest of the tubes are stationary. It is also assumed that only the immediate neighboring tubes directly affect the vibration of a tube. The rest of the tubes in the array indirectly affect the vibration of the tube through a cascade effect. Therefore, the fluid force acting on a tube is a function of the motions of all the tubes in the array. The resultant coupled equations of motion is reduced to a single equation by using a constrained mode analysis. By solving this equation, the mass-damping parameter corresponding to a given dimensionless velocity is found.

In order to determine the fluid forces acting on the downstream tubes, the single flexible model is extended so that the velocity and pressure fluctuations are obtained in the downstream flow region. Although the downstream streamtube length is not known, intuitively one would expect vorticity generated by tube motion to be convected many tube rows downstream. The experimental study presented in chapter 5 supports this. However, such convected disturbances are not related in any obvious way to the inertial streamtube length associated with the phase lag. In the absence of information to the contrary, the downstream streamtube length is assumed to be equal to the upstream streamtube length. Additionally, the same type of decay function is used in the downstream area as the one used in the upstream area.

The phase function in the downstream area is assumed to be the same as the upstream phase function, since there is no information on which to establish a better approximation.

The multiple tube analysis, presented in sections 4.1 through 4.3, is general for all tube arrays except in-line square arrays. For in-line square arrays, the methodology is the same except the elemental force coefficient array, $\{C\}^c$, is different as given in section 4.3.2.

4.4.1 Dynamic Instability for 5-Flexible Tubes

The results for the 5-tube model of the parallel triangular array with $P_r = 1.375$ are shown in figure 4.6. The system parameters used when obtaining figure 4.6 are the same as the ones used to obtain figure 3.14. The solution for the single flexible tube model is shown with the dashed line. Solid lines show the solution for the multiple tube model. As it is seen in the figure, the multiple flexible tube model always predicts lower critical dimensionless velocities than the single flexible tube model. The difference between these two models is

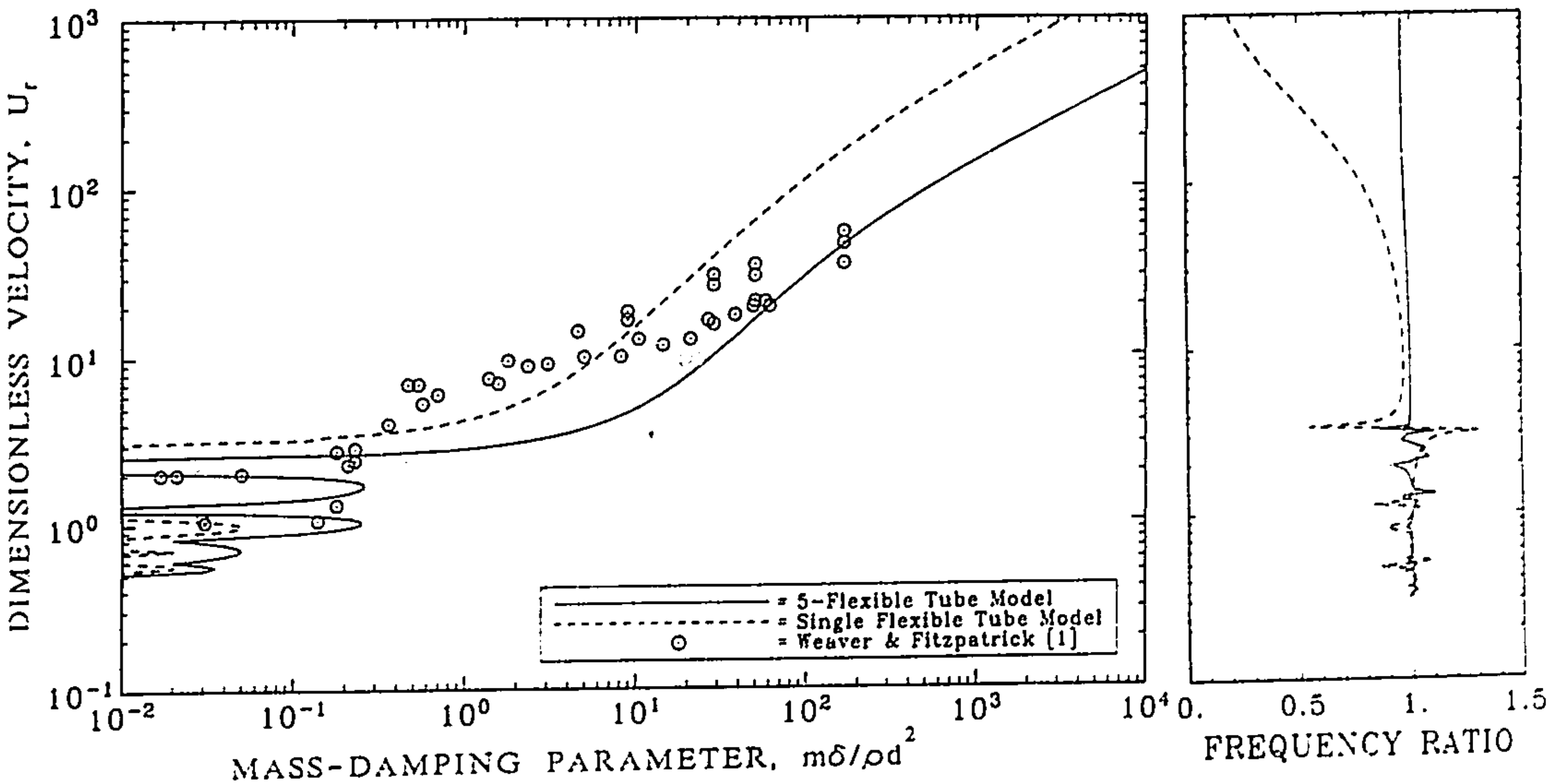

Figure 4.6 Dynamic Instability for 5 Flexible Tubes in the Parallel Triangular Array with P_r=1.375

largest at high values of the mass-damping parameters, implying that the neighboring tube motion is very important in this range. At low values of the mass damping parameters, the multiple flexible tube solution is closer to the single flexible tube solution. Hence, the coupling of the neighboring tubes is less important in this range.

With the extension to multiple tube analysis, the agreement between the experiments and the theoretical predictions are improved at high values of the mass-damping parameter. As can be seen in figure 4.6, the slope of the stability curve becomes 0.5 at high values of the mass-damping parameters. The frequency ratio, ω/ω_n is found to be approximately unity for the whole range. This behavior is essentially the same as that described by Chen [6-8] and Price & Païdoussis [10-13] as *stiffness-controlled dynamic instability*. As they reported, the effect of the neighboring tubes plays a major role at high values of the mass-damping parameter. The present model exhibits the same behavior, thus successfully modelling the *stiffness controlled instability*.

An interesting feature of the results shown in figure 4.6 is the limited number of instability regions. No instability regions are eliminated artificially as was done by Lever and Weaver [23-25], and Price & Païdoussis [9-13]. Incidentally, the number of instability regions obtained here is close to the maximum possible instability regions assumed by the above mentioned researchers. However, a close examination of the numerical solution shows that, other instability regions also exist, but they are out of the investigated range of the mass-damping parameter ($m\delta/\rho d^2 < 0.01$).

4.4.2 The Effect of the Downstream Pressure Decay

It is noted in figure 4.6 that the effect of coupling from neighboring tubes is reduced at smaller values of the mass-damping parameter but that it does not disappear. This may be due, in part, to the way in which the decay of disturbances has been modeled. Physically, this decay is caused by viscous effects which will manifest itself in terms of a decay in pressure perturbations. This has been modeled artificially and simply by introducing an area decay function into the analysis. For the single flexible tube model, this approach was satisfactory since only the pressure on the tube being analyzed was needed. In the multiple flexible tube model, the pressure on a downstream tube produced by motions of an upstream tube is required. Since, the pressure is obtained by integrating area and velocity disturbances along a streamline, the pressure disturbances will persist downstream even though the local area disturbance has disappeared. Thus the pressure perturbations on downstream tubes are exaggerated over those which would have been obtained by using a pressure decay function rather than a perturbation area decay function. Clearly, the former would have been more realistic but much more difficult to model.

In order to examine the effect of these exaggerated downstream pressures, they were artificially decayed by simply multiplying them with the area decay function (equation 3.15).

The results are shown in figure 4.7. It is seen that the

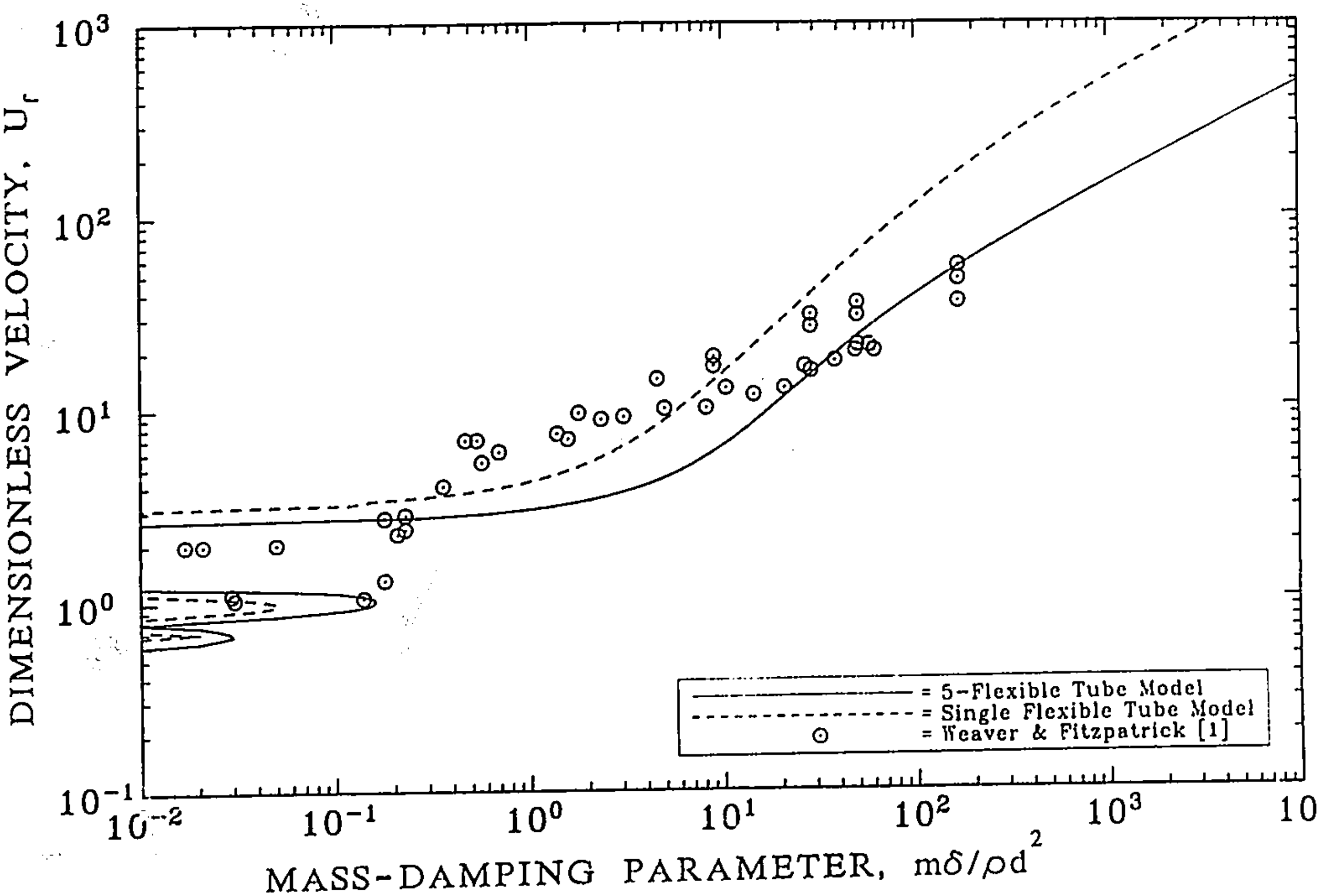

Figure 4.7 The Effect of the Downstream Pressure Decay

primary effect is at low values of the mass-damping parameter where the agreement between the single flexible tube and multiple flexible tube models has been improved. Most notable is the improved agreement in the multiple stability region for $m\delta/\rho d^2 < 0.2$.

4.4.2 Results For the In-Line Square Arrays

The modeshape discussed in section 4.3.1 was used to predict the dynamic instability for in-line square arrays as shown in figure 4.8. Again, perturbations are assumed to diminish within 1.5 tube rows upstream and downstream of the tube being studied.

Agreement with experiments is reasonably good over the entire mass-damping parameter range. The effect of neighboring tube motion reduces the stability threshold at higher values of the mass-damping parameter. The effect of neighboring tube motion is small at lower values of the mass-damping parameters as expected.

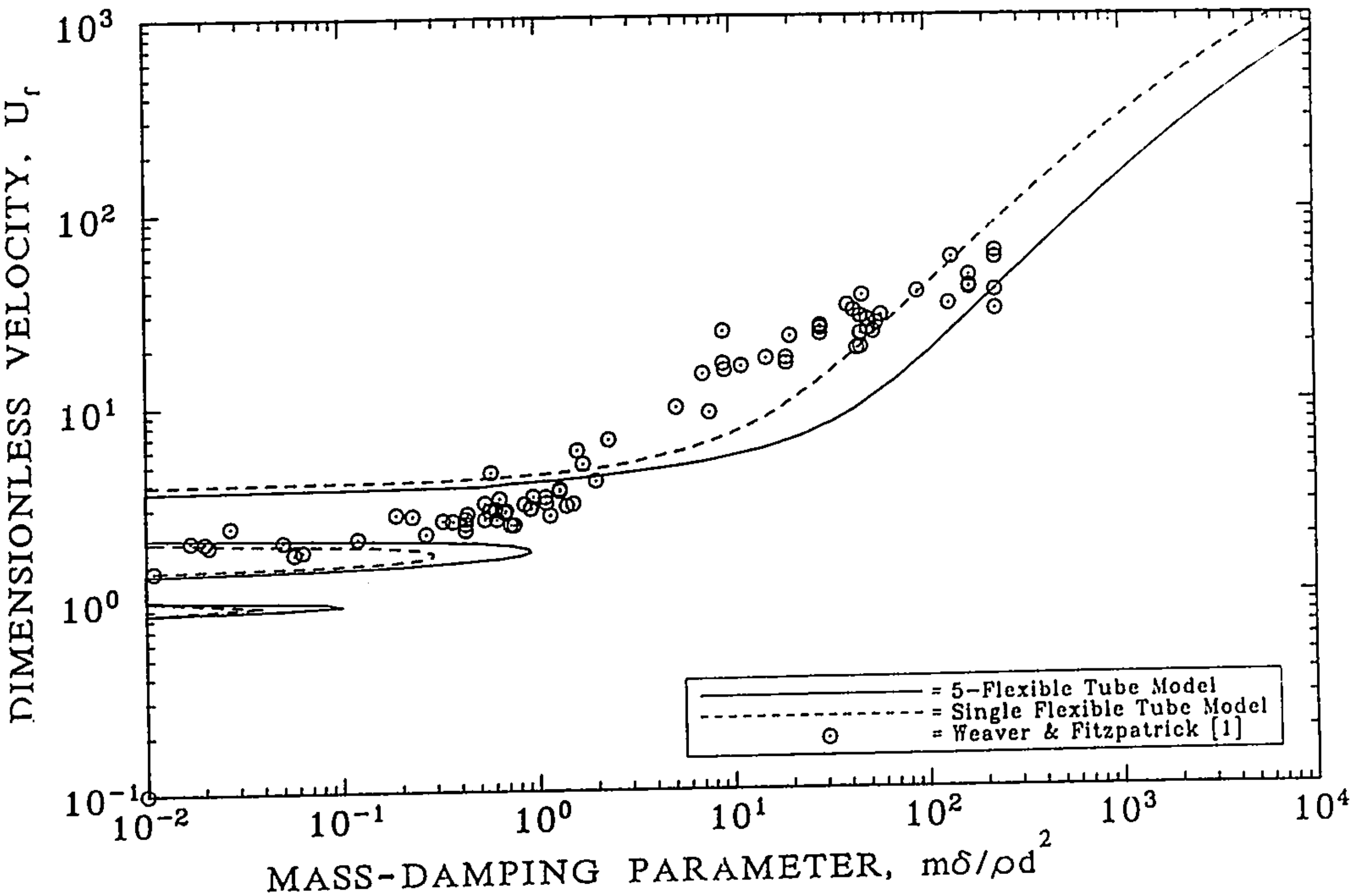

Figure 4.8 Dynamic Instability for 5 Flexible Tubes in the In-line Square Array with P_r=1.375

CHAPTER 5

AN EXPERIMENTAL STUDY ON THE PHASE FUNCTION AND THE DECAY FUNCTION

A weakness of the present theoretical model is the form of the proposed phase and decay functions. These proposed functions yield results which agree reasonably well with experiments, yet they are based entirely on intuition and their validity is open to question [10]. A parametric study of the present model shows that the critical velocity for the fluidelastic instability for a given array is significantly affected by the phase function. This function, as proposed by Lever and Weaver [24], is based on the surge phenomenon in liquid filled pipes. Although it is believed here that this rough analogy results in the correct qualitative trends, the quantitative phase values may be substantially in error. Therefore, a better understanding of the phase function is necessary. A careful examination of the phase function shows two unrealistic characteristics. Firstly, the phase function approaches infinity when the dimensionless velocity approaches zero. An infinite phase value represents infinite fluid inertia. Clearly, this cannot be correct. Secondly, the phase function is always equal to $1/U_r$ at $s = -s_1$. There is no reason to believe that this should be so.

As mentioned above, it is believed here that the phase function gives the correct general trends. Firstly, when the dimensionless velocity increases, the phase lag decreases. Since higher critical dimensionless velocities are obtained in less dense fluids, inertial forces are smaller and perturbations are felt in shorter time periods. Hence, the phase lag is expected to be smaller at high dimensionless velocities. Secondly, the phase function gives the phase lag as a linear function of position. The further the position of a point from the vibrating tube the longer it takes to feel the perturbation. This should be correct if the perturbations are assumed to be travelling with constant speed.

On the other hand, it is important to determine how the fluctuating velocity and pressure decay. How far from the vibrating tube can the fluid disturbances be felt?. Do the phase function and the decay function behave the same way in upstream and downstream regions?. The following section describes an experimental study which attempted to address these questions.

5.1 DESIGN OF THE TEST RIG

Because of the complexity of the phenomenon, a satisfactory theoretical solution for the phase function and the decay function couldn't be obtained. In order to obtain some insight into this behavior, it was decided to perform an experimental study. For this purpose, the wind tunnel designed by Grover [37] was used. This facility is shown schematically in figure 5.1. In the test section, the velocity distribution is uniform within 1% over the middle 80% of the cross sectional area (inside the wall boundary layers). The maximum operating speed is 19 m/sec when there is no tube array in the test section.

A test section was designed for the purposes of this study. All but one of the tubes in the array are rigid and fixed at one end. The remaining tube is rigid but connected to a shaker. This

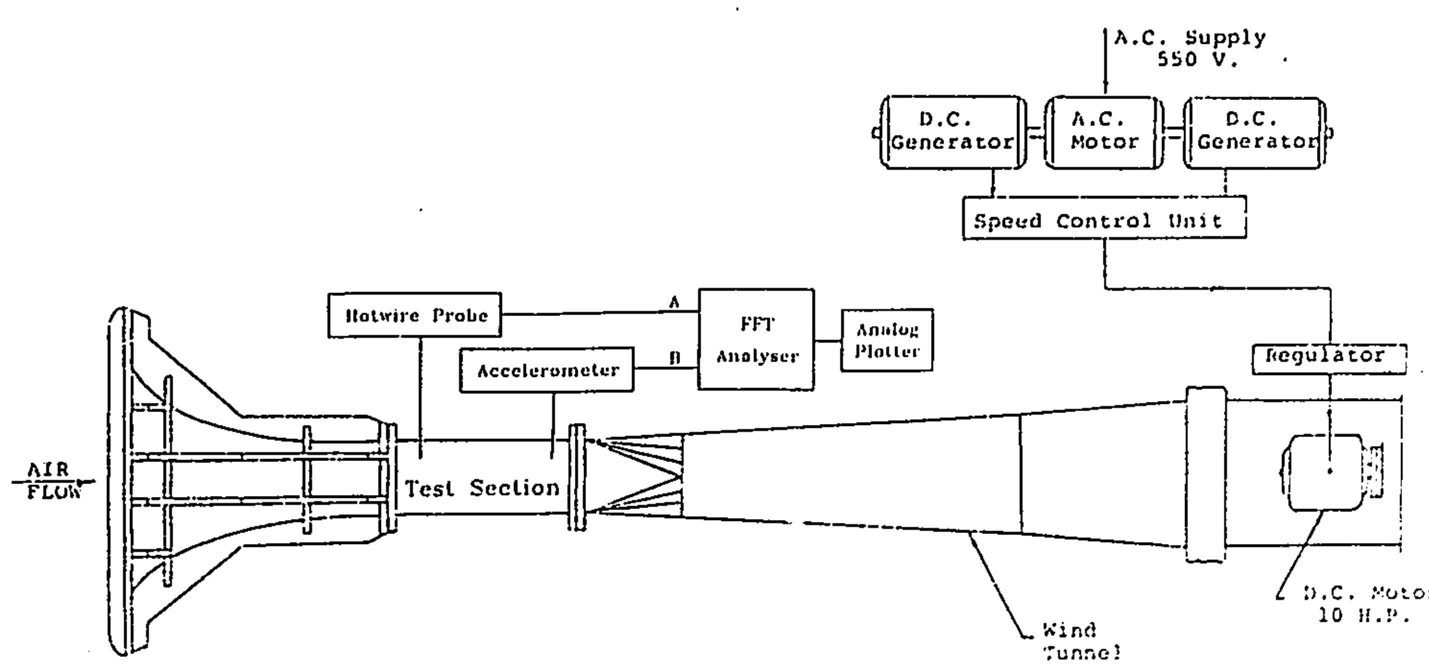

Figure 5.1 Schematic of Experimental Setup (Adapted From [50])

tube is driven sinusoidally at the midpoint through an eccentric cylinder-cam pair and the resulting velocity fluctuations in the neighbouring streamtube are measured with a hotwire anemometer. The tube motion is monitored with the use of an accelerometer and the correlation of velocity and acceleration data should yield the phase difference between tube motion and the velocity fluctuations. The decay function can be obtained directly from the velocity fluctuation measurements.

This test section was designed for the existing wind tunnel in McMaster University [37, 38]. The test section dimensions shown in figure 5.2 are quite satisfactory for the purposes of this study.

5.1.1 Determination of the Tube Diameter

Grover [37] and El-Kashlan [38] conducted their experimental studies on the existing facility. Their data for the parallel triangular array with pitch ratio, P_r, of 1.375 has been used by Lever and Weaver [23-25] for comparison. For consistency, it was decided to design the test rig for the same array geometry with $P_r = 1.375$.

Since it was the intention of this study to determine the phase and decay functions as a function of position, velocity fluctuations have to be measured along a streamtube at different locations. This is accomplished by moving the hotwire probe along the stream tube. A traversing mechanism is used for this purpose. The tube diameter is chosen to be as large as possible, so that there is sufficient space in the array for the hotwire probe to

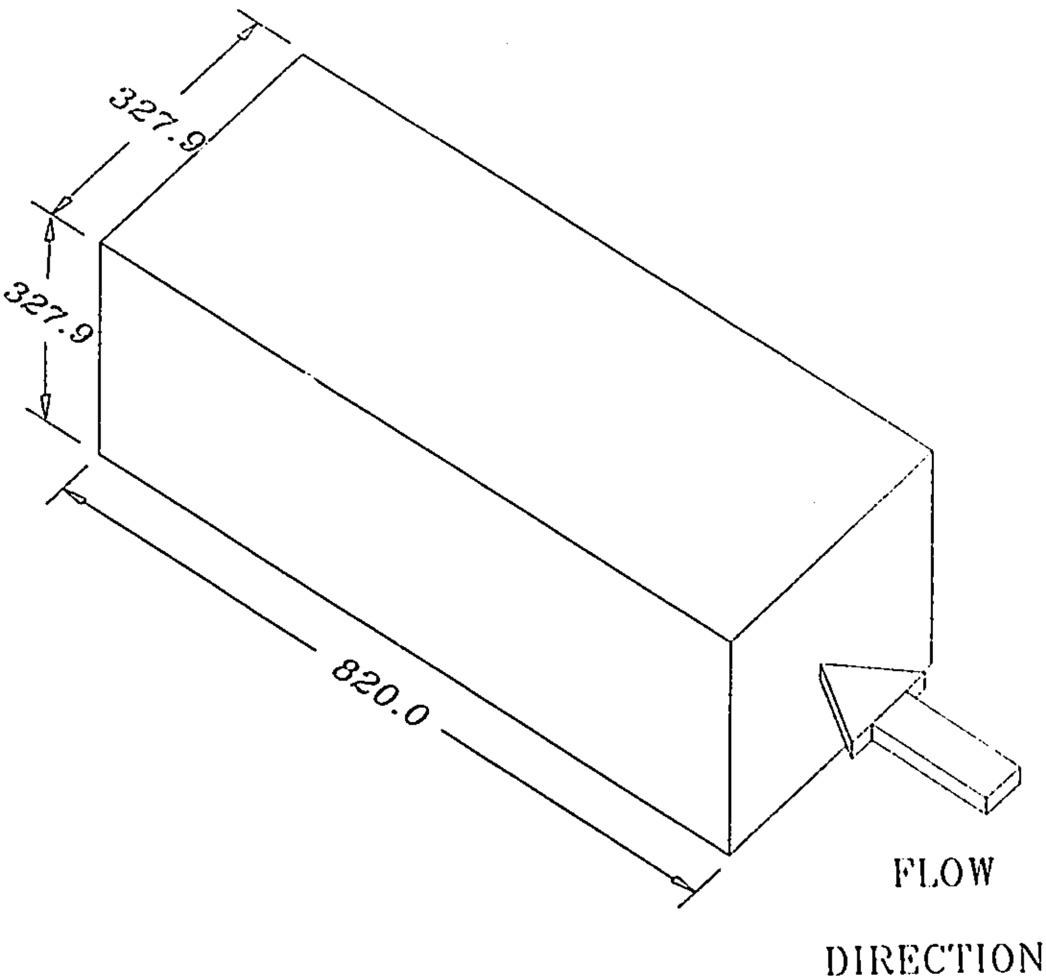

Figure 5.2 Dimensions of the test section

move safely. For the unit cell to be complete, there must be at least five rows and three columns of tube. In order to simulate a characteristic unit cell deep inside the array, three upstream rows and a downstream row were added. Hence, the number of rows increased to nine. For the given pitch ratio, P_r=1.375, and the minimum required number of 3 columns, the tube diameter was found to be 62.5 mm. Since, the largest available tube size was 50.8 mm, the array was designed to have 4 columns with P_r= 1.375. In order to eliminate the wall effects, half tubes were used on the side walls at appropriate positions. The final arrangement is shown in figure 5.3.

5.1.2 Traversing Mechanism

The traversing mechanism consists of two disks as shown in figure 5.4(b). The hotwire probe is attached to the smaller disk eccentrically. By rotating the large disc and the small disk, the hotwire probe can be positioned anywhere in the shaded area shown in figure 5.4(a). Two of these mechanisms, one for upstream and the other for downstream measurements, are installed on the top plate of the test rig.

5.1.3 Shaker Mechanism

The theory presented in this thesis assumes simple harmonic motion of the tube, hence, experiments must simulate this basic assumption. There are two mechanisms that can produce reciprocating simple harmonic motion. These are (i) the scotch yoke mechanism, and (ii) the eccentric cylindrical cam-follower pair (figure 5.5). Scotch yoke mechanisms are not suitable for high frequencies because of the backlash of the slider in the scotch yoke. Hence, an eccentric cylindrical cam-follower mechanism was designed to shake the tube in the test rig. For this purpose Fatigue Dynamics Inc.'s VHS-40H variable speed fatigue testing machine was modified. A roller bearing was press fit around the eccentric shaft as shown in figure 5.6.

When the machine rotates, the follower moves back and forth sinusoidally. The stroke of the simple harmonic motion can be altered by changing the eccentricity of the fatigue testing machine. In this way, a stroke range of 0-50 mm (up to 10% of the tube diameter) can be obtained. The direct transverse load on the shaft shouldn't exceed 40 lbs (≅ 200 N) according to the specifications given for the testing machine. It is also specified that the maximum rotation speed is 30 Hz.

The desired motion of the tube is $y(t) = Ye^{iwt}$ where, Y is in the range (1%-10%)d. For a given frequency, forces will be largest in the case where the maximum stroke of Y = 0.1d ≅ 5 mm. Therefore, the spring was chosen for the worst case when Y = 0.1d. In summary, the desired mechanism must be designed keeping in mind the following;

Limitations : Maximum load = 40 lbs (≅ 200 N)
Maximum frequency = 30 Hz
Requirement : Y_{max} = 5 mm (maximum stroke)

5.2 Dynamic Analysis of the Cam-follower

The free body diagram of the follower is shown in figure 5.7. Here, $f_c(t)$ is the contact force between the bearing and the follower. In addition to $f_c(t)$, the inertial force of the bearing

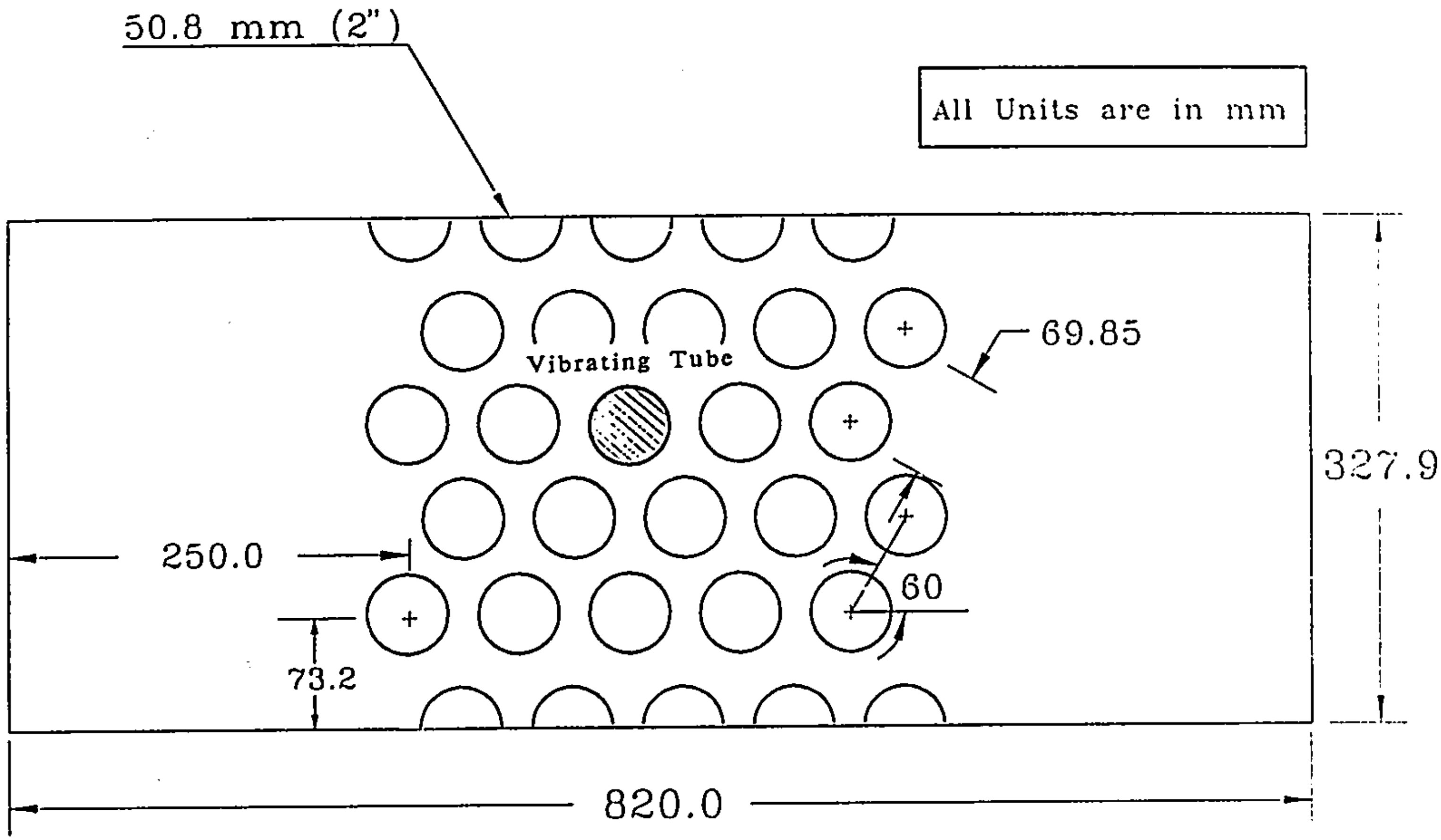

Figure 5.3 Top View of the Test Array Chosen for the Study

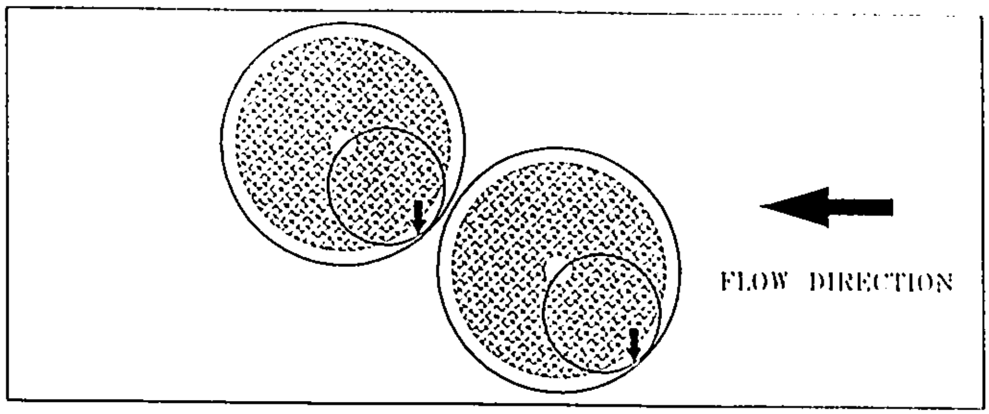

(a) Top View

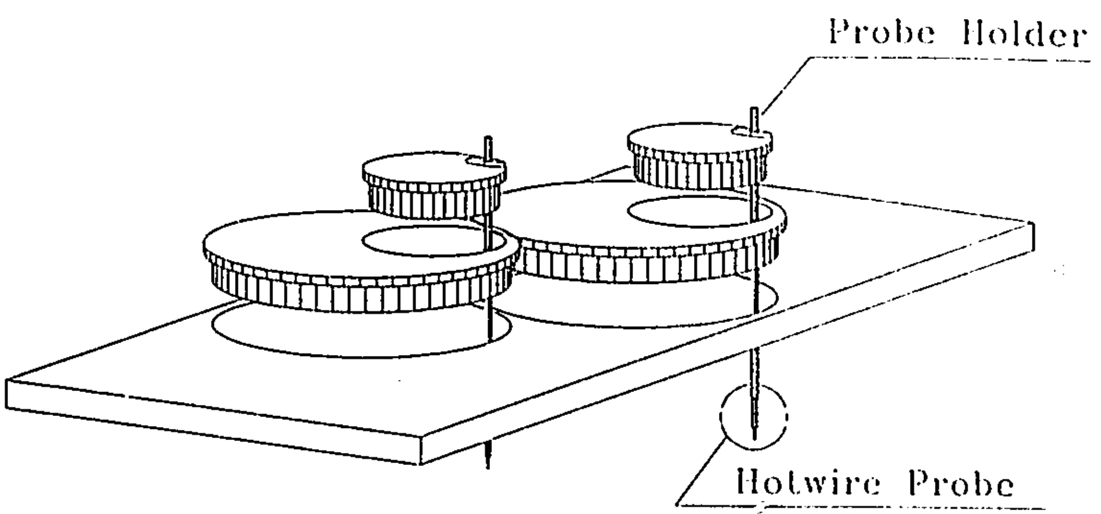

(b) Exploded View

Figure 5.4 Traversing Mechanism

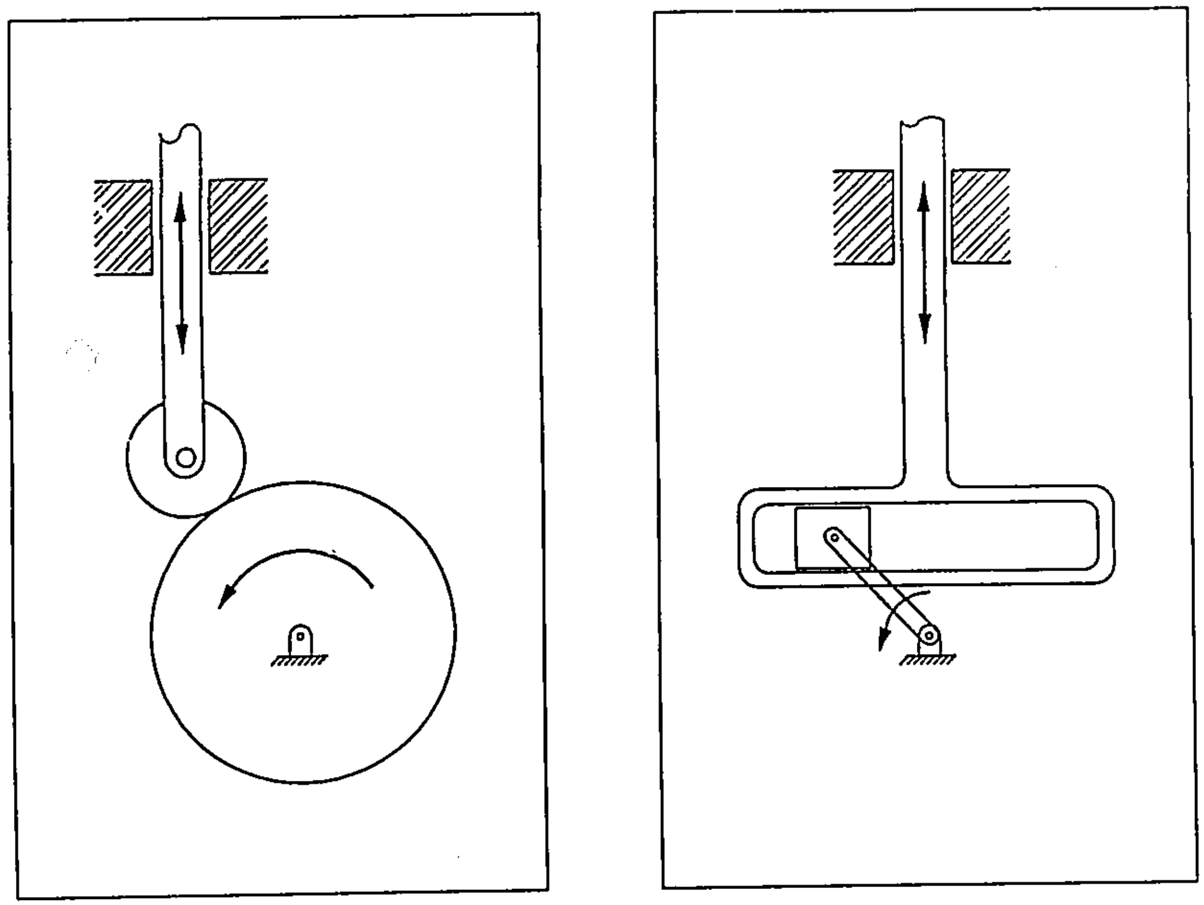

Figure 5.5 Mechanisms that can produce Simple harmonic motion

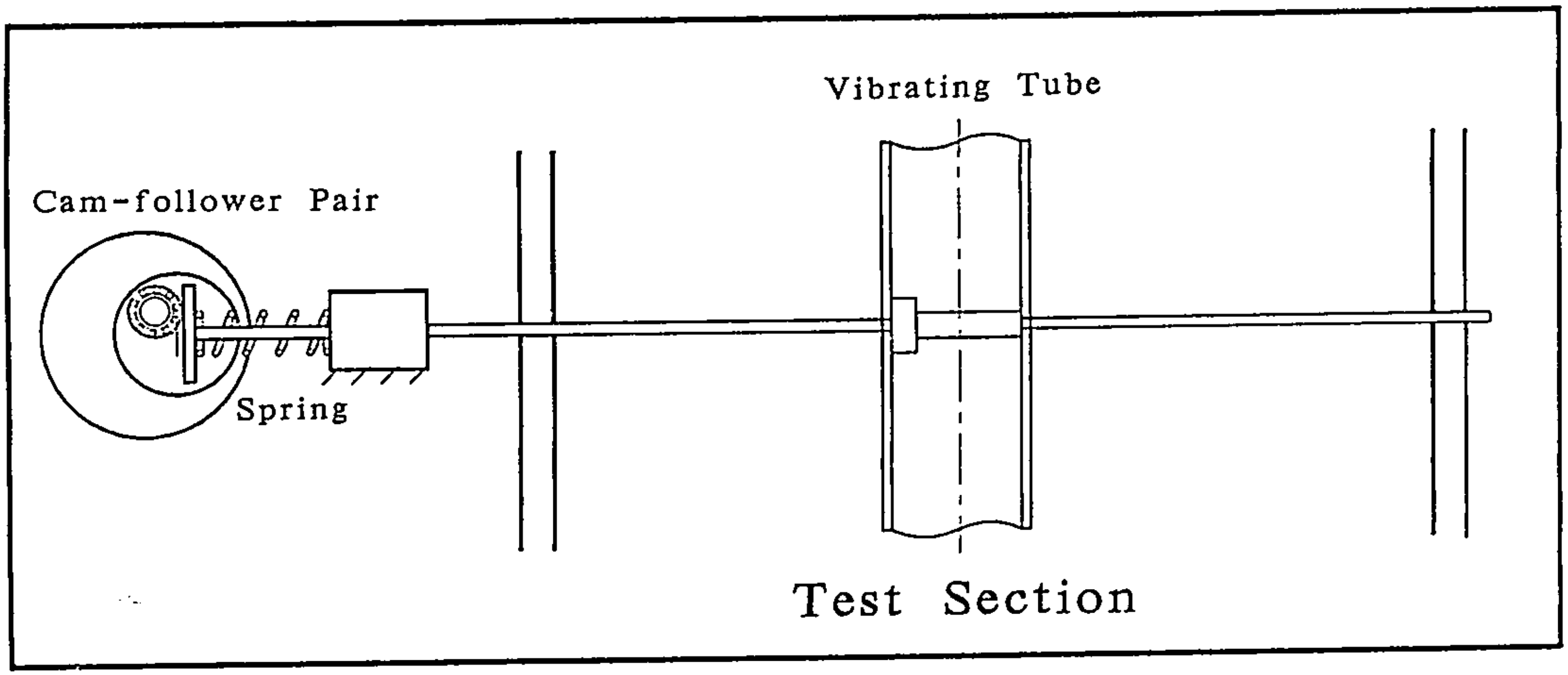

Figure 5.6 Schematic Drawing of the Shaker Mechanism

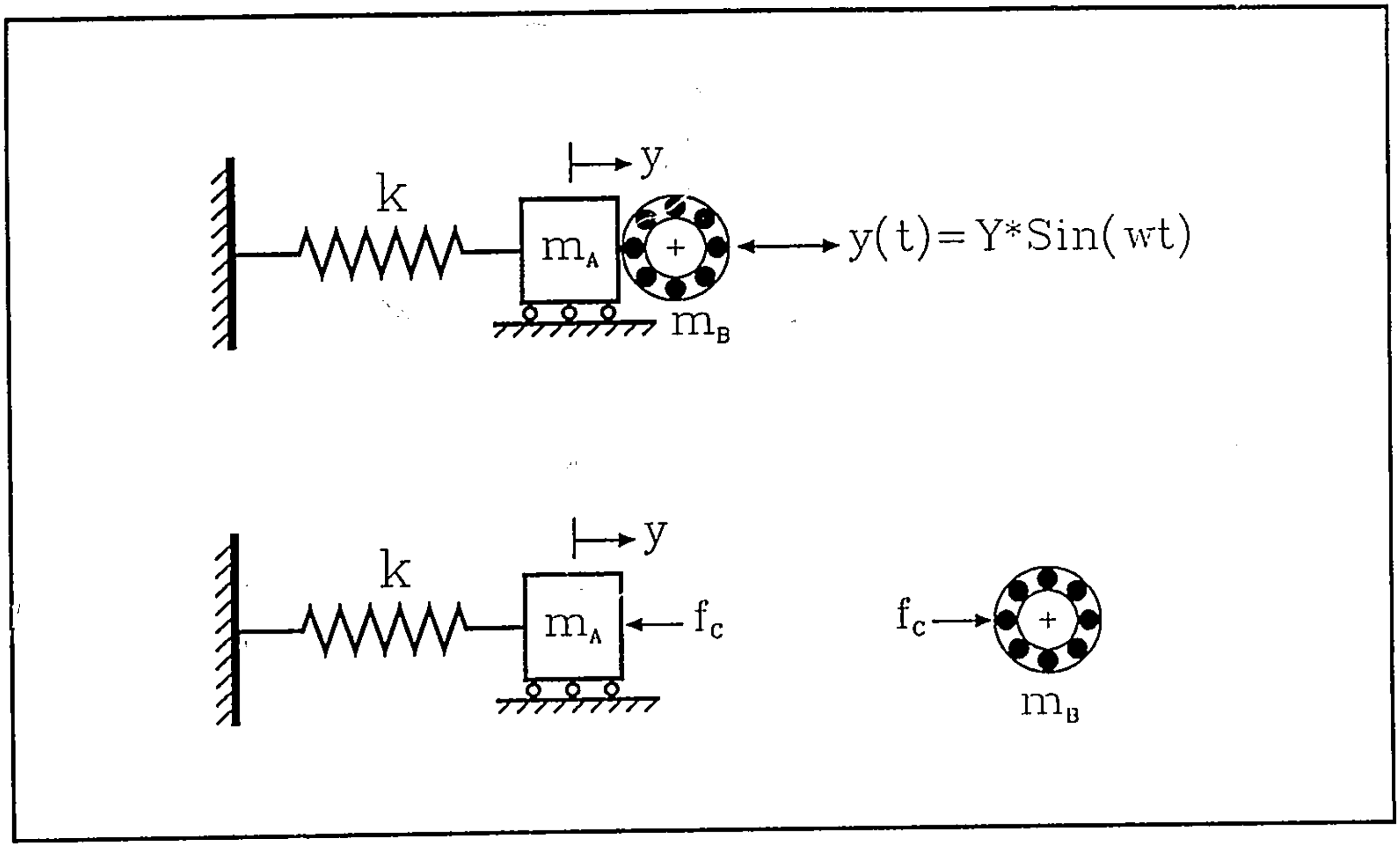

Figure 5.7 Body Diagram of the Cam-Follower Pair

$m_B\ddot{y}(t)$, will be carried by the fatigue testing machine. Therefore, the equations of the motion for the vibrating system can be written as :

$$\left.\begin{aligned} &m_A\ddot{y}(t) + ky(t) = f_c(t) && \text{(a)} \\ &m_B\ddot{y}(t) = f(t) - f_c(t) && \text{(b)} \end{aligned}\right\} \qquad (5.1)$$

where m_A is the total mass of the moving tube, the connecting rod, the spring and the accelerometer. By eliminating $f_c(t)$, equation (5.1) can be written in a compact form, to determine the total force f(t) as given below :

$$(m_A + m_B)\ddot{y}(t) + ky(t) = f(t) \qquad (5.2)$$

where, $m_A = 1/3m_{spr} + m_{rod} + m_{tube} + m_{acc}$
m_B = mass of the roller bearing
k = stiffness

The requirement that the cam-follower is to be in contact at all time is; $f_c(t) > 0$. That is,

$$ky(t) > -m_B\ddot{y}(t) \qquad (5.3)$$

Substituting $y(t) = Y{*}e^{iwt}$ into equation (5.3) and rearranging, one can find the requirement for contact as;

$$\omega_n > \omega \qquad (5.4)$$

where, ω is the excitation frequency as given before, and $\omega_n = \sqrt{k/m_A}$ is the natural frequency of the follower-spring assembly. Since ω_{max} is given as 30 Hz, ω_n is chosen to be 30 Hz.

The load acting on the bearing shaft can be found from equation (5.2) as;

$$f(t) = (\omega_0^2 - \omega)y(t) \tag{5.5}$$

where $\omega_0 = \sqrt{k/(m_A+m_B)}$

Let, $f(t) = F*e^{iwt}$. Then the maximum load will be obtained when $y(t) = Y_{max}e^{iwt}$ and $\omega = 0$. Hence, the most critical case is when the spring is statically compressed to it's maximum deflection. As a result,

$$F_{max} = Y_{max}\omega_0^2 \tag{5.6}$$

The tube shaken by the cam-follower mechanism is an aluminum tube with a 50.8 mm outer diameter. Its weight is reduced by turning the tube to approximately 1 mm wall thickness while keeping the outer diameter 50.8 mm. The connecting rod is made of hardened steel with a 3 mm diameter. It is connected to the aluminum tube with nuts. The total weight of the tube-rod assembly is measured to be $m_A = .225$ kg. The weight of the spring is assumed to be 0.025 kg. This assumption will be checked after the selection of the spring. A 1" ball bearing that can carry 200 N is chosen to install on the shaft of the fatigue testing machine. Its weight is specified as $m_B = 0.05$ kg. Since, $Y_{max} = 5$ mm and $\omega_0 = \sqrt{m_A/(m_A+m_B)} * \omega_n$. ω_n is already determined as 30 Hz. Therefore, for the worst case $F_{max} \cong 145$ N which is less than the maximum allowable load of 200 N. Therefore, the mechanism is capable of satisfying the requirements. Note that the friction force which might arise due to the motion of the rod with respect to the stationary test rig is not modelled. From the calculations presented above, a maximum friction force of 55 N is allowed. This is much higher than the practical range of the friction force expected for the design.

5.2.1 Selection of the Spring

In the previous section, the natural frequency is determined to be 30 Hz. The spring constant, then, can be found as;

$$k = m_A \omega_n^2 \tag{5.7}$$

For m_A = .225 kg, the spring constant is found to be : k = 8000 N/m. A die spring with a 4 cm length and a 4 mm internal diameter is chosen. Its weight is less than the assumed 0.025 kg, therefore the initial assumption of the spring weight was conservative and the design is satisfactory.

5.3 INSTRUMENTATION

The velocity fluctuations are measured with a miniature general purpose hotwire probe (DISA type 55P11). The probe output is connected to a dual channel FFT analyzer (Nicolet 660B) for signal processing. The tube motion is monitored with an accelerometer attached to the shaker mechanism. The accelerometer output is connected to the first channel of the FFT analyzer.

5.4 REYNOLDS NUMBER

The Reynolds number, Re, of the flow does not play an important role in many flow induced vibration problems. This is primarily because neither the drag coefficient nor the Strouhal number vary significantly over a significant range of practical flow velocities. However, very low Reynolds numbers should be avoided, since the drag coefficients and the Strouhal numbers show strong Reynolds number dependence in this range. For isolated circular cylinders, at about Re = 300, vorticies formed behind the cylinder undergo a transition from laminar to turbulent. Similarly, in the range $Re = 3x10^5 - 3.5x10^6$ transition of the boundary layer of the cylinder from laminar to turbulent should be expected. Such transitions cause the flow field to change significantly. Hence, they must be kept in mind when designing experiments and analyzing the experimental data.

It is found that the velocity fluctuations are measurable when the flow velocity at the minimum gap between tubes is less than about 25 m/s. At velocities higher than 25 m/s, turbulence levels, and hence the noise to signal ratio becomes too large to obtain good measurements. Additionally, reliable measurements could be obtained only for the minimum gap velocities greater than 2.5 m/s. This was attributed to the hotwire probe sensitivity at low velocities. Using the kinematic viscosity of air at 20°C, $\nu = 1.5 \cdot 10^{-5}$ m^2/s, and a tube diameter of d = 0.05 m, the Reynolds number range based on the minimum gap velocity is determined as :

$$Re = \frac{U_o d}{\nu} = 0.8x10^4 \text{ to } 8.0 \cdot 10^4 \tag{5.8}$$

This range is within the typical range of most experimental data in the literature. Hence the test velocity range is acceptable.

5.5 EXPERIMENTAL TECHNIQUE

The time domain signals of the hotwire probe, $x_h(t)$, and the accelerometer, $x_a(t)$, are transformed to the frequency domain by using the fourier transformation :

$$
\begin{aligned}
X_h(f) &= \int_0^T x_h(t)e^{-i2\pi ft}dt \\
X_a(f) &= \int_0^T x_a(t)e^{-i2\pi ft}dt
\end{aligned}
\qquad (5.9)
$$

where T is the time interval during which $x_a(t)$ and $x_h(t)$ are measured. The amplitude of the velocity fluctuation is determined from the peak in $X_h(f)$ that corresponds to the excitation frequency, f_{exc}. The transfer function between these two signal is defined [51] as:

$$H_{a-h}(f) = \frac{X_h(f)}{X_a(f)} \qquad (5.10)$$

The phase difference between these two signals can be determined from the transfer function :

$$\phi_{a-h}(f) = \text{Atan}\left[\frac{\text{Imag}(H_{a-h}(f))}{\text{Real}(H_{a-h}(f))}\right] \qquad (5.11)$$

The frequency domain data is averaged 64 times to determine the amplitude of the velocity fluctuations and the phase difference between the accelerometer and the hotwire signals. It should be noted that the dual channel FFT analyzer used in the experiments has a built-in function to determine $H_{a-h}(f)$, hence no computation is needed.

5.6 RESULTS

As mentioned earlier, the experiments were conducted on a parallel triangular tube array with $P_r = 1.375$, and $d = 50.8$ mm. The intention of this study was to determine the phase and decay functions for this array as functions of the mean flow velocity and the position along the streamtube. The accelerometer and the linearized hotwire signals were used in equation (5.11) to determine the phase angle. Unfortunately, the measured phase information appeared very confusing with no discernible trends, and therefore will not be presented here. It is the author's feeling that the reason for the unexplained, and seemingly unsystematic behavior of the measured phase angles is the complexity of the flow field and high noise-to-signal ratio. It is possible that the fluctuating velocity components are reflected from the rigid tube boundaries and superimposed on the velocity fluctuations propagating directly from the source. Acoustic propagation of the fluctuations might be affecting the results as well. In addition, the immediate area of the vibrating tube would experience the effect of propagating vortex structures generated by the tube vibration. All of this is superimposed on a high ambient turbulence generated by the tube bundle. In summary, the flow field is very complex, especially in the close proximity of the vibrating tube, and it is not straightforward to separate the effects of the different flow phenomena. Because of the unexplained behavior of the phase function, this part of the experimental study was abandoned to the author's great disappointment.

On the other hand, the measured values of the velocity fluctuations showed some systematic trends and the useful results are presented below.

When measuring the velocity fluctuations, noise in the probe signal due to the ambient turbulence affects the quality of the signal. In order to increase the signal to noise ratio, the amplitude of the tube vibration is set to 10% of the tube diameter. In reality, the amplitude of tube vibration seldom exceeds 2% of the tube diameter at the stability threshold. Hence, it is important to determine whether the large amplitude (0.1d) tube vibration testing would provide data applicable for the small amplitude (0.02d) tube vibration. Figure 5.8 shows the effect of the amplitude of vibration on the amplitude of the velocity fluctuation for various frequencies of vibration at position 3U in figure 5.9. The results regarding the perturbation velocity amplitude, including the ones which will be presented in the following sections, are normalized with respect to the average value of the perturbation velocity amplitude at $s = 0$ (location 0 in figure 5.9) so that $f(s) = 1$ at $s = 0$. This reference value is obtained by averaging the velocity perturbation amplitude at $s=0$ for various flow velocities when the vibration frequency is 12.5 Hz

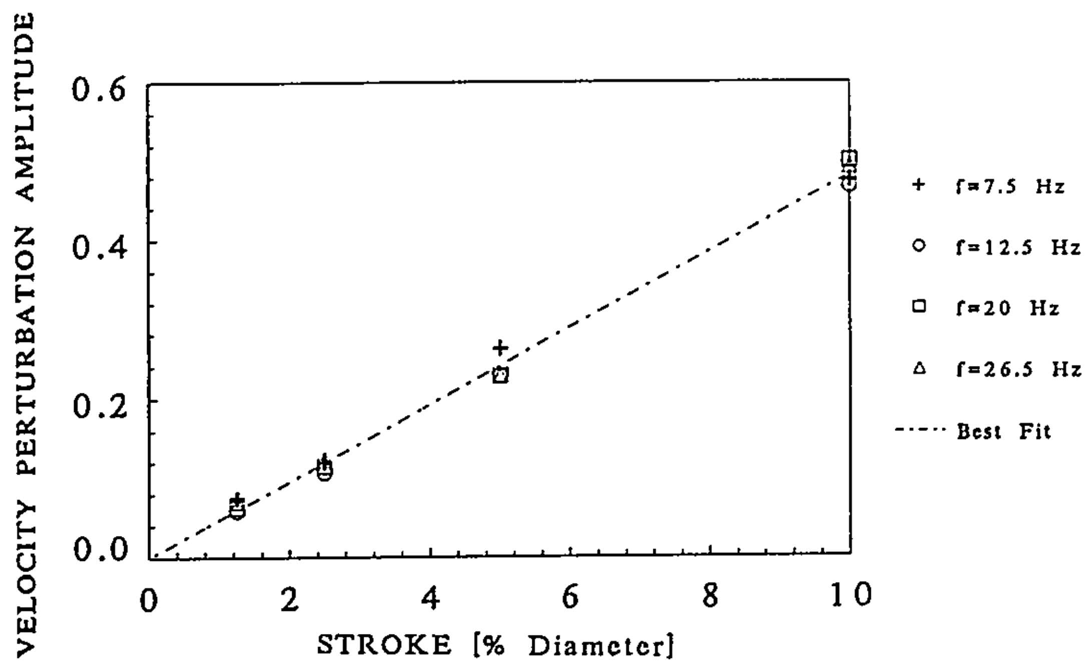

Figure 5.8 Effect of the Amplitude of the Tube Vibration on the Velocity Fluctuation.

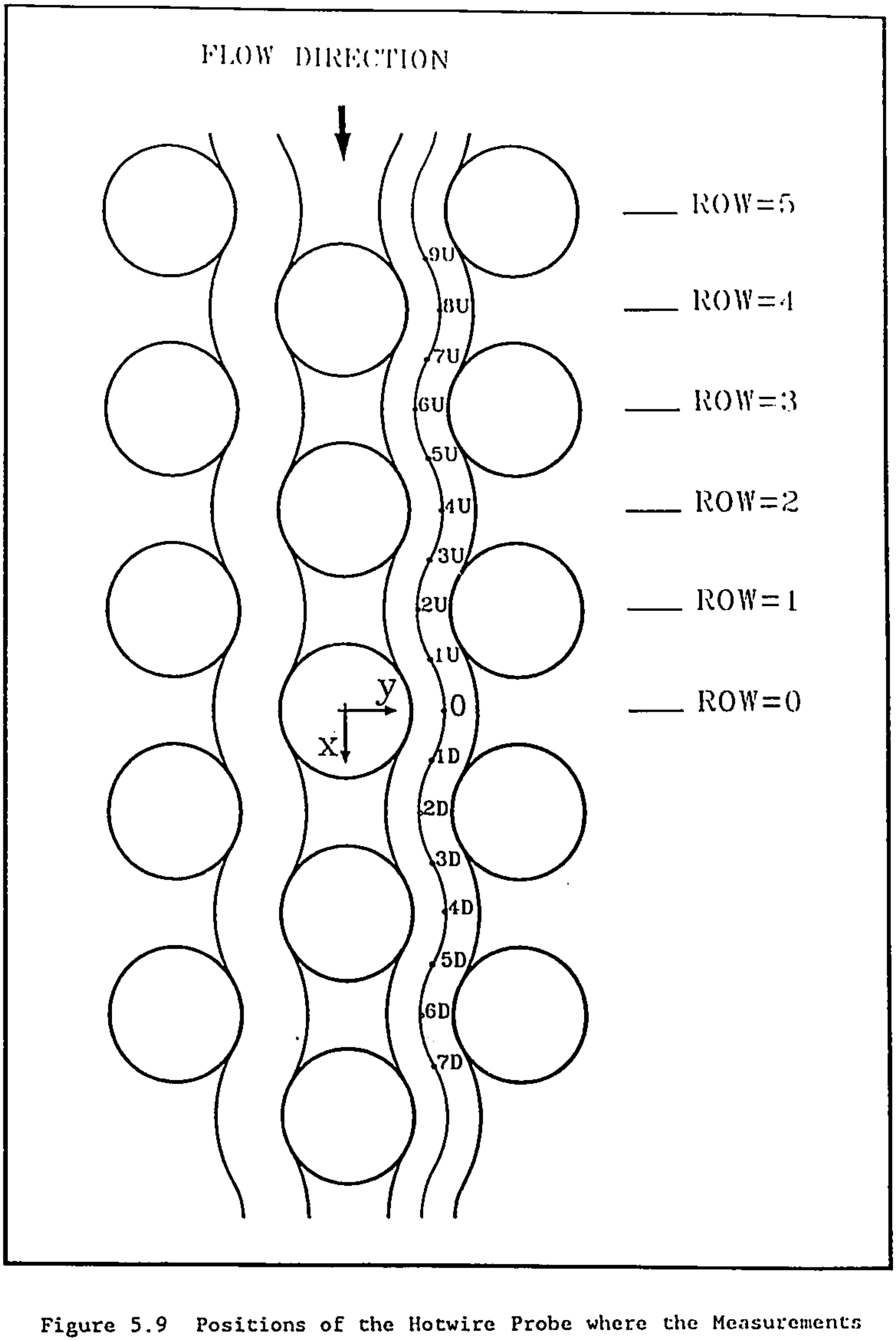

Figure 5.9 Positions of the Hotwire Probe where the Measurements are Taken

and the vibration stroke is 0.1d. In figure 5.8, excellent linearity is found between the velocity perturbation amplitude and the vibration stroke for all the frequencies at $Re=2.0 \cdot 10^4$. It is concluded that the results obtained using a tube vibration amplitude of 0.1d can be used to study the small amplitude vibration behavior with the advantage that the signal to noise ratio is improved significantly.

5.6.1 The Effect of the Mean Flow Velocity

In order to determine the effect of the mean flow velocity, the probe is located at different positions in upstream and downstream regions as shown in figure 5.9. At every location, the mean flow velocity is varied and the time domain probe signal is transformed to the frequency domain through the built in Fast Fourier Transformation (FFT) function in the FFT Analyzer. The amplitude of the fluctuating velocity, then, is determined from the peak corresponding to the vibration frequency. In general, the coherence was greater than 0.85 showing that the signal to noise ratio is satisfactory, and the system behaves linearly. A typical result at point 3U is shown in figure 5.10. The amplitude of the velocity fluctuation is reasonably constant over the range $10^4 < Re < 4 \times 10^4$. At a Reynolds Number $4 \cdot 10^4$, there appears to be a drop in the amplitude of the fluctuating velocity. Repeated experiments verified these results. The reason for this drop may be the transition from a laminar to a turbulent boundary layer on the tubes.

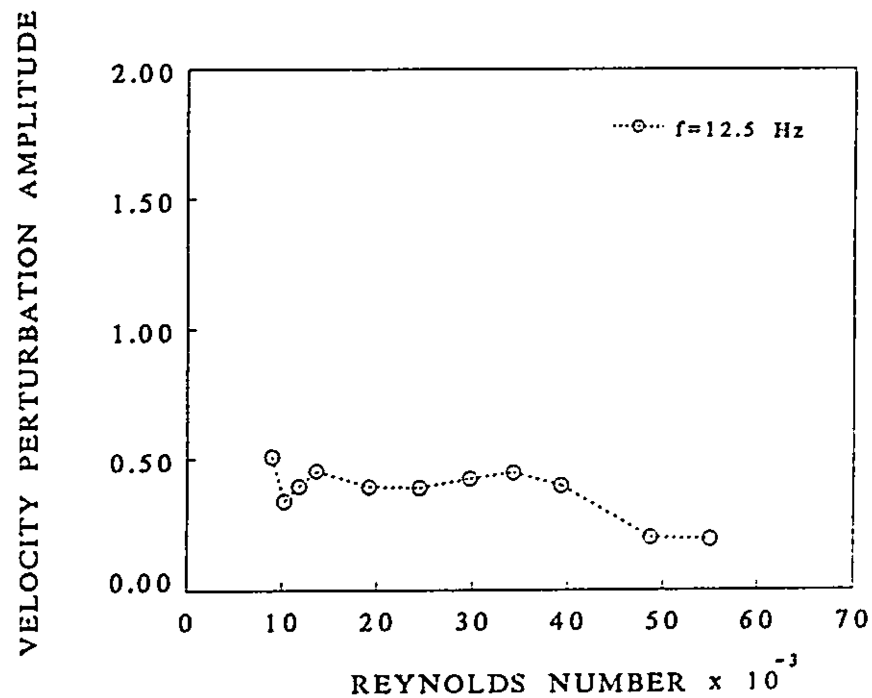

Figure 5.10 Amplitude of Velocity Fluctuation at position 3U as a Function of the Mean Flow Velocity

5.6.2 The Effect of the Vibration Frequency

Figure 5.11 shows the effect of the vibration frequency on the velocity perturbation amplitude as a function of Reynolds number at location 3U. As can be seen, the vibration frequency over the range of frequencies tested has little effect on the trends observed in the previous section. The scatter in the data at Re < 10^4 is thought to be caused by the poor signal to noise ratio at low flow velocities.

5.6.3 The Effect of the Position

Similar results to the those shown in figure 5.10 are obtained at different locations by traversing the streamtube with the hot wire probe. The amplitude of the velocity fluctuation is shown in figure 5.12 for every upstream location shown in figure 5.9. The variation in the measured amplitudes at each location is shown by the error bars. Although the variation is fairly large at some locations, especially at position 2U, a clear trend of the decay as a function of position can be seen. As shown in figure 5.12, the velocity fluctuations are observed as far as 4 tube rows upstream from the vibrating tube. No measurable perturbations were detected at distances larger than 4 tube rows. The fluctuations at point 2U were sometimes unexpectedly large and may be due to vorticity generated by the driven tube. In any event, the decay of the fluctuations is clear and the upstream decay function is determined as follows:

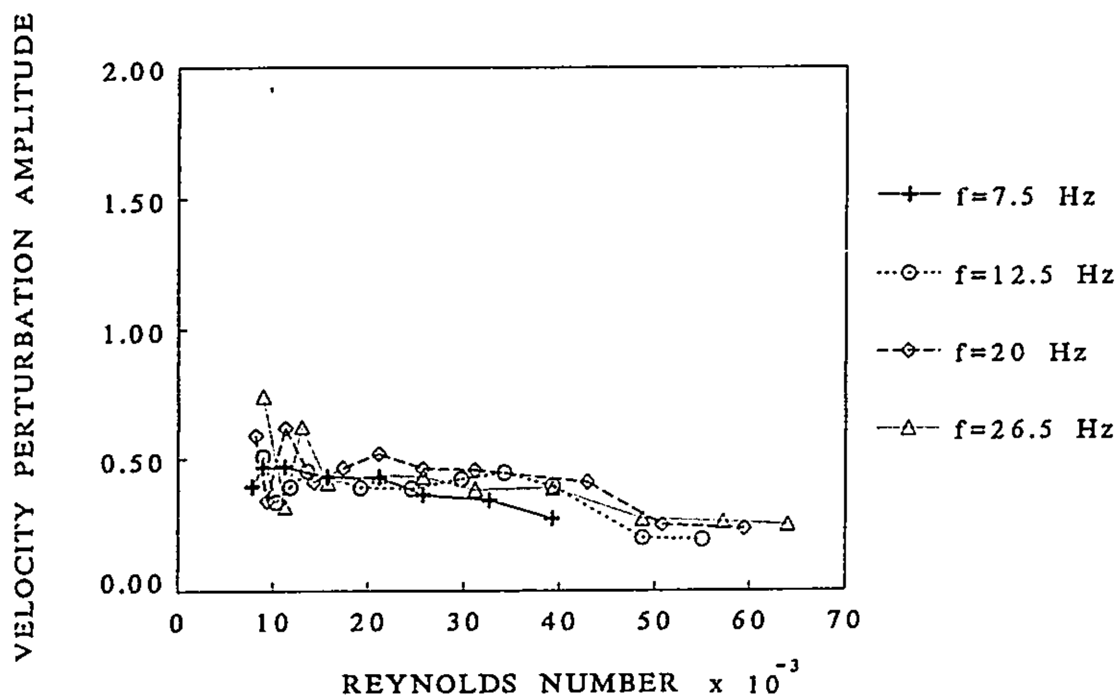

Figure 5.11 The Effect of the Frequency of Vibration on the Amplitude of the Velocity Fluctuation

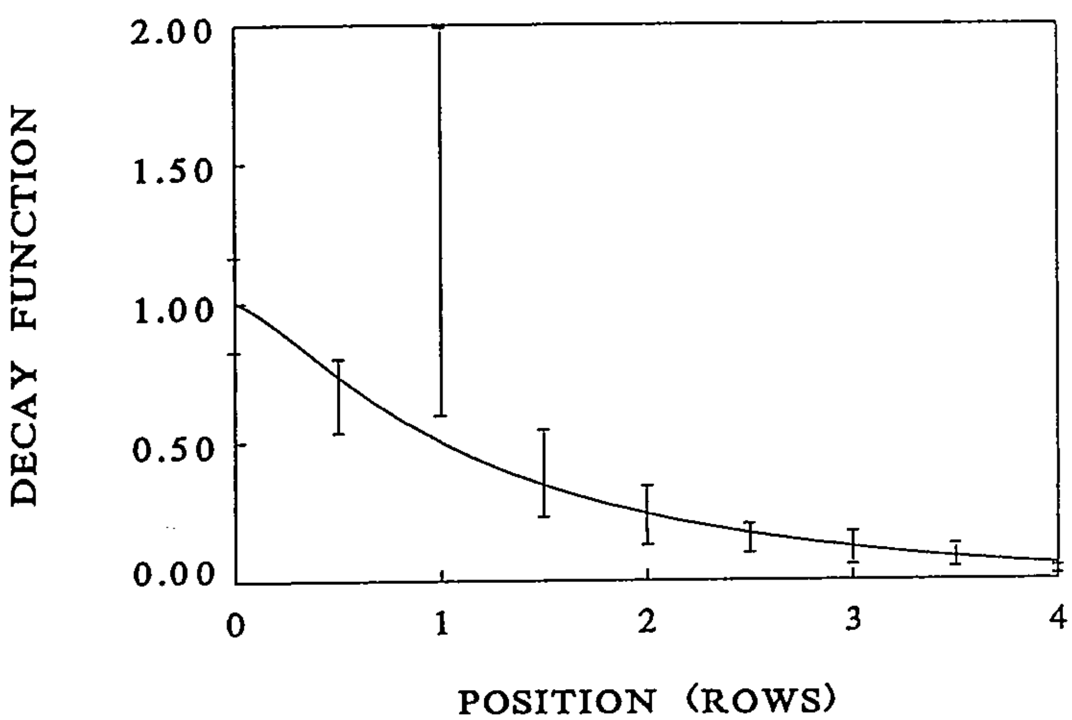

Figure 5.12 Experimentally Determined Upstream Decay Function (ROWS as shown in Figure 5.9)

$$f(s) = 1.05\left(\frac{1}{1 + 1.2 \cdot s^2} - 1 \right) + 1 \qquad (5.12)$$

When obtaining equation 5.12, numerical techniques such as least squares could not be used successfully due to the large deviation in the data at the 1st row. A successful approach might weight this questionable data point less than the others. However, instead of assuming such a weighing scheme, the coefficients 1.05 and 1.2 were determined by trial and error to obtain the solid line in figure 5.12.

Note that this decay function is normalized with respect to the average value of the measured velocity fluctuation at s = 0 (location 0 in figure 5.9) so that f(s) = 1 at s = 0. Also note that in the limiting case, when s is very large, f(s) approaches 0.0. In this study, it is assumed that the decay function shown in figure 5.12 is valid for other array geometries as well. When adapting equation (5.12) to other array geometries with different pitch ratios, the proper coordinate transformation should be done so that the value of $f(-s_1)$ is always the same. This can be done by replacing s with $s \cdot s_{1-30}/s_{1-\alpha}$, where $s_{1-30} = 2.88d$ is the position of the streamtube inlet for $\alpha = 30^\circ$ with $P_r = 1.375$ and $s_{1-\alpha}$ is the position of the streamtube inlet for an arbitrary geometry. Such a transformation ensures that the perturbations have decayed by a distance in 4 rows upstream of the vibrating tube.

In the downstream region, very large velocity fluctuations

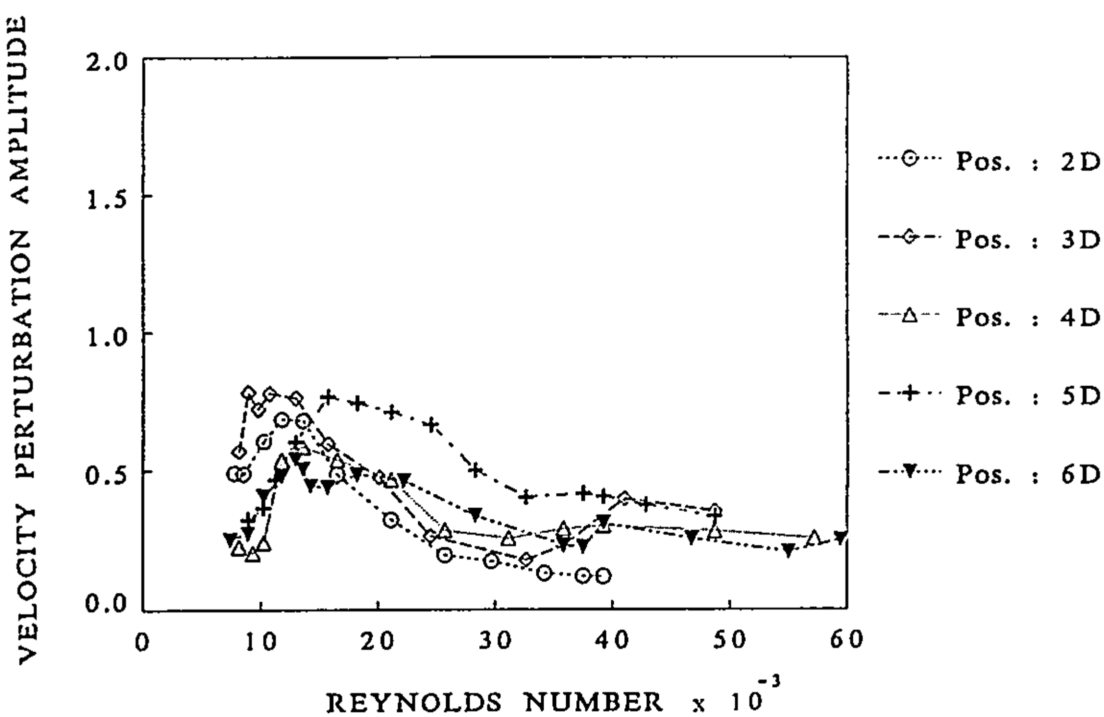

Figure 5.13 Downstream Velocity Fluctuations at Various Locations

are observed at Re < 5.0×10^4 at position 1D. This was thought to be caused by discrete vortex structures being shed from the vibrating tube. However, almost no decay was observed for the existing 3 downstream tube rows. This is probably because the fluctuations are vortical structures being convected with the mean flow. Some typical results obtained in different positions are shown in figure 5.13. These measurements imply, not surprisingly, that flow disturbances generated by a vibrating tube are convected many tube rows downstream. Thus, it is not possible from these experiments to determine the downstream inertial streamtube length which contribute to the phase lag.

5.6.4 Theoretical Prediction of Dynamic Instability by using the experimental decay function

Figure 5.14 shows the dynamic instability for the parallel triangular arrays as predicted by the present theoretical model by using the experimental decay function (equation 5.12). Since the velocity perturbations are measured up to 4 tube rows upstream the vibrating tube, the streamtube length is calculated along 4 tube rows. The rest of the parameters are the same as the ones used to obtain figure 4.7. As it can be seen from these figures, the predicted stability threshold is not affected significantly at U_r > 10. However, for U_r < 10 the predictions are significantly different. The reason for this is because, at high mass-damping ratios, the forces acting on the vibrating tubes are strongly

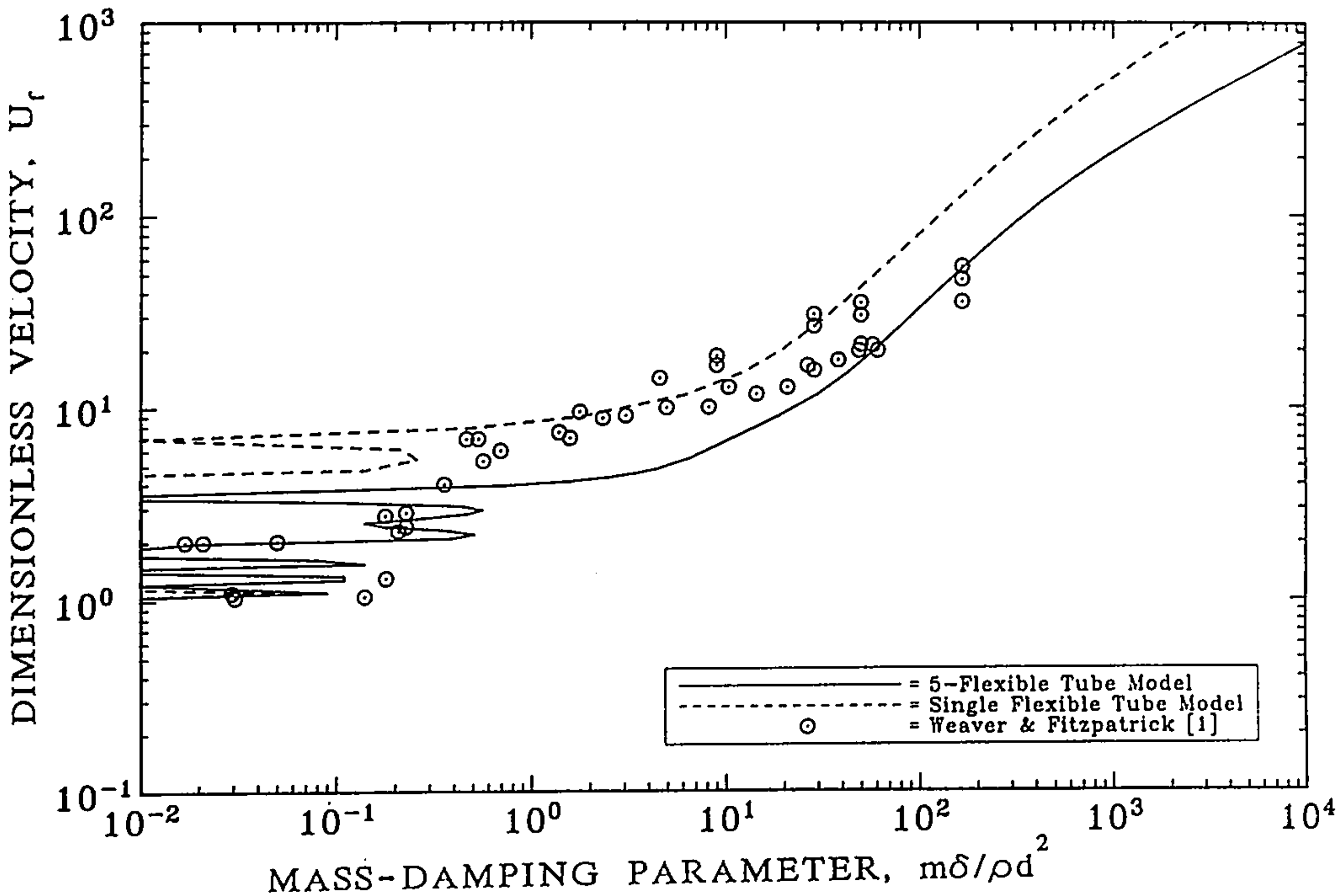

Figure 5.14 Dynamic instability for the Parallel Trianguar Arrays with Experimental Decay Function (P_r = 1.375).

affected by the displacements of the neighboring tubes but the phase angle is small. The streamtube length, therefore, does not affect the dynamic instability significantly. However, at low values of the mass-damping parameter, the inertia of the fluctuating fluid column plays an important role. Hence, the streamtube length is an important parameter in determining the dynamic instability threshold in this range of the mass-damping parameter.

The agreement between the experiments [1] and the present theoretical prediction with experimental streamtube length is reasonably good at high mass-damping parameters as can be seen in figure 5.14. However, at low mass-damping parameters, the agreement is not satisfactory as the results of the multiple tube model show many instability regions. As was discussed in chapter 4, the reason for these multiple instability regions is the unrealistic values of the phase function. For example, when the experimentally determined streamtube length is used, the present phase function predicts a phase difference of about 15π between a tube's motion and the fluid force acting on the tube due to its own motion at $U_r = 1.0$. Clearly, a phase difference of this magnitude is unrealistic. Therefore, this discrepancy points out to the deficiency of the phase function used in this study. Unfortunately, due to the reasons explained earlier, experimental study was not successful in determining the phase function.

It was hoped that these experiments would shed some light on the nature of the phase function and the decay of disturbances as a function of distance from the vibrating tube. It was assumed that the effective streamtube inertial length used in the phase function was related to the distance over which the decay of disturbances occurred. Clearly, using this assumption with the theoretical phase function produces unrealistic results. This is very disappointing because it means that there is no obvious way of incorporating any of the experimental results in the theoretical model. Thus, it was decided to abandon the experiments altogether and to carry out the final analysis using the Lever and Weaver model parameters. That model predicted experimental observations reasonably well at low values of the mass-damping parameter. The extensions to that theory developed in this thesis have overcome many of its shortcomings, especially at high values of the mass-damping parameter.

Future research must be directed towards the experimental determination of the phase function and the relationship between streamtube inertial length and decay of disturbances. The present study has shown the complexity of the fluidelastic mechanism and the difficulties in obtaining useful results. It seems that the very high turbulence levels generated by the tube array make studying the fluid excitation mechanism especially difficult.

CHAPTER 6
RESULTS AND DISCUSSION

The present study focuses on the theoretical aspects of fluidelastic instability in heat exchangers. For this purpose, Lever and Weaver's [24-25] theory has been modified and extended to include the effects of neighboring tube motion. In this section, a summary of the the present theoretical findings and a detailed discussion about the stiffness and damping dominated dynamic instability mechanisms are given. Predicted theoretical results are presented for the stability thresholds for all four standard heat exchanger tube array geometries. These predictions are compared with experimental data from the literature. The effects of various parameters on the theoretical model are investigated. To set the stage for these calculations an overview of the theoretical model is presented and discussed.

6.1 THEORETICAL RESULTS AND DISCUSSION

The results of the theoretical developments presented in chapters 3 and 4 provided some valuable insights into the model behavior. These results were discussed in detail previously, and therefore, only a summary of the important findings will be given here.

6.1.1 Single Flexible Tube in an Array

As mentioned in chapter 3, the modifications to Lever and Weaver's single flexible tube model overcame the theoretical anomalies and improved the agreement with experimental results and other theoretical models. The following are the major improvements and findings from the single flexible tube model.

(1) Decay Function : In a proper dynamic model, when all the time dependent terms are set to zero, the dynamic solution should reduce to the static solution. However, Lever and Weaver's theory on the dynamic instability of heat exchanger tubes does not produce this static instability. It was found that the reason for this unexpected behavior is the finite area perturbation value at the streamtube inlet, $s = -s_1$, where velocity and pressure perturbations are set to zero. In a more consistent model, all the perturbations should be approximately zero at the inlet point $s = -s_1$. Figure 6.1(a) shows a typical area perturbation as modelled by Lever and Weaver. When the time dependent terms (and the phase function, $\phi(s)$) are set to zero, the area perturbation becomes constant along a streamtube. Therefore, the magnitude of the velocity and pressure perturbations along the streamtube are constant and equal to their zero boundary values at $s = -s_1$. It follows that no static instability can be predicted. However, when the perturbations created by the vibrating tube propagate, their amplitudes should become smaller because of dissipation effects. In the present study, the decay of the perturbations is modelled by introducing a decay function, $f(s)$, in the theoretical model. The

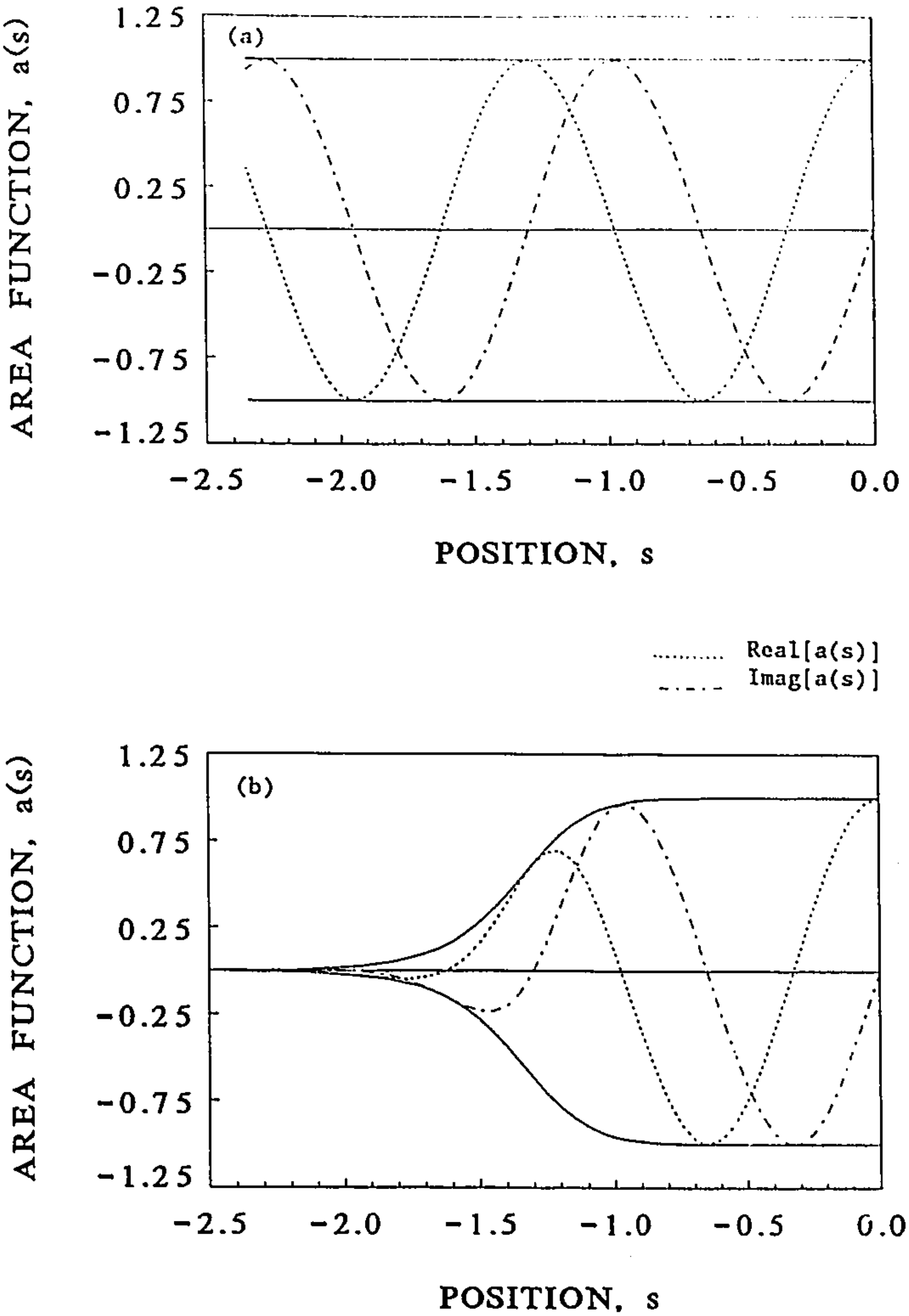

Figure 6.1 The Effect of the Decay Function on Area Fluctuations (a) Lever & Weaver [24] (no decay), (b) Proposed Decay Function

effect of this function is to set the area perturbation to a negligible value at the streamtube inlet, $s = -s_1$, so that the area fluctuation is consistent with the forced boundary conditions of zero velocity and pressure fluctuations. A typical area perturbation with the decay function is shown in figure 6.1(b). If the time dependent terms are set to zero, the phase function, $\phi(s)$, becomes zero everywhere along the streamtube and the unit area perturbation function becomes the same as the decay function, f(s). As a result, even if the time dependent terms are zero, an area perturbation is produced and divergence predicted. Interestingly, the predicted static instability is quantitatively very close to Lever and Weaver's static instability solution obtained from their separate model. This is because the static instability is dominated by the change of area (caused by the tube motion with respect to the neighboring tubes) in the attached flow region. Since the modification introduced into the model essentially affects the overall fluid inertia while keeping the the fluid inertia at the attached flow region the same as before, static instability is not affected.

(2) Relaxing the Frequency Ratio, ω/ω_n : Previous researchers have assumed that $\omega/\omega_n = 1$ in their theoretical models when determining the critical dimensionless velocity. i.e., the tubes always become unstable at their natural frequency. This assumption causes some error for a single degree of freedom system at very high values of the mass-damping parameter, where the fluid stiffness forces (the real part of equation (3.26) are much larger than the fluid damping terms. At these values of the mass-damping

parameter, if ω/ω_n is set to unity, the real part of equation (3.26) which includes the fluid stiffness term cannot be satisfied. By relaxing ω/ω_n, the correct solution can be obtained. The results shown in figures 3.8 and 3.9 show the effect of relaxing the frequency ratio. As seen in figure 3.9, the dynamic solution approaches the static solution at very high values of the mass-damping parameters. At the same time, ω/ω_n approaches zero. This is to be expected, since the static instability solution is obtained by setting $\omega/\omega_n = 0$ in the dynamic stability analysis.

When the fluid stiffness forces are dominant in a single freedom system, dynamic instability tends towards divergence. This type of instability is different in nature than the stiffness controlled instability observed in multiple flexible tube arrays. In single degree of freedom systems, if the fluid stiffness terms are dominant, the frequency ratio becomes smaller than one, whereas in the multiple degrees of freedom systems, the frequency ratio is always approximately equal to one. It is the latter type of stiffness controlled instability that is predicted by Chen and Price & Païdoussis. As they discovered [6-8, 9-13], the fluid stiffness coupling with the neighboring tubes is the essential feature of tube array instability at high values of the mass-damping parameter. More will be mentioned about this in the following sections.

(3) Lever and Weaver's dynamic model predicted no streamwise dynamic instability. It was found that the reason for this behavior is the symmetric attachment and separation points about s = 0. In the attached flow region, Lever and Weaver assumed a zero

phase lag and varying amplitude area perturbation. As a result, pressure fluctuations in this area increased along the streamtube from the attachment point to the separation point. When the pressure fluctuation is integrated along the attachment surface of the tube, an opposing force was found. Hence, no streamwise dynamic instability is predicted. The present analysis predicts streamwise instability by using the attachment and separation points observed in the flow visualization experiments of Scott [44]. These attachment and separation points yield a higher projected area of the pressure fluctuations in the streamwise direction in favor of streamwise instability. Figure 3.13 shows the results with the new attachment and separation angles. It was found that the streamwise dynamic instability is always less critical than that of the transverse dynamic instability, therefore, the streamwise instability is not of practical concern.

6.1.2 Multiple Flexible Tube Model

An important difference between the models of Chen and of Price & Païdoussis and the single flexible tube model is that the former ones include the effect of relative tube motion. Indeed, it is this effect which generates their predicted fluid-stiffness dominated dynamic instability. In view of the observations of the present single flexible tube results and Chen and Price & Païdoussis' findings, it was thought that some improvement might be achieved by including the effects of the relative motion between neighboring tubes.

In the multiple tube analysis, the results show that the stiffness-controlled dynamic instability in multiple degrees of freedom is modelled successfully. It is found that the effects of the neighboring tubes are very important at high mass-damping parameter values. In the stiffness-controlled instability region, the slope of the stability curve is found to be 0.5 and the associated frequency ratio is about 1 over the whole range. This behavior is the same as the semi-empirical theories of Chen and Price & Païdoussis. By modelling the array behavior with the inclusion of the effects of neighboring tubes, the quantitative and qualitative agreement with the experiments is improved at high mass-damping parameter values.

6.2 MULTIPLE INSTABILITY REGIONS

Lever and Weaver's model predicted a large number of instability regions at low values of the mass-damping parameter. Interestingly, this behavior was also predicted by Price and Païdoussis' theoretical model. It was found that the reason for this behavior is the unrealistically high phase lag produced by Lever and Weaver's phase function at low values of dimensionless velocity. Figure 6.2 shows the phase function at $s = -s_1$. Every cycle of the phase function corresponds to an instability region in Lever and Weaver's solution (Figure 3.7). For example, at the dimensionless velocity of 1, the phase lag at $s = -s_1$ is equal to 20.9 radians (appx. 3 cycles). Incidentally, this dimensionless velocity lies in the third instability region. Not surprisingly, the same multiple instability regions are reported by Price & Païdoussis. In their model, the flow retardation parameter, a

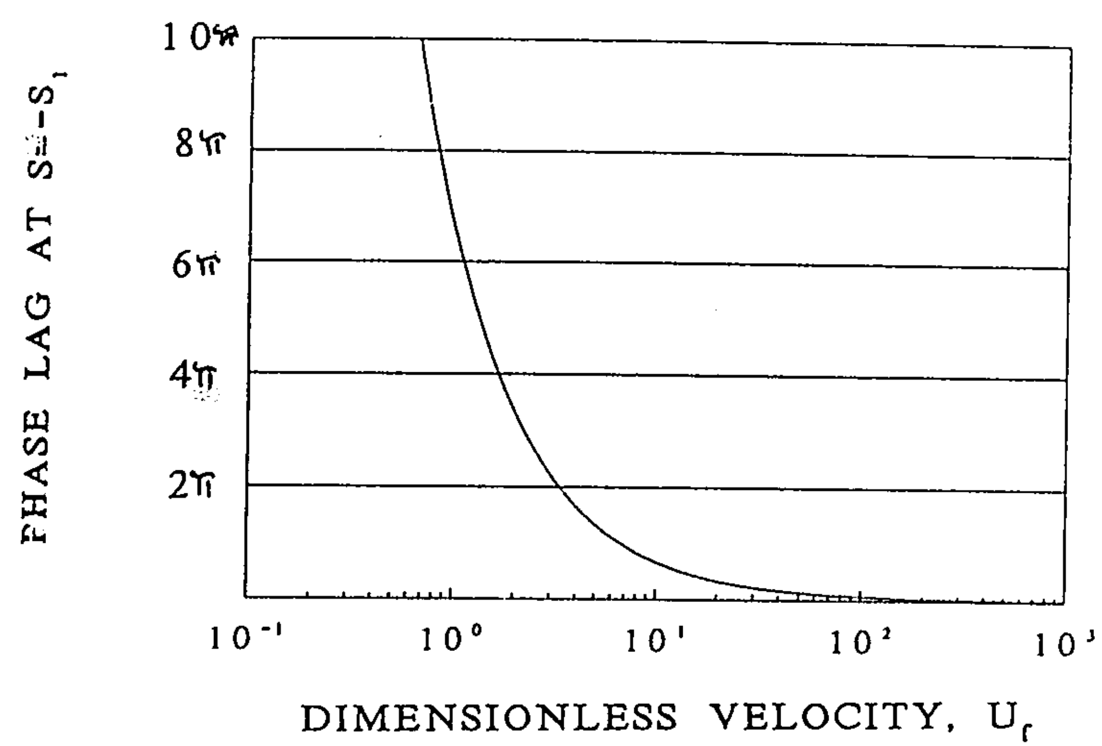

Figure 6.2 The Phase Function, $\phi(s)$, at $s = s_1$, as a Function of U_r

form of the phase function, becomes very large at low values of the dimensionless velocity and produces the multiple instability regions.

Physically, having the value of the phase function 6π at s = $-s_1$, means that the fluctuations created by the vibrating tube are felt at s = $-s_1$, 3 cycles of tube vibration after they are created. Intuitively, one would expect that the fluctuations would diminish earlier, perhaps within two cycles of tube vibration after they are created. Obviously, the phase function used in this study is too large at low dimensionless velocities and is responsible for the multiple instability regions. Since, no better alternative is found for the phase function, it will be used for all the results presented, but only three instability regions will be accepted. This is the same approach adopted by Lever and Weaver [23-25], and Price & Païdoussis [12].

6.3 MODEL PARAMETERS

The idealized flow fields for various array geometries are shown in figure 3.1. The evolved model parameters for various arrays are summarized in table 6.1. Lever and Weaver modelled the added damping and the pressure loss by using the steady state drag coefficient, c_D. In the present study, it was decided that using the steady state drag coefficient is not necessary, since no significant change in the stability threshold was observed by neglecting these terms. Hence, for the following final results, these terms are set to zero. Also, the streamtube length, based on

Configuration	α	A_o^*	s_1^*	$\beta_1^{\otimes}$	$\beta_2^{\otimes}$
In-Line Square	0°	$P_r - 1$	P_r*ROW	10°	10°
Parallel Triangle	30°		$P_r \alpha$*ROW	40°	10°
Rotated Square ($P_r \leq 1.7$)	45°			75°	15°
Rotated Square ($P_r > 1.7$)	45°	$P_r \cos(\alpha)-0.5$	$P_r[\alpha+\sin(\alpha)]/2$*ROW	85° †	15° †
Rotated Triangle	60°			85°	15°

$$l_o^* = 2\,s_1^*\ , \quad s_a^* = -\beta_1/2\ , \quad s_s^* = \beta_2/2$$

⊗ From [44] , ROW = 4

† β_1 and β_2 for this array is assumed to be the same as rotated trianguler arrays

Table 6.1 Model Parameters for Various Arrays table 6.1 and applying the artificial downstream pressure decay, the unsteady force coefficients acting on the tubes in an array can be determined. As mentioned earlier, the model is general for all arrays and no new experimental measurements are necessary to predict the critical flow velocities in other arrays. The only experimental data used in constructing the model are the attachment and separation angles from Scott's study [44]. These angles are obtained from flow visualization pictures. Careful investigation over a range of flow rates showed little variation in attachment and detachment angles. Hence, these angles as listed in table 6.1 are assumed valid for all flow conditions and pitch ratios. Figure 6.3 shows the predicted fluidelastic instability for the parallel triangular arrays with P_r = 1.5. The parameters used are the same as the ones used to obtain figure 4.7. These results are discussed in terms of the mechanisms generating the instability in the following section. The results for the other standard arrays are presented in section 6.6.

6.4 DAMPING-CONTROLLED AND STIFFNESS-CONTROLLED DYNAMIC INSTABILITY MECHANISMS

The fluidelastic instability mechanism has been reported [6-8, 9-13] as the combination of two mechanisms. One of these mechanisms is the stiffness-controlled dynamic instability mechanism that is dominant for high mass-damping parameters. In

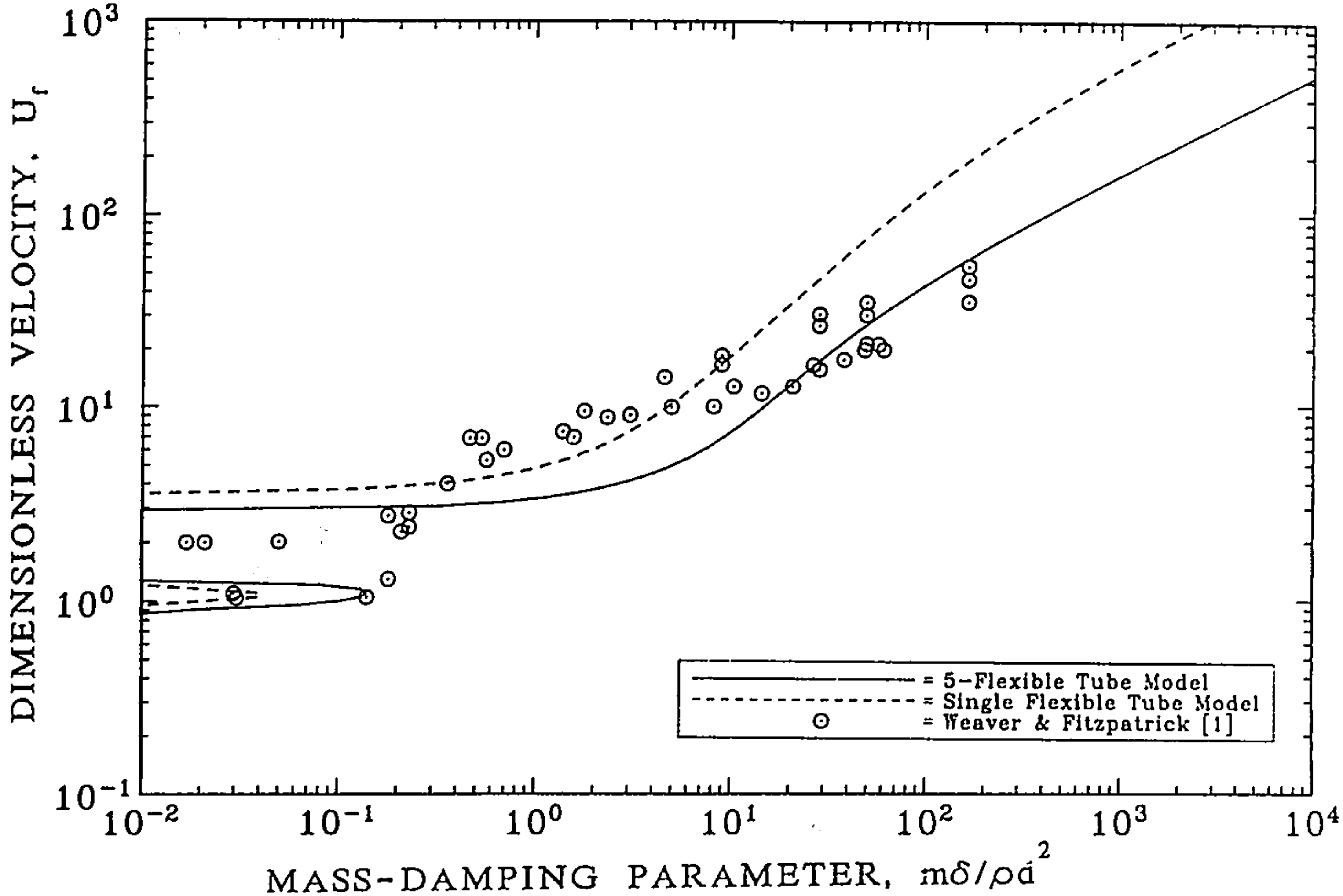

Figure 6.3 Present Theoretical Prediction of the Dynamic Instability for the Parallel Triangular Arrays with $P_r = 1.5$

this mechanism, the fluid stiffness forces due to the neighboring tube motion results in the tube's becoming dynamically unstable. The second mechanism is the damping controlled dynamic instability that is dominant at low mass-damping parameters. In this type of instability, neighboring tubes' effect is not important and a tube goes dynamically unstable because of the fluid dynamic forces generated by the tube's own motion. The following sections will clarify how these mechanisms operate in the present model and what the nature of the relationship between the mass-damping parameter and the dimensionless velocity is.

6.4.1 Mathematical Aspects

In both the single flexible tube model and the multiple flexible tube model, the mass ratio for a given dimensionless velocity and array geometry is determined from equation 4.1. This equation has very interesting properties and a close examination yields important information about how the damping-controlled and the stiffness-controlled dynamic instabilities behave. A form of equation (4.1) is rewritten below :

$$\frac{m}{\rho d^2} = \frac{\lambda_R + i\,\lambda_I}{1 - \left(\frac{\omega}{\omega_n}\right)^2 + i\frac{\delta}{\pi}\left(\frac{\omega}{\omega_n}\right)} \tag{6.1}$$

Here, λ represents the fluid forcing function acting on a tube (i.e. $\lambda = \bar{F}_{y_1} / \dot{y}_1$ if tube #1 is being investigated). In a physical system, the mass ratio, $m/\rho d^2$, and the frequency ratio,

ω/ω_n, are real quantities. Therefore, equation (6.1) is forced to yield a real valued mass ratio, $m/\rho d^2$, and a real valued frequency ratio, ω/ω_n. In the case of λ_R/λ_I << 1 (the ratio λ_R/λ_I physically related to the phase difference between a tube's displacement and the total fluid force acting on the tube by the relationship $\theta_{disp-force} = \mathrm{Arctan}(\lambda_I/\lambda_R)$), equation (6.1) reduces approximately to :

$$\frac{m}{\rho d^2} = \frac{i\ \lambda_I}{i\frac{\delta}{\pi}\ (\frac{\omega}{\omega_n})} \tag{6.2}$$

Note that since the real component of the numerator is set to zero, the real component of the denominator has to be zero in order to obtain a real valued mass ratio, $m/\rho d^2$. This requirement leads to : $\omega/\omega_n = 1.0$. This is the approximate solution used for the whole range by Chen [6-8], Price & Païdoussis [9-13] and Lever & Weaver [23-25]. Rewriting equation (6.2), one can obtain :

$$\frac{m\delta}{\rho d^2} = \pi\ \lambda_I \tag{6.3}$$

As can be seen in equation (6.3) the mass-damping parameter, $m\delta/\rho d^2$, comes out of the nondimensional analysis.

In the case of λ_R/λ_I >> 1, equation (6.1) reduces approximately to the following.

$$\frac{m}{\rho d^2} = \frac{\lambda_R}{1 - (\frac{\omega}{\omega_n})^2} \tag{6.4}$$

Since the imaginary component of the numerator is set to zero, the imaginary component of the denominator has to be zero in order to yield a real valued mass ratio, $m/\rho d^2$. This requirement leads to: $\omega/\omega_n = 0.0$. This solution happens to be the solution for the static instability and represents a limiting case for dynamic instability of a single flexible tube in a rigid array. Substituting $\omega/\omega_n = 0$ and rewriting equation (6.2), one can obtain :

$$\frac{m}{\rho d^2} = \lambda_R \tag{6.5}$$

It is important to note that the mass ratio, $m/\rho d^2$, and the logarithmic decrement, δ, are separate and they do not have to be grouped in the mass-damping parameter, $m\delta/\rho d^2$. That is, the damping, as represented by δ, has no effect on static instabilities. This type of behavior is predicted by the present model to exist only in a single degree of freedom system at very high values of the mass ratio.

In reality, because of the finite inertia of the surrounding fluid, there generally exists a phase difference, $\theta_{disp-force}$, between the tube motion and the fluid force acting on the tube. This results in the complex valued forcing function, λ, in equation (6.1) and, depending on the value of λ_R/λ_I, the solution can be approximated by either equation (6.3) or equation (6.5). These approximate solutions intersect at $\lambda_R/\lambda_I = \pi/\delta$. This ratio is $\lambda_R/\lambda_I = 10\pi$ and $\theta_{disp-force} = 1.5^\circ$ for $\delta = 0.1$. Figure 6.4 shows the exact solution of equation (6.1) for $m\delta/\rho d^2$ together with the two approximate solutions when $\delta = 0.1$ and $\lambda_I = 1.0$. If the value of λ_I changes, the solutions shown in figure 6.4 would shift vertically while the lines representing the approximate solutions crossing always at $\lambda_R/\lambda_I = 10\pi$.

In a physical system, λ_R and λ_I represents the stiffness and damping forces, respectively. This means that even though damping is as small as only 5% of the stiffness force, the damping type instability is dominant.

Tanaka and Takahara's experiments show that the above mentioned phase difference, $\theta_{disp-force}$, is larger than 1.5° for the whole range within which they took the measurements. These results make physical sense, since at low mass-damping parameters, fluid inertia is fairly large and fluid responds to a tubes motion with a large time (phase) delay. At high mass-damping parameters, the critical flow velocity is so high that the interaction of the neighboring tubes become important. As a result of the fluid forces due to the neighboring tube motions which are not necessarily in phase with the tube's displacement, again, $\theta_{disp-force}$ is expected to be larger than 1.5°. This means that in actual heat exchanger analysis, equation

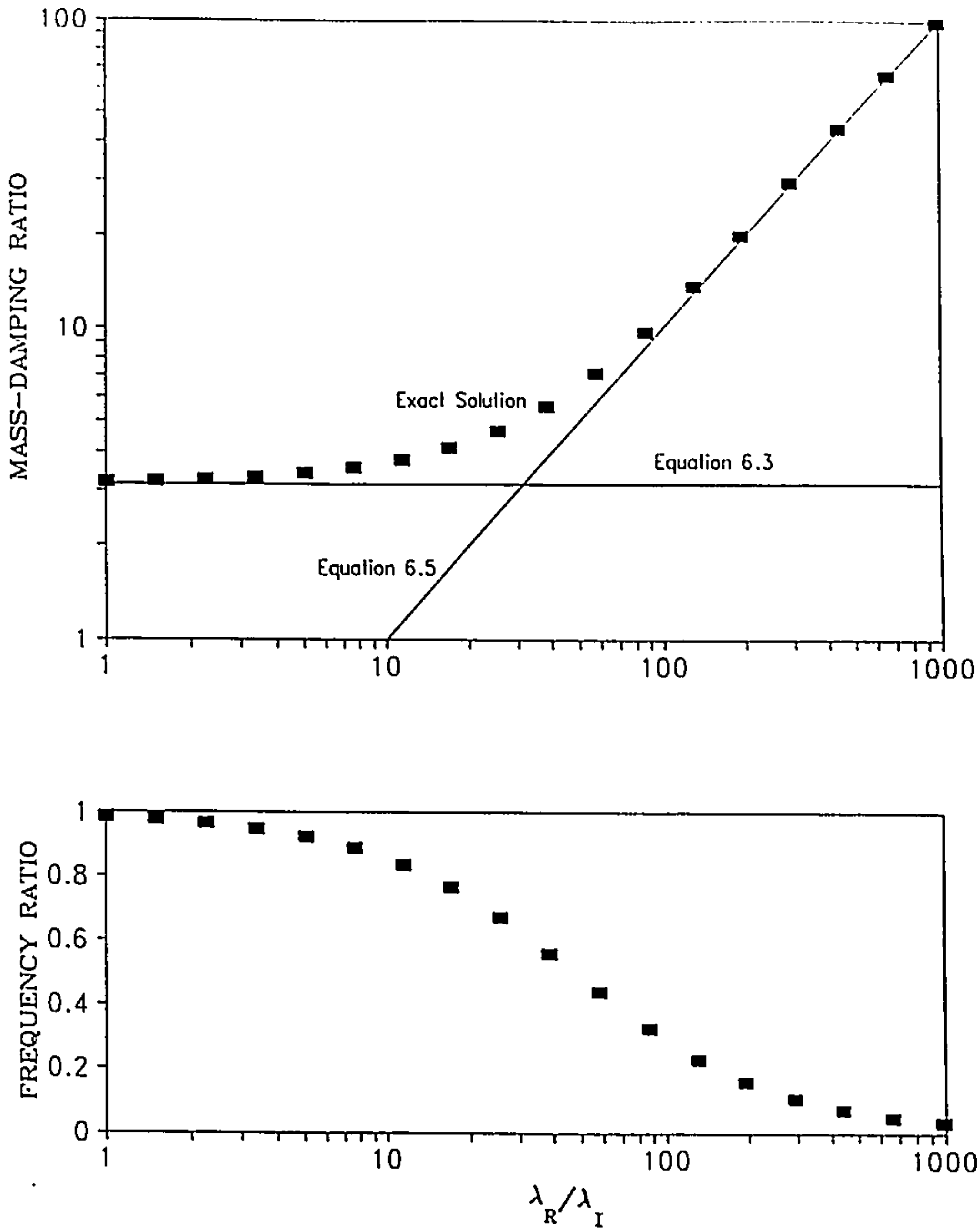

Figure 6.4 Approximate Solutions and the Exact Solution for the Mass-Damping Ratio, $m\delta/\rho d^2$, and the Frequency Ratio, ω/ω_n

6.3 can be used as a good approximation. This behavior also explains why the frequency ratio, ω/ω_n, remains almost constant and equal to one in heat exchanger arrays with multiple degrees of freedom.

6.4.2 Physical Aspects

The form of the forcing function, λ, is obtained for the single and multiple tube analysis in chapters 3 and 4, respectively. Substituting these functions in equation 6.1, the following results are obtained.

(i) Single Flexible Tube :

The fluid force acting on a single flexible tube is given by equation 3.26. Therefore, the forcing function λ can be written as :

$$\lambda = C_{ycy} = C0_{ycy} U_r^2 + C1_{ycy} U_r \left(\frac{\omega}{\omega_n}\right) + C2_{ycy} \left(\frac{\omega}{\omega_n}\right)^2 \qquad (6.6)$$

In general, the force coefficients, $C0_{ycy}$, $C1_{ycy}$ and $C2_{ycy}$ are complex numbers and their amplitudes are only geometry and phase function dependent. Figure 6.5 shows the magnitude and the phase of these force coefficients of a typical system. As seen in figure 6.5, the force coefficient $C2_{ycy}$ is much smaller than other two force coefficients and can be ignored for an approximate solution. An inspection of the continuity and the momentum equations, equations (3.7) and (3.10), respectively, shows that

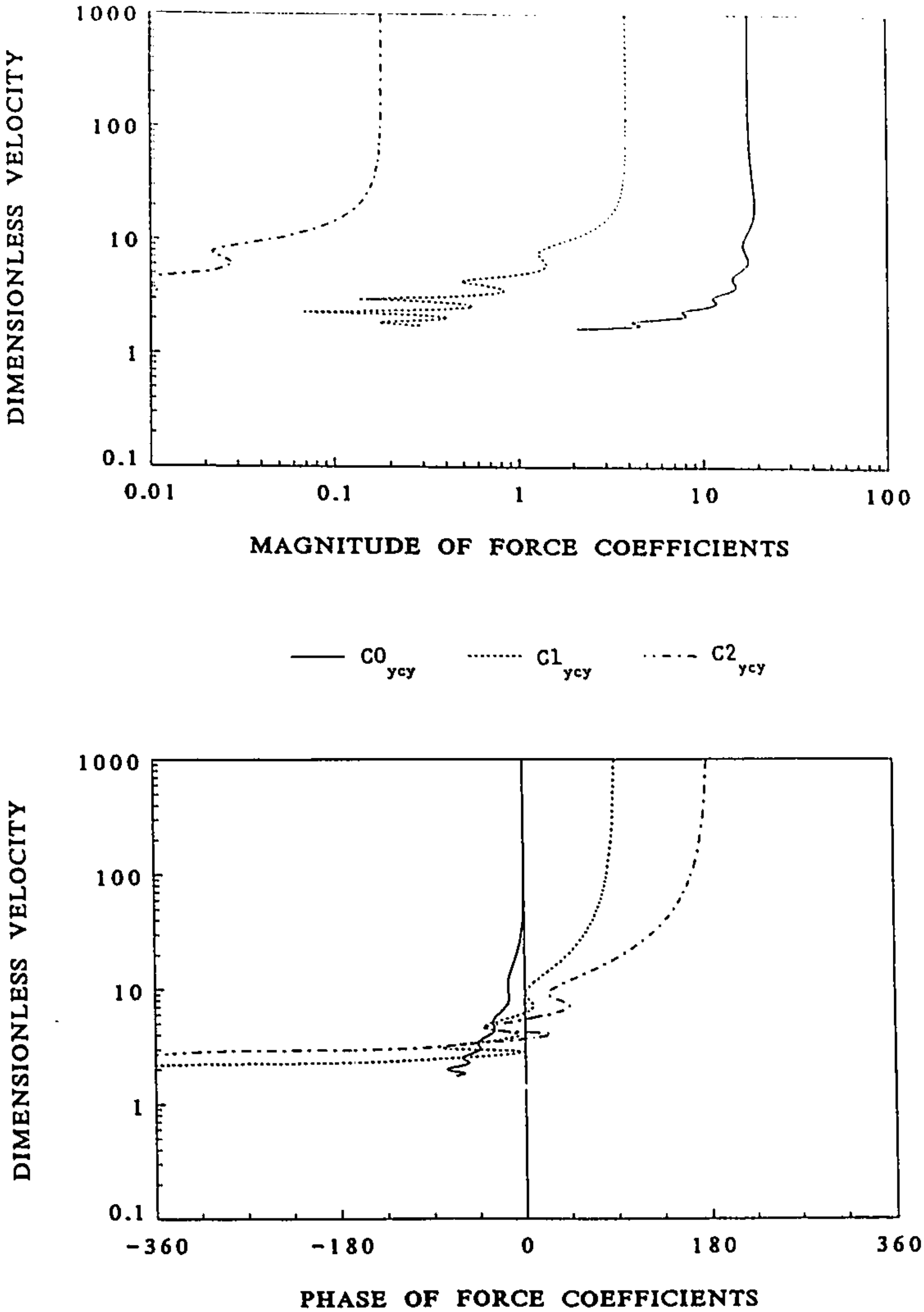

Figure 6.5 Magnitudes and Phase Angles of the Fluid Force Coefficients, $C0_{ycy}$, $C1_{ycy}$, and $C2_{ycy}$

the phase angles of the force coefficients, $C0_{ycy}$, $C1_{ycy}$ and $C2_{ycy}$ are phase shifted from the phase function at $s = -s_1$, $\phi(-s_1)$, by approximately 0°, 90°, 180°, respectively. This is also seen in figure 6.5. At intermediate and high values of the dimensionless velocity, $U_r > 10$, the phase function approaches zero. Hence, $C0_{ycy}$,$C1_{ycy}$ and $C2_{ycy}$ would have the phase angles of approximately 0°, $90^\circ$and 180°. By ignoring the insignificant last term of equation (6.6) and rewriting it :

$$\lambda \cong U_r^2 \, |C0_{ycy}| \angle 0^\circ \quad + \; U_r(\frac{\omega}{\omega_n}) \; |C1_{ycy}| \angle 90^\circ$$

$$\cong U_r^2 \, |C0_{ycy}| \; + \; U_r(\frac{\omega}{\omega_n}) \; |C1_{ycy}| \; i \qquad (6.7)$$

Substituting equation (6.7) into (6.1) yields the mass ratio, $m/\rho d^2$, and the frequency ratio, ω/ω_n. If the approximate solution given by equation (6.3) is used for these ranges of dimensionless velocity, one can find the following relationship :

$$\frac{m\delta}{\rho d^2} \cong |C1_{ycy}| \; U_r \qquad (6.8)$$

This is the solution obtained by Lever and Weaver [23-25]. They obtained a linear relationship between the mass damping parameter, $m\delta/\rho d^2$, and the dimensionless velocity, U_r, as seen in figure 3.7. This behavior is now explained by equation (6.8). However, in the previous chapter it was shown that when $\lambda_R/\lambda_I > 56$ (this might happen only in 1 d.o.f. systems with high mass-damping ratios), it is not correct to use the approximate solution used by other researchers [6-29]. Since $|CO_{ycy}|$ and $|CO_{ycy}|$ are of the same order of magnitude, $(\lambda_R/\lambda_I) = |CO_{ycy}|U_r^2/|CO_{ycy}|U_r \cong U_r$ for $U_f = U_r K_u > 10$. Hence, at very high values of dimensionless velocity, $U_f > 500$ (this number is valid for the parallel triangular arrays with $P_r = 1.375$ where $K_u \cong 15$, it is array dependant), (λ_R/λ_I) becomes larger than 56 and equation (6.5) gives a better approximation. Using equation (6.5) in this range of dimensionless velocity, the following relationship is found :

$$\frac{m}{\rho d^2} \cong |CO_{ycy}|\ U_r^2 \tag{6.9}$$

The mass-damping parameter is obtained from equation (6.9) by multiplying both sides by δ. Note that the mass ratio, $m/\rho d^2$, in equation (6.9) is now proportional to the square of the dimensionless velocity, U_f. This behavior can be seen at high values of dimensionless velocity in figure 3.9 to 3.13. As it is given in equation (6.9), the real (stiffness) component of C_{ycy}, CO_{ycy} , is responsible for this dynamic instability.

At very high mass-damping parameters, dynamic instability in single degree of freedom systems tends towards divergence and is associated with reduced values of the frequency ratio. Figure 6.6 shows the change in frequency ratio, ω/ω_n, for the predicted dynamic instability given in figure 6.3. The dashed line shows the solution for the single flexible tube. As seen in the figure, the frequency ratio approaches zero when the dimensionless velocity becomes very large. Unfortunately, there

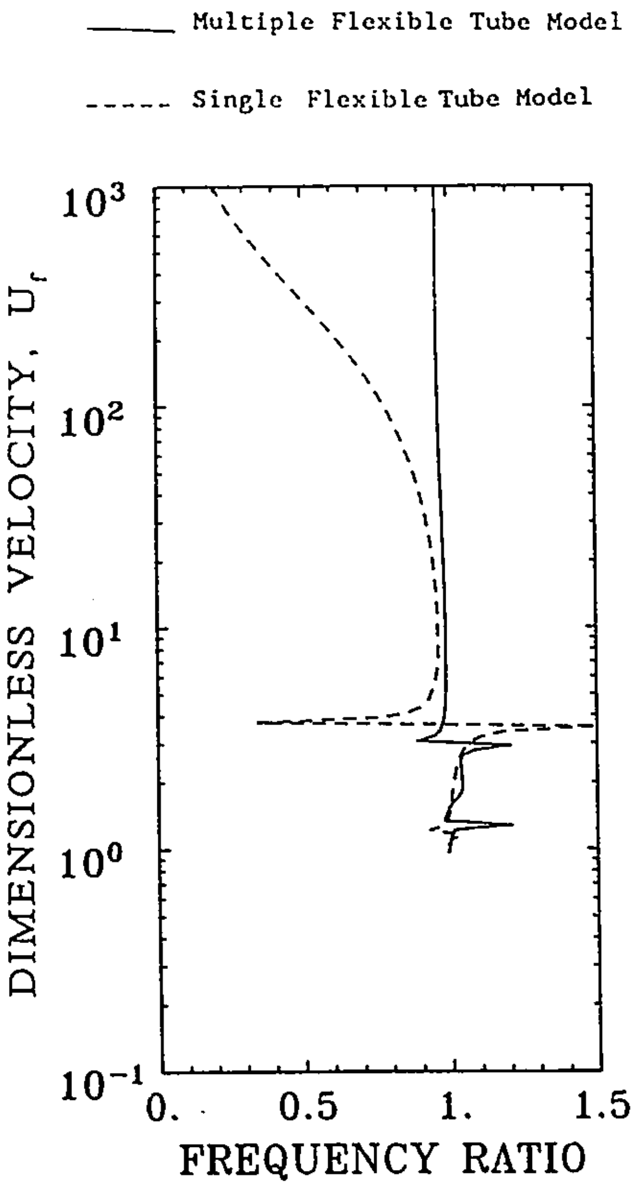

Figure 6.6 Frequency Ratio, ω/ω_n, as a Function of the Dimensionless Velocity, U_r, for the Single Flexible Tube Model and the Multiple Flexible Tube Model

are no experimental data available in the literature to corroborate this predicted behavior. This type of dynamic instability is different than the stiffness-controlled dynamic instability reported by Chen and Price & Païdoussis where the coupling of the neighboring tubes is necessary. Stiffness-controlled instability in multiple flexible tube models compares with the experimental observations reasonably well, while maintaining $\omega/\omega_n \cong 1$. In order to model the neighboring tube behavior, more than one degree of freedom is necessary. In chapter 4, the extension of the single flexible tube model to the multiple flexible tube model was given so that the stiffness controlled instability could be more properly modelled.

(ii) Multiple Flexible Tube Model

In the multiple flexible tube model, the force coefficient, λ, is determined as explained in section 4.3. In general λ is a function of the upstream and downstream tubes' force coefficients. This shows that the interaction between the neighboring tubes has been modelled appropriately. From the analysis of 5 flexible tubes, at high values of the mass-damping parameters, λ is obtained in equation (4.29) as :

$$\lambda = C_{ycy} - 2\,(C_{ydy} - C_{yuy}) \angle\, \psi_2 \tag{6.9}$$

The force coefficient C_{yuy} is usually a few times smaller than C_{ydy} and C_{ycy}, and hence doesn't affect the results significantly. The unsteady flow equations yield these coefficients in the form :

$$C_{ydy} = CO_{ydy} U_r^2 + C1_{ydy} U_r \left(\frac{\omega}{\omega_n}\right) + C2_{ydy} \left(\frac{\omega}{\omega_n}\right)^2$$

$$C_{yuy} = CO_{yuy} U_r^2 + C1_{yuy} U_r \left(\frac{\omega}{\omega_n}\right) + C2_{yuy} \left(\frac{\omega}{\omega_n}\right)^2 \tag{6.10}$$

Again, the $C2_{ydy}$ and $C2_{yuy}$ terms are negligible and can be eliminated from the analysis without significant loss of accuracy. The phase angles of C_{ydy} and C_{yuy} closely follow the phase angles of C_{ycy}. Hence, for intermediate and high values of the dimensionless velocities (for example, when the fluid density is small, U_r>10), the phase function, $\phi(s)$, yields small phase angles and equation (6.10) reduces to :

$$C_{ydy} \cong |CO_{ydy}|\ U_r^2 + i|C1_{ydy}|\ U_r\left(\frac{\omega}{\omega_n}\right)$$

$$C_{yuy} \cong |CO_{yuy}|\ U_r^2 + i|C1_{yuy}|\ U_r\left(\frac{\omega}{\omega_n}\right) \tag{6.11}$$

The force coefficient CO_{ydy} is the same order of magnitude as its counterpart, CO_{ycy}. Similarly, the coefficient $C1_{ydy}$ has the same order of magnitude as its counterpart, $C1_{ycy}$. Although they have the same order of magnitude, CO_{yuy} and $C1_{yuy}$ are few times smaller than their counterparts in general.

Stiffness Controlled Dynamic Instability :

At high values of dimensionless velocity (typically U_r > 100), the phase function $\phi(s)$ yields small values representing a light fluid responding to the tube vibration almost instantly. In this case, CO_{ydy} and CO_{yuy} are essentially real numbers and represent the stiffness forces, and $C1_{ydy}$ and $C1_{yuy}$ are essentially imaginary numbers and represent the damping forces. In this range of dimensionless velocities, the stiffness forces, $CO_{ydy}U_r^2$ and $CO_{yuy}U_r^2$, are much larger in magnitude than the damping forces, $C1_{ydy}U_r$ and $C1_{yuy}U_r$, respectively. Therefore an approximate solution can be obtained by ignoring $C1_{ydy}$ and $C1_{yuy}$ and substituting equations (6.11) into equation (6.9) as follows:

$$\lambda \cong |CO_{ycy}|\ U_r^2 - 2\ (|CO_{ydy}|-|CO_{yuy}|)\ U_r^2 \angle \psi_2 \qquad (6.12)$$

When optimized for minimum dimensionless velocity, ψ_2 is found to be approximately -90°. Since $|CO_{ydy}|$ is several times larger than $|CO_{yuy}|$, the imaginary component of λ in equation (6.12) is a positive number, and of the same order of magnitude as the real component of λ. Now, even at very high dimensionless velocities, $(\lambda_R/\lambda_I) \cong 1$. Hence the solution of this equation can be obtained by using the approximate formula given by equation (6.3) as follows:

$$\frac{m\delta}{\rho d^2} \cong 2\pi\ (|CO_{ydy}|-|CO_{yuy}|)\ U_r^2 \qquad (6.13)$$

All the terms in this approximate solution are stiffness terms, and therefore, after Chen [6], this type of instability is called the stiffness-controlled dynamic instability. Note that the coefficient, CO_{ycy} , disappears from the analysis when the approximate solution is used. The implication of this is that the *stiffness controlled instability* in multiple degrees of freedom systems is produced as a result of the neighboring tubes' motion. Also, note that the larger the difference in the magnitudes of the force coefficients C_{ydy} and C_{yuy}, larger the mass-damping parameter will be. Since the minimum critical velocity is predicted when the mass-damping parameter is maximum, it appears that an essential feature in the stiffness controlled mechanism is the difference in the magnitudes of the forces acting on a tube due to its upstream and downstream neighbors.

The individual effects of the stiffness and damping terms can be seen clearly in figure 6.7 for the parallel triangular array with a pitch ratio of 1.5. In this figure the solid line shows the exact solution and the dashed lines show two other solutions, one solution has only the stiffness terms included and the other has only damping terms included. As can be seen in figure 6.7, at high mass-damping ratios the exact solution and the solution with only the stiffness terms are very close, hence the dynamic instability is stiffness-controlled. This solution yields the slope of the dynamic instability curve to be 0.5. Previous results obtained by Chen, Price & Païdoussis, and Tanaka & Takahara support these results.

Damping Controlled Dynamic Instability :

At intermediate and low dimensionless flow velocities (U_r < 100), all the force coefficients CO_{ycy}, CO_{ydy}, CO_{yuy} $C1_{ycy}$, $C1_{ydy}$ and $C1_{yuy}$ are complex numbers. Hence, it may not be

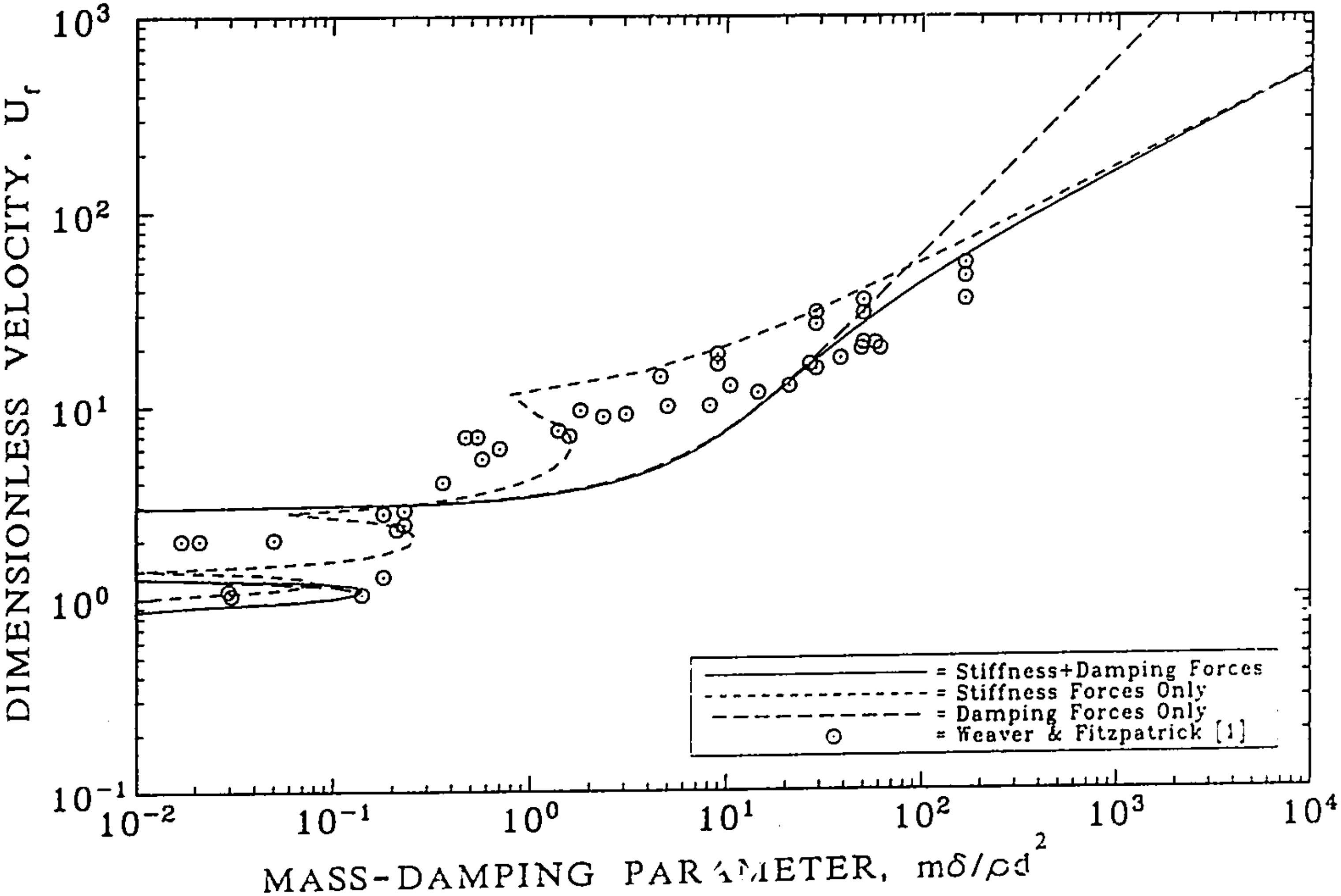

Figure 6.7 Dynamic Instability Obtained by including (a) Stiffness Terms Only, (b) Damping Terms Only, and (c) Both Stiffness and Damping Terms (Parallel Triangular Array, $P_r = 1.5$)

appropriate to use the simplified force equations (6.11). The full form of the force coefficients given in equation (6.10) should be used. Unfortunately, this form of the force coefficients doesn't lend itself to any simplified solutions. In this region, the instability is predicted accurately by using damping terms only which also agrees with previous authors. It should be noted that the fluid stiffness forces are about the same order of magnitude as the fluid damping forces. However, due to the reasons explained in section 6.4.1, the fluid damping forces prevail in predicting the dynamic instability threshold.

6.5 RESULTS FOR VARIOUS ARRAYS

The idealized streamtube geometries for various tube arrays are depicted in figure 3.1 and the model parameters are given in table 6.1. As mentioned earlier, Lever and Weaver's steady state drag coefficient, c_D, used to model the pressure drop and added damping, was not found to have much effect and was therefore dropped from the model. The decay function given by equation 3.34 is used for all arrays. The final results for the 5 flexible tube model are given for various arrays in figures 6.8 through 6.10. In these results, the predicted lower branches of the instability regions are eliminated, and only three instability regions are allowed. Both qualitative and quantitative agreement is reasonably good for all arrays.

In all arrays at high mass-damping parameters, the slope of the instability curve approaches 0.5. This is the area where the fluid stiffness forces are dominant. At low mass-damping

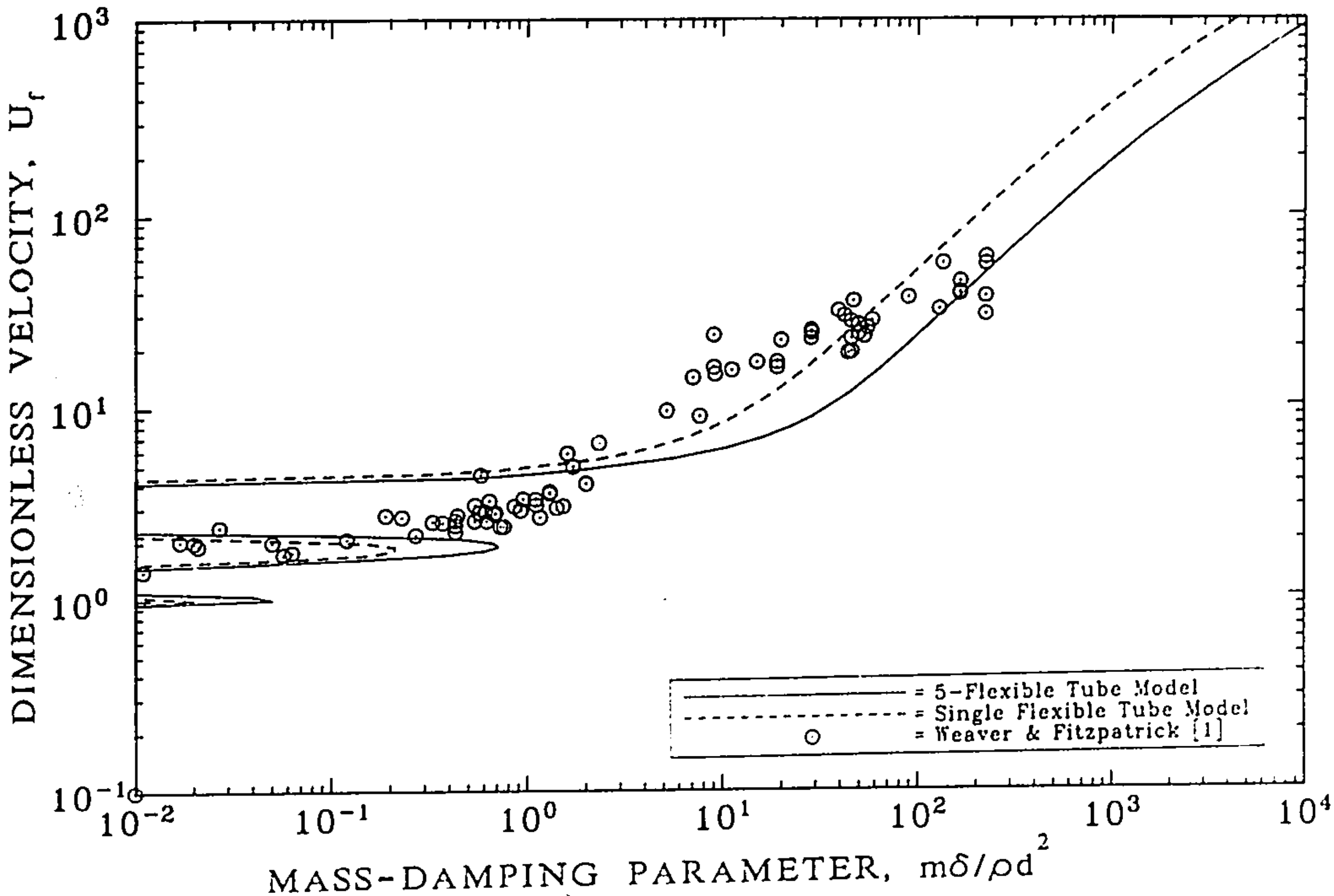

Figure 6.8 Present Theoretical .rediction of the Dynamic Instability for the In-Line Square Arrays with $P_r = 1.5$

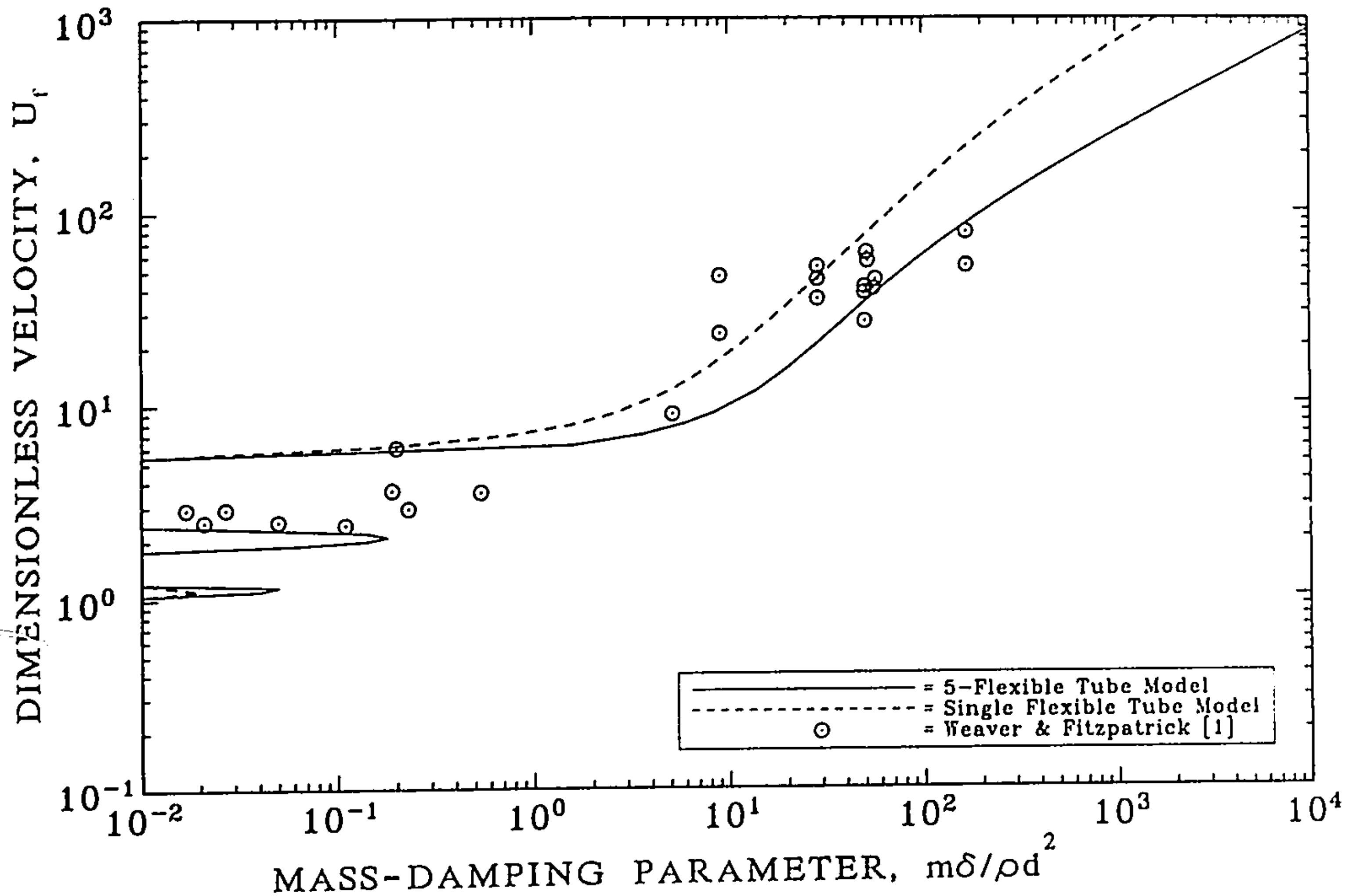

Figure 6.9 Present Theoretical Prediction of the Dynamic Instability for the Rotated Square Arrays with $P_r = 1.5$

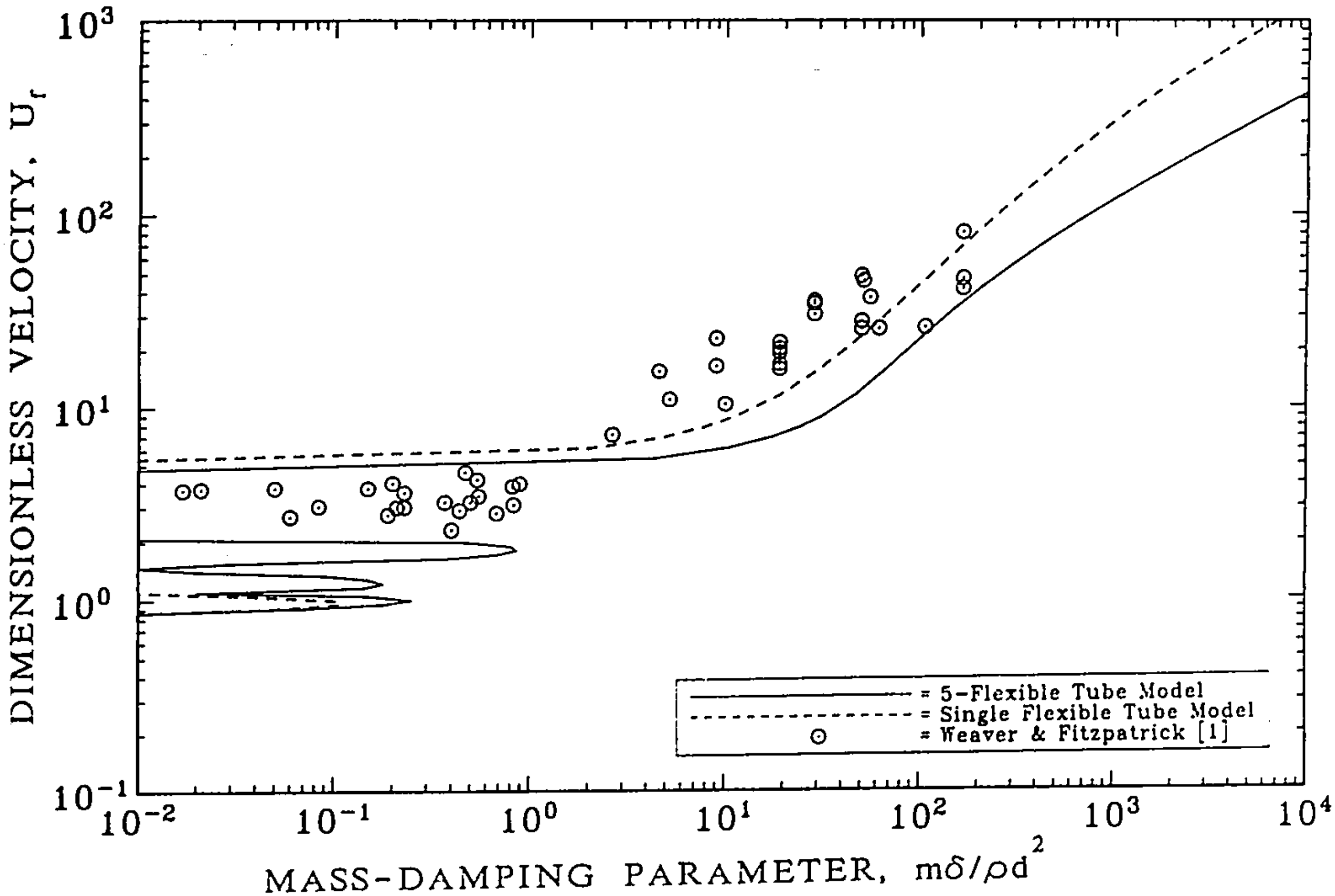

Figure 6.10 Present Theoretical Prediction of the Dynamic Instability for the Rotated Triangular Arrays with $P_r = 1.5$

parameters, the fluid damping forces determine the the dynamic instability threshold and the multiple flexible tube solution approaches to the single flexible tube solution. The solution in this region is not fully satisfactory due to the predicted multiple instability regions. However, the agreement with experiments is reasonably good when the lower branches of the instability regions are eliminated artificially.

6.6 SUMMARY

The summary of the important findings can be listed as follows;

(1) The unsteady force coefficients determined from the simplified flow field are found to be in the form :

$$C = C_0 U_r^2 + C_1 U_r \left(\frac{\omega}{\omega_n}\right) + C_2 \left(\frac{\omega}{\omega_n}\right)^2$$

It was found that the coefficient C_2 is much smaller than C_0 and C_1, in general and can be neglected for a reasonable approximation. At intermediate and high values of the mass-damping parameter, $m\delta/\rho d^2 > 10$, the coefficients C_0, C_1 are found to be in phase with the tube displacement and and tube velocity, respectively. Hence, simplified relationships can be found between the dimensionless velocity, U_r, and the mass damping parameter, $m\delta/\rho d^2$.

(2) Dynamic instability of a single degree of freedom system (for example a single flexible tube moving in one direction in a tube array) was found to tend towards divergence at very high

mass-damping parameters. This type of instability is associated with the vibration frequencies smaller than the natural frequency of the flexible tube. In this range, the relationship between the dimensionless velocity and the mass-damping parameter is of Connors type.

(3) It was found that the single flexible tube in an array can go dynamically unstable in the streamwise direction if the transverse motion is restricted. However, transverse dynamic instability is always more critical than streamwise dynamic instability.

(4) The stiffness controlled instability in multiple degrees of freedom systems (for example, multiple flexible tubes in a tube array) is found to be the result of the neighboring tubes' motion. In this type of stiffness controlled instability, the frequency ratio is always approximately equal to one. The relationship between the dimensionless velocity and the mass-damping parameter is , again, of Connors type. These results are in agreement with the other researchers findings. At low mass-damping parameters, it was found that the dynamic instability is dominated by the fluid damping forces and the coupling between the neighboring tubes doesn't affect the results significantly. Again, these results are in agreement with the literature.

(5) It was found that the mysterious multiple instability regions in Lever & Weaver and Price & Païdoussis theories are caused by the unrealistically high values of the phase

function at low mass-damping parameters. This finding suggest that the phase function used in this study needs to be investigated in the future for a satisfactory solution.

CHAPTER 7

CONCLUSIONS AND RECOMMENDATIONS

The purpose of this thesis was to investigate theoretically the fluidelastic instability in heat exchanger tube bundles. It was thought that through a theoretical analysis which requires minimum experimental data, an improved understanding of the fundamental behavior could be obtained and a useful predictive model could be developed. For this purpose, Lever and Weaver's single flexible tube model was modified and extended to a multiple flexible tube model. As with Lever and Weaver's model, the present model takes into account the effect of the array geometry and is general for all the standard array geometries. Although some experimental data was used when developing the present model, no new measurements are necessary to apply the theory to different arrays.

In the present theoretical development, anomalies in Lever and Weaver's theory are explained and dealt with. In Lever and Weaver's original model, the dynamic instability solution would not yield the static instability solution when the time dependent terms in the formulation were set to zero. This mathematical problem is solved by setting the boundary conditions at the streamtube inlet in a consistent way through the use of the perturbation decay function.

It was found that the dynamic instability in the modified single flexible tube model tends towards divergence at very high mass-damping parameters. This type of instability is associated with reduced frequency ratios, i.e. the vibration frequency at thestability threshold is less than the natural frequency of the flexible tube and decreases with increasing mass-damping parameter. As the mass-damping parameter becomes very large, the frequency at instability approaches zero, i.e. the dynamic instability threshold approaches static instability threshold. This behaviour has not been observed experimentally and it must be concluded that the use of a single flexible tube in a rigid array to model a fully flexible array is not valid at large values of the mass-damping parameter. The semi-empirical models developed by other researchers have indicated that the coupling motion of neighboring tubes becomes important at high mass-damping parameters. Therefore, the single flexible tube model was extended to a multiple flexible tube model to include the effect of the neighboring tubes motion.

In general, it was found that the multiple flexible tube model predicts lower critical velocities than the single flexible tube model. At high values of the mass-damping parameters, dynamic instability is found to be dominated by the displacement dependent fluid stiffness forces. It was found that the coupling between the neighboring tubes is the essential feature in this type of dynamic instability. The resultant relationship between the mass-damping parameter and the dimensionless critical velocity is found to be of the Connors type. The same behaviour is reported by Chen [6,8] and Price & Païdoussis [10-13] and is supported by the experimental data. It should be noted that the results obtained by Chen and

Tanaka & Takahara are based on the measured unsteady fluid dynamic forces and, therefore, their findings represent the actual behaviour of the tube arrays. At low mass-damping parameters, present results show that the solution is dominated by the fluid damping forces as reported by other researchers.

Experiments were carried out in an air tunnel to measure the perturbation decay function and the phase function. Velocity fluctuations were measured up to 4 rows upstream of a vibrating tube. Although, useful information was obtained regarding the decay function, the measured phase data were chaotic with no systematic trends. Repeated attempts failed to produce better data and the experiment was abandoned.

Multiple instability regions are predicted by the present multiple flexible tube model. This behaviour is similar to Lever & Weaver's and Price & Païdoussis's results. It was found that these multiple instability regions are the result of the perturbations created by the vibrating tube many cycles earlier. This behaviour is the result of the unrealisticaly high values of the phase function at low dimensionless velocities. Since no better phase information exists at present, the phase function basically as proposed by Lever & Weaver is used, but only three instability regions are allowed. In this way the perturbations created by the vibrating tube are artificially forced to diminish within two cycles. Intuitively, this seems reasonable. The Price & Païdoussis' flow retardation parameter, a form of phase function, shows the same multiple instability regions. These authors eliminated this unrealistic behaviour in the same way. Clearly, at this stage, the theoretical modelling of the fluidelastic instability at low mass-damping values is not totally satisfactory. Future work is necessary to determine the nature of the phase function and to treat dissipation effects in a more realistic way.

The present theoretical model is a general theory applicable to all the standard array geometries with any pitch ratio. The unsteady forces acting on the tubes are determined from the unsteady fluid dynamics of idealized flow fields. The only experimental data necessary for the theory are the attachment and separation points of the streamtubes. The attachment and separation points of the streamtubes that were obtained experimentally [44] for all the standard array geometries are used in the present study. Hence, no new experimental data are required to obtain the predicted instability for any standard array configuration. As mentioned earlier, good qualitative agreement is found between the present results and the semi-empirical theories of Chen, Price & Païdoussis, and Tanaka & Takahara. Quantitatively, results obtained agree reasonably well with experimental data for all standard array geometries. This represents a significant improvement over the prediction of the Lever and Weaver model.

7.1 FUTURE WORK

In this study, an attempt was made to justify all the simplifying assumptions on physical grounds. However, the phase function is not modelled to the author's full satisfaction. The reasonable agreement of the critical predictions with experimental data from the literature indicates that the phase function has the correct characteristics. Unfortunately, in spite of a substantial effort to verify the proposed phase function experimentally, no conclusive information was obtained. Clearly, the flow field is more complicated than what was modelled. From this point on, the best progress on the present model can be made with experimental studies designed to improve understanding the unsteady flow field.

The present theory models the fluid dynamics in one dimension. Two dimensional effects, however, might be important in the immediate neighborhood of the flexible tubes, especially at low mass-damping parameters. Perturbations should be propagating and decaying in the transverse direction as well as in the modelled streamwise direction. Also, in the present study, the effects of unsteady wakes have not been modelled. Unsteady wakes could cause the attachment and separation points, which are assumed to be stationary in the present model, to change as a function of time.

An interesting, but unknown, behaviour is predicted by the present single flexible tube model at high values of the mass-damping parameter which corresponds to high dimensionless velocities. At these velocities, the present theory predicts that a single flexible tube, when restricted to move only in transverse direction, will go dynamically unstable at significantly lower frequencies than its natural frequency and will tend towards divergence. It would be interesting to conduct an experimental study to investigate this predicted behaviour.

Further applications of the present theory might help our understanding of specific problems associated with heat exchanger tube instability. A possible extension is to include the tube motion in the streamwise direction as well as the transverse direction in the multiple tube analysis. This extension is straightforward and such an analysis would yield the effects of coupling of the streamwise and the transverse vibrations. It is also straightforward to modify the theory to take into account the direction dependent natural frequency. Such a model can be used to predict the instability in heat exchanger U-bend regions where the stiffness of the tubes (therefore the natural frequencies) are not the same in streamwise and transverse directions. Fluidelastic instability in open lanes can also be investigated with small modifications to the existing theory. In such applications, the continuity and the momentum equations must be solved separately for the two streamtubes, one on each side of the flexible tube being considered.

REFERENCES

[1] WEAVER, D.S., FITZPATRICK, J.A.: "A review of cross-flow induced vibations in heat exchanger tube arays", J. of Fluids and Structures, Vol. 2(1), 1988, pp.73-93

[2] PAÏDOUSSIS, M.P.: "A review of flow-induced vibrations in reactors and reactor components", Nuclear Engineering and Design, Vol.74(1), 1983, pp.31-60.

[3] CONNORS, J.H.: "Fluidelastic Vibration of Tube Arrays Excited by Cross Flow", Flow-Induced Vibration in Heat Exchangers, ed., D.D. Reiff, ASME, New York, 1970

[4] BLEVINS, R.D.: " Fluidelastic Whirling of a Tube Row", ASME Journal of Pressure Vessel Technology, Vol. 96, 1974, pp.263-267.

[5] BLEVINS, R.D.: "Fluidelastic Whirling of Tube Rows and Tube Arrays", ASME Journal of Fluids Engineering, Vol. 99, 1977, pp. 457-461.

[6] CHEN, S.S.: "Instability mechanisms and stability criteria of a group of circular cylinders subject to cross flow. Part 1: Theory", ASME Journal of Vibration, Acoustics, Stress and Reliability in Design, v.105, 1983, pp. 51-58.

[7] CHEN, S.S.: "Instability mechanisms and stability criteria of a group of circular cylinders subject to cross flow. Part 2: Numerical Results and Discissions", ASME Journal of Vibration, Acoustics, Stress and Reliability in Design, v.105, 1983, pp. 51-58.

[8] CHEN, S.S.: "A general theory for dynamic instability of tube arrays in crossflow", J. of Fluids and Structures, Vol. 1, 1987, pp. 35-53.

[9] PRICE, S.J., PAÏDOUSSIS, M.P.: "Fluidelastic Inatability of a double row of circular cylinders subject to a cross-flow", ASME Journal of Vibration, Acoustics, Stress and Reliability in Design", Vol. 105, 1983, pp. 56-66.

[10] PRICE, S.J., PAÏDOUSSIS, M.P.: "An improved mathematical model for the stability of cylinder rows subject to cross flow", J. Sound and Vibration, Vol. 97, 1984, pp. 615-640.

[11] PRICE, S.J., PAÏDOUSSIS, M.P.: "A constrained-mode analysis of the fluidelastic instability of a double row of flexible circular cylinders subject to cross-flow: a theoretical

Investigation of system parameters", J. Sound and Vibration, Vol. 105(1), 1986, pp. 121-142.

[12] PRICE, S.J., PAÏDOUSSIS, M.P.: "Fluidelastic instability of a full array of flexible cylinders subject to cross flow", *ASME Symposium on Fluid-Structure Interaction and Aerodynamic Damping*, Cincinnati, 1985, pp. 171-192.

[13] PRICE, S.J., PAÏDOUSSIS, M.P. and GIANNIAS, N.: "A Generalized Constrained-Mode Analysis in Cross Flow", *ASME International Symposium on Flow-Induced Vibration and Noise*, Chicago, Vol. 3, 1988, pp. 25-55.

[14] TANAKA, H.,TAKAHARA, S.: "Unsteady Fluid Dynamic Force on Tube Bundle and its Dynamic Effect on Vibration", Flow-Induced Vibration in Power Plant Components, ASME, PVP-Vol. 41, ed. Au-Yang, M.K., New York, 1980, pp. 77-92.

[15] TANAKA, H.,TAKAHARA, S.: "Fluidelastic Vibration of Tube Array in Cross Flow", Journal of Sound and Vibration, Vol 77, 1981, pp. 19-37.

[16] TANAKA, H.,TAKAHARA, S. and OHTA, K.: "Flow-Induced Vibration of Tube Arrays with Various Pitch-to-Diameter Ratios", Symposium on Flow-Induced Vibration of Circular Cylindrical Structure, PVP-Vol. 63, ASME, New York, 1982, pp. 45-56

[17] WHISTON, G.S. and THOMAS, G.D.: "Whirling Instabilities in Heat Exchanger tube Arrays", Journal of Sound and Vibration, Vol. 77, 1982, pp. 1-31.

[18] CHEN, S.S.: "Crossflow-Induced Vibrations of Heat Exchanger Tube Banks", Nuclear Engineering and Design, Vol. 47, 1978, pp. 67-86

[19] BALSA, T.F.: "Potential Flow Interactions in an Array of Cylinders in Cross-flow", Journal of Sound and Vibration, Vol. 52, 1977, pp. 285-303.

[20] PAÏDOUSSIS, M.P., MAVRIPLIS, D. and PRICE, S.J.: "A potential flow theory for the dynamics of cylinder arrays in cross flow", J. of Fluid Mechanics, Vol. 146, 1984, pp. 227-252.

[21] PAÏDOUSSIS, M.P., PRICE, S.J. and MAVRIPLIS, D.: "A Semi-Potential Flow Theory for the Dynamics of Cylinder Arrays in Cross Flow", Journal of Fluid Mechanics, Vol. 146, pp. 67-82.

[22] VAN DER HOOGT, P.J.M. and VAN CAMPEN, D.H.: "Self-induced

Instabilities if parallel tubes in cross-flow", ASME Winter Annual Meeting, *Symposium on Flow-Induced Vibration*, New Orleans, Vol. 2, 1984. pp. 53-66.

[23] LEVER, J.H. and WEAVER, D.S.: "A theoretical model for fluid-elastic instability in heat exchanger tube bundles", ASME J. Pressure Vessel Technology, Vol. 104, 1982, pp. 147-158.

[24] LEVER, J.H. and WEAVER, D.S.: "On the stability behaviour of heat exchanger tube bundles: Part 1 - Modified theoretical model", J. Sound and Vibration, Vol.107(3), 1986, pp. 375-392.

[25] LEVER, J.H. and WEAVER, D.S.: "On the stability behaviour of heat exchanger tube bundles: Part 2 - Numerical results and comparison with experiments", J. Sound and Vibration, Vol. 107(3), 1986, pp. 393-410.

[26] ROBERTS, B.W.: "Low Frequency aeroelastic vibrations in a cascade of circular cylinders", Mechanical Engineering Science Monograph, No. 4, 1966.

[27] CHEN, S.S.: "Guidelines for the Instability Flow Velocity of Tube Arrays in Cross Flow", Journal of Sound and Vibration, Vol. 93, 1984, 439-455.

[28] CHEN, S.S.: "Some Issues Concerning Fluidelastic Instability of Group of Circular Cylinders in Crossflow", ASME Winter Annual Meeting, *International Symposium on Flow-Induced Vibration and Noise*, Chicago, Vol. 3, 1988, pp. 1-24.

[29] PAÏDOUSSIS, M.P. and PRICE, S.J.: "The Mechanisms Underlying Flow Induced Instabilities of Cylinder Arrays in Cross Flow", Journal of Fluid Mechanics, Vol. 187, pp. 45-59.

[30] HARTLEN, R.T.: "Wind Tunnel Determination of the Fluid Elastic Vibration Thresholds for Typical Heat-Exchanger Tube Patterns", Ontario Hydro Research Division Report No. 74-309-K, 1974

[31] PETTIGREW, M.J.., SYLVESTER, Y., and CAMPAGNA, A.O., "Vibration Analysis of Heat Exchanger Components in Liquid and Two-Phase Cross Flow", *ASME Flow Induced Vibration Guidelines*, New York, Vol. 52, 1981, pp. 89-110.

[32] PETTIGREW, M.J.: "Flow Induced Vibration Phenomena in Nuclear Power Station Components", Power Industry Research, Vol.1, 1981, pp. 97-133.

[33] SOPER, B.M.: "The Effect of Tube Layout on the Fluidelastic

Instability of Tube Bundles in Cross Flow", Flow-induced Heat Exchanger Tube Vibration, 1980, eds. Chenoweth, J.M. and Stenner, J.R., HTD_Vol. 9, ASME, New York, 1980. pp. 1-9.

[34] SAVKAR, S.D.: " A Note on the Phase Relationships Involved in the Whirling Instability in Tube Arrays", ASME Journal of Fluids Engineering, Dec.1977/727.

[35] GIBERT, R.J., CHABRERIE, J. and SAGNER, M.: "Vibration of Tube Arrays in Transversal Flow", Transactions of 4th International Conferance on Structural Mechanics in Reactor Technology", Series F, Paper F4/h, San Fransisco, 1977.

[36] HEILKER, W.J. and VINCENT, R.Q.: "Vibration in Nuclear Heat Exchangers Due to Liquid and Two-Phase Flow", Transactions of ASME, Journal of Engineering for Power, Vol. 103, 1981, pp. 358-366.

[37] WEAVER, D.S. and GROVER, L.K.: "Cross-flow Induced Vibrations in a Tube Bank - Turbulent Buffeting and Fluidelastic Instability", Journal of Sound and Vibration, Vol. 59, 1978, pp. 277-294

[38] WEAVER, D.S. and EL-KASHLAN, M.: "The effect of Damping and Mass Ratio on the Stability of a Tube Bank", J. Sound and Vibration, vol.76, 1981, pp. 283-294

[39] WEAVER, D.S. and KOROYANNAKIS, D.: " The Cross-flow Response of a Tube Array in Water - A Comparision with the same Array in Air", ASME Journal of Pressure Vessel Technology, Vol. 104, 1982, pp. 139-146.

[40] WEAVER, D.S. and YEUNG, H.C.: " The Effect of Tube Mass on the Flow Induced Response of Various Tube Arrays in Water", Journal of Sound and Vibration, Vol. 93, 1984, 409-425.

[41] YEUNG, H.C. and WEAVER, D.S.: "The effect of approach flow direction on the flow induced vibrations of a triangular tube array", ASME Journal of Vibration, Acoustics, Stress and Reliability in Design, Vol. 105, 1983, 76-82.

[42] WEAVER, D.S. and ABD-RABBO, A.: "A Flow Visualization Study of a Square Array of Tubes in Water Crossflow", ASME Journal of Fluids Engineering, Vol. 107, 1985, 354-363.

[43] ABD-RABBO, A. and WEAVER, D.S.: "A Flow Visualization Study of Flow Development in Staggered Tube Array", Journal of Sound and Vibration, Vol. 106, 1986, pp. 241-256.

[44] SCOTT, P.: "Flow Visualization of cross-flow-induced vibrations in tube arrays", M.Eng. Thesis, Department of Mechanical Engineering, McMaster University, Hamilton,

Ontario, Canada, 1987.

[45] GORMAN, D.J.: "The Effects of Artificially Induced Upstream Turbulance on the Liquid Cross-flow Induced Vibration of Tube Bundles", *ASME Symposium on Flow-Induced Vibration in Power Plant Components*, ed. Au-Yang, M.K., PVP-Vol. 41, 1980, 33-43.

[46] FRANKLIN, R.E. and SOPER, B.M.H.: "An Investigation of Fluidelastic Instabilities in Tube Bank Subjected to Fluid Cross-flow", Trans. 4th International Conferance on Structural Mechanics in Reactor Technology, San Fransisco, 1977.

[47] WARING, L. "Partial Admission Effects on the Stability of a Heat Exchanger Tube Array", M.Eng. Thesis, Department of Mechanical Engineering, McMaster University, Hamilton, Ontario, Canada, 1987.

[48] ANJELIC, M. and POPP, K.: " Data for the Fluidelastic instability of Heat Exchanger Tube Bundles", *ASME International Symposium on Flow-Induced Vibration and Noise*, Chicago, Vol. 3, 1988, pp. 57-76.

[49] Blevins, R.D., Flow-Induced Vibration, Van-Nostrand Rheinhold Co., New York, 1977